Scanning near-field infrared microspectroscopy on semiconductor structures

DISSERTATION

zur Erlangung des akademischen Grades
doctor rerum naturalium (Dr. rer. nat.)

durchgeführt am Helmholtz-Zentrum Dresden-Rossendorf

eingereicht an der Fakultät Mathematik und
Naturwissenschaften der Technischen Universität Dresden

von Dipl.-Phys. Rainer Jacob

HZDR
HELMHOLTZ ZENTRUM DRESDEN ROSSENDORF

TECHNISCHE UNIVERSITÄT DRESDEN

Gutachter:

1. Prof. Dr. Manfred Helm (Technische Universität Dresden)
2. Prof. Dr. Lukas Eng (Technische Universität Dresden)

eingereicht im Januar 2011

Abstract

Near-field optical microscopy has attracted remarkable attention, as it is the only technique that allows the investigation of local optical properties with a resolution far below the diffraction limit. Especially, the scattering-type near-field optical microscopy allows the nondestructive examination of surfaces without restrictions to the applicable wavelengths. However, its usability is limited by the availability of appropriate light sources. In the context of this work, this limit was overcome by the development of a scattering-type near-field microscope that uses a widely tunable free-electron laser as primary light source.

In the theoretical part, it is shown that an optical near-field contrast can be expected when materials with different dielectric functions are combined. It is derived that these differences yield different scattering cross-sections for the coupled system of the probe and the sample. Those cross-sections define the strength of the near-field signal that can be measured for different materials. Hence, an optical contrast can be expected, when different scattering cross-sections are probed. This principle also applies to vertically stacked or even buried materials, as shown in this thesis experimentally for two sample systems.

In the first example, the different dielectric functions were obtained by locally changing the carrier concentration in silicon by the implantation of boron. It is shown that the concentration of free charge-carriers can be deduced from the near-field contrast between implanted and pure silicon. For this purpose, two different experimental approaches were used, a non-interferometric one by using variable wavelengths and an interferometric one with a fixed wavelength. As those techniques yield complementary information, they can be used to quantitatively determine the effective carrier concentration. Both approaches yield consistent results for the carrier concentration, which excellently agrees with predictions from literature.

While the structures of the first system were in the micrometer regime, the capability to probe buried nanostructures is demonstrated at a sample of indium arsenide quantum dots. Those dots are covered by a thick layer of gallium arsenide. For the first time ever, it is shown experimentally that transitions between electron states in *single* quantum dots can be investigated by near-field microscopy. By monitoring the near-field response of these quantum dots while scanning the wavelength of the incident light beam, it was possible to obtain characteristic near-field signatures of single dots. Near-field contrasts up to 30 % could be measured for resonant excitation of electrons in the conduction band of the indium arsenide dots.

Zusammenfassung

Die optische Nahfeldmikroskopie hat viel Beachtung auf sich gezogen, da sie die einzige Technologie ist, welche die Untersuchung lokaler optischer Eigenschaften mit Auflösungen unterhalb der Beugungsgrenze ermöglicht. Speziell die streuende Nahfeldmikroskopie erlaubt die zerstörungsfreie Untersuchung von Oberflächen ohne Einschränkung der verwendbaren Wellenlängen. Die Nutzung ist jedoch durch das Vorhandensein entsprechender Lichtquellen beschränkt. Im Rahmen dieser Arbeit wurde diese Beschränkung durch Entwicklung eines streuenden Nahfeldmikroskops überwunden, das einen weit stimmbaren Freie-Elektronen-Laser als primäre Lichtquelle benutzt.

Im theoretischen Teil wird gezeigt, dass ein optischer Kontrast erwartet werden kann, wenn Materialien mit unterschiedlichen Dielektrizitätskonstanten kombiniert werden. Es wird hergeleitet, dass diese Unterschiede in unterschiedlichen Streuquerschnitten für das gekoppelte System aus Messkopf und Probe resultieren. Diese Streuquerschnitte definieren die Stärke des Nahfeldsignals, welches auf unterschiedlichen Materialien gemessen werden kann. Ein optischer Kontrast kann also erwartet werden, wenn unterschiedliche Streuquerschnitte untersucht werden. Dass dieses Prinzip auch auf übereinander geschichtete oder sogar verborgene Strukturen angewendet werden kann, wird in dieser Doktorarbeit an zwei Probensystemen experimentell gezeigt.

Im ersten Beispiel wurden die unterschiedlichen Dielektrizitätskonstanten durch örtliches Ändern der Ladungsträgerdichte in Silizium durch Bor-Implantation erreicht. Es wird gezeigt, dass die Dichte der freien Ladungsträger an Hand des optischen Kontrastes zwischen implantiertem und reinem Silizium ermittelt werden kann. Zu diesem Zweck wurden zwei unterschiedliche Ansätze verwendet, ein nicht-interferometrischer mittels variabler Wellenlängen und ein interferometrischer mit einer konstanten Wellenlänge. Weil diese Techniken gegensätzliche Informationen liefern, können sie genutzt werden, um die effektive Ladungsträgerdichte quantitativ zu bestimmen. Beide Ansätze lieferten konsistente Resultate für die Trägerdichte, welche sehr gut mit den Vorhersagen der Literatur übereinstimmt.

Während die Strukturen im ersten Beispiel im Mikrometer-Bereich lagen, wird die Möglichkeit, verborgene Nanostrukturen zu untersuchen, an Hand einer Probe mit Indiumarsenid Quantenpunkten demonstriert. Diese sind von einer dicken Schicht Galliumarsenid bedeckt. Zum ersten Mal wird experimentell gezeigt, dass Übergänge zwischen Elektronenzuständen in *einzelnen* Quantenpunkten mit Nahfeldmikroskopie untersucht werden können. Durch die Messung der Nahfeld-Antwort der Quantenpunkte unter Änderung der Wellenlänge des eingestrahlten Lichtes war es möglich, charakteristische Nahfeld-Signaturen der einzelnen Quantenpunkte zu erhalten. Nahfeld-Kontraste bis zu 30 Prozent konnten für die resonante Anregung der Elektronen im Leitungsband der Indiumarsenid Punkte beobachtet werden.

Contents

List of Figures

List of Tables

Nomenclature

a-SNOM	Aperture scanning near-field optical microscope
ac	Alternating current
AFM	Atomic force microscope
AM-AFM	Amplitude modulated control of AFM mode
As	Arsenic
CO_2	Carbon dioxide
dc	Direct current
ELBE	Electron linear accelerator for beams with high brilliance and low emittance
FEL	Free-electron laser
FM-AFM	Frequency modulated control of AFM mode
FWHM	Full width half maximum
Ga	Gallium
GaAs	Gallium arsenide
InAs	Indium arsenide
KPFM	Kelvin probe force microscopy
KRS-5	Thallium-bromoiodide
LIA	Lock-in amplifier
MCT	Mercury cadmium telluride (detector)
ML	Monolayer
PL	Photoluminescence
PSD	Positioning-sensing device
PtIr	Platinum-iridium

RTA	Rapid thermal annealing
s-SNOM	Scattering-type scanning near-field optical microscope
Si	Silicon
SiC	Silicon carbide
SiO_2	Silicon dioxide
SNOM	Scanning near-field optical microscope
SNR	Signal-to-noise ratio
STM	Scanning tunneling microscope
T-B	Top-minus-bottom signal of the PSD
TPX	Polymethylpentene
U100	Undulator with 100 mm period
U27	Undulator with 27.3 mm period
ZnSe	Zinc selenite

1 Introduction

Students are often introduced into a new topic by famous anecdotes. For the present thesis, such an anecdote could be the image of a naked man running through the streets of Syracuse and yelling "*Eureka*!". Another one could be the apple that falls from a tree onto the head of man sitting below it.

The former is the Greek scholar Archimedes of Syracuse after discovering the buoyancy, also known as the principle of Archimedes. The latter is Isaac Newton who was said to have been inspired to formulate his theory of gravitation by watching the fall of an apple from a tree.

On first glance, both scientists show nothing in common, as their achievements are related to different parts of science. A closer look, however, will reveal that their fundamental breakthroughs are based on the same scientific method: OBSERVATION. But the capabilities of the human eye are limited. Hence, the human mind invented tools to support and extend its usage.

For example, the telescope (from the Greek τῆλε, tele "far" and σκοπεῖν, skopein "to look or see") was invented to see objects that are very far away. Contrary to that, the microscope (from the Greek μικρός, mikros "small") allows the observation of very small objects. Since their first appearance, both concepts have passed numerous enhancements that pushed the optical resolution to the physical limits. For classical optics, this limit in microscopy is given by the diffraction limit of E. Abbe [Abb73]. It restricts the resolution to roughly half of the used wavelength. To resolve smaller objects, a new ansatz for microscopy was necessary. This new concept was proposed by Synge [Syn28] and with it, he established the near-field microscopy. He also described the promising prospects, although it lasted 50 years until the first experimental realization. Using

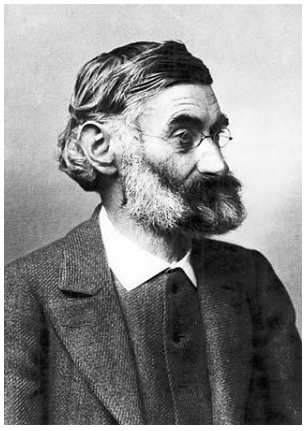

Figure 1.1: *Photo of Ernst Abbe, recorded before 1905 in Jena by Emil Tesch [Tes05].*

near-fields, this kind of microscopy allows optical resolution on almost atomic length scales. Hence, it should be named nanoscopy (from the Greek νᾶνος, nanos "dwarf"), as it can resolve objects which are not accessible by classical microscopy.

Another fundamental new concept was the laser, developed around 1960, as a new type of light source. For the first timer ever, it provided light of a certain wavelength without broadband background light. While it was first used for scientific applications, we use its numerous possibilities today without even thinking about its Nobel prize awarded concept. It can be found in compact disc players or home cinema systems, in mass storage devices, in bar-code readers in the supermarket or as pointers for presentations. Today a life without lasers is almost impossible to imagine. The near-field microscopy would also be different without lasers, because only lasers in combination with fiber optics allowed the technical realization of Synge's concept at the beginning. Meanwhile, the necessity of optical fibers could be overcome, but the laser is still necessary, even though there are ideas to replace them by broadband sources. This necessity presents a major drawback of near-field microscopy, since lasers are typically fixed to a certain wavelength and with it, they deny a spectroscopic use of near-field microscopes in the mid and far-infrared. This changed as the first free-electron lasers entered the stage of scientific light sources. Their technical concept allowed a wide tunability of the wavelength which would make them a perfect light source for the near-field microscopy. Unfortunately, free-electron lasers are big, complex machines and only few of them exist world wide. One of them is situated at the Helmholtz-Zentrum Dresden-Rossendorf, and it emits between 4 µm and 250 µm.

This thesis is part of a project which intended to combine both techniques, creating a near-field microscope fed by a free-electron laser. This would open the door to numerous applications of microscopic as well as spectroscopic nature, since the advantages of both concepts could be exploited. In the context of this project, the primary objective was the setup of the near-field microscope at the Helmholtz-Zentrum, starting with an empty laboratory. Later the setup was applied to investigate semiconducting materials. In order to demonstrate the spectroscopic usage, boron implanted silicon was characterized with respect to the concentration of free carriers in the implanted areas. Furthermore, buried indium arsenide quantum dots were studied as well.

In order to provide all necessary information, this thesis is divided into three parts.

The first part will discuss the theoretical foundations of the near-field microscopy as well as some basics on the free-electron laser. Furthermore, it will provide the theory of the used scanning-probe techniques. En detail, the 2^{nd} chapter shows, how the near-field signals evolve and how they can be predicted with the help of a simple dipole model. For this reason, the measured quantity - the scattering cross-section - is derived with or without a sample. Moreover, influences of, e. g., the polarization of the incident light and reflections at the sample surface are discussed. In the 3^{rd} chapter the general working principle of a free-electron laser is discussed theoretically. It will be shown, how the electron movement creates the electro-magnetic field and how this field is amplified to be usable as laser light. Chapter 4 then discusses the scanning probe techniques which are applied in the context of the near-field microscopy.

In the second part of this thesis, a detailed description of the built near-field micro-

scope is presented. It will be shown, which laser sources are available and a detailed technical discussion will be given (chapter 5). Afterwards, the near-field microscope is discussed and the performance of the setup as well as a description of the alignment process is presented (chapter 6).

The last part is devoted to the scientific discussion of the investigated samples. At the beginning, the boron implanted silicon is introduced in chapter 7. It will be shown, which considerations lead to the sample design and the preparation parameters. Finally, the experimental results, which yield a quantitative number for the carrier concentration, are discussed in detail. The same will be done in chapter 8, for the system of buried quantum dots. Here the scientific aim was the characterization of these dots by means of the near-field signature.

Part I

Fundamentals

2 Near-field optical microscopy

In this chapter the basic concepts of scattering-type near-field optical microscopy are discussed. The quasi-electrostatic model of interacting dipoles is introduced to describe the light scattering at a particle that is small compared to the wavelength. Afterwards this model is extended to account for the presence of a sample. It will be shown how the evanescent near-fields are transformed into propagating waves and which dependencies influence the near-field signal. In the end, different methods are described which can be used to enhance the near-field signals and to separate the signals from the background.

2.1 History - from first experiments to scattering-type near-field optical microscopy

The sense of vision is one of our main sources of information when interacting with our environment. To be able to see we are equipped with one of the first optical devices ever, still created by nature. But while the ability to see was already discussed by Euclid (∼300 B.C.) and other Greek philosophers, it lasted until ∼1000 A.D., when the Arab Alhazen explained the sensation of vision in detail by the first known optical experiments [Voh04]. Again more than two centuries passed afterwards until the first man-made optical device was created. Based on the ideas of Roger Bacon, polished glass was used to correct ametropia. The spectacles were born [Hec89]. The next major step was done at the beginning of the 17th century, as two Dutchmen, Hans and Zacharias Jansen, combined two lenses to magnify small objects, thereby creating the first reported microscope [Bey88]. Over the next 200 years the design of microscopes was improved continuously, aiming for an even greater optical resolution. But the development of improving the resolution with better lenses and lens systems came to halt in the year 1873, when Ernst Abbe published his theories about the resolution limit due to diffraction [Abb73, Abb82]. He showed that there is no possibility to distinguish objects which are closer together than half of the applied wavelength. Hence, a higher spatial resolution may only be achieved by decreasing the wavelength.

This was valid until 1928 when Synge proposed a method to overcome the diffraction limit [Syn28]. His idea was to illuminate the sample through a hole with a diameter of 10^{-6} cm = 10 nm which is then raster scanned over the sample at a 10 nm distance. But, as he already recognized, this was not technically feasible in these days. Especially fabricating such a tiny aperture and bringing it close enough to the surface of interest without touching was not yet possible. More than 40 years passed before Ash and Nicholls [Ash72] were able to realize sub-wavelength resolution in 1972. They achieved a resolution of $\lambda/60$ by using microwaves and an aperture with 1.5 mm in diameter.

But they still lacked a technology to decrease and control the distance between the aperture and the sample in the nanometer range.

With the development of both the scanning tunneling microscope (STM) by Binnig and Rohrer in the early 1980s and subsequently the atomic force microscope (AFM) [Bin81, Bin86], it became possible to position a small aperture within sub-nanometer distance from the sample. Hence, it is not surprising that the first near-field measurements in the visible spectral range were performed directly after the invention of the STMs, since intense light sources had become available with the development of the laser in the 1960s. How fast Synge's concept was realized in the visible range can be seen in the year 1984, when two different groups published their measurements using light of 488 nm wavelength. Both groups showed an optical resolution which was well below half of the wavelength. In the case of Lewis *et al.* [Lew84] it was $\lambda/10$ while Pohl *et al.* [Poh84] even achieved $\lambda/20$. These were the first scanning near-field optical microscopes (SNOM). To be more specific, these were the first aperture scanning near-field optical microscopes (a-SNOM), since they used a small aperture and scanned it across the sample. Only one year later Wessel [Wes85] proposed the substitution of the small aperture by a particle of the same size. He utilized Babinet's theorem [Bab37] which states that the diffraction pattern of two complementary objects is the same. Instead of illuminating the sample via a small aperture, one could place a small particle next to the surface and illuminate the particle. According to Wessel [Wes85] this should result in the same optical properties (see figure 2.1). This principle of an apertureless or scattering-type scanning near-field optical microscope (s-SNOM) was then realized by Specht *et al.* in the year 1992 [Spe92]. Here the tip of a STM was used to probe the near-field of a plasmon in a gold film, achieving a resolution of $\lambda/200$. The first light scattered directly at the apex of a tip was reported by Inouye and Kawata [Ino94]. Later Zenhausern *et al.* [Zen94] achieved a resolution of 3 nm using a similar setup operated at 633 nm wavelength.

Since then both types of near-field microscopes are subject to continuous development. Especially the development of aperture probes like fiber optics is a major topic since the diameter of the aperture defines the resolution. The material of the fibers also limits the usable wavelengths, especially in the infrared region. However, the range of the used wavelength could also be extended into this region by using apertureless near-field microscopes instead [Lah96]. Finally, Stevenson *et al.* [Ste01] reported the first usage of a SNOM in the ultraviolet range in the year 2001.

Parallel to this progress a wide range of applications has evolved for a-SNOM or s-SNOM. Providing a full overview would be beyond the scope of this work. For aperture near-field microscopy detailed sources are Paesler and Moyer[Pae96], Dunn [Dun99] and Hecht *et al.* [Hec00]. The main field for scattering-type near-field microscopy is the infrared region, because the advantage of the wavelength independence takes full effect. Here the potential has been shown mainly using $9 - 11$ µm supplied by tunable carbon dioxide lasers due to the lack of other available sources. Lahrech *et al.* [Lah97], for example, showed the occurrence of differences in the near-field amplitude between implanted and non-implanted silicon. Later similar experiments were performed where the carrier concentration could be deduced directly from the measured amplitude and

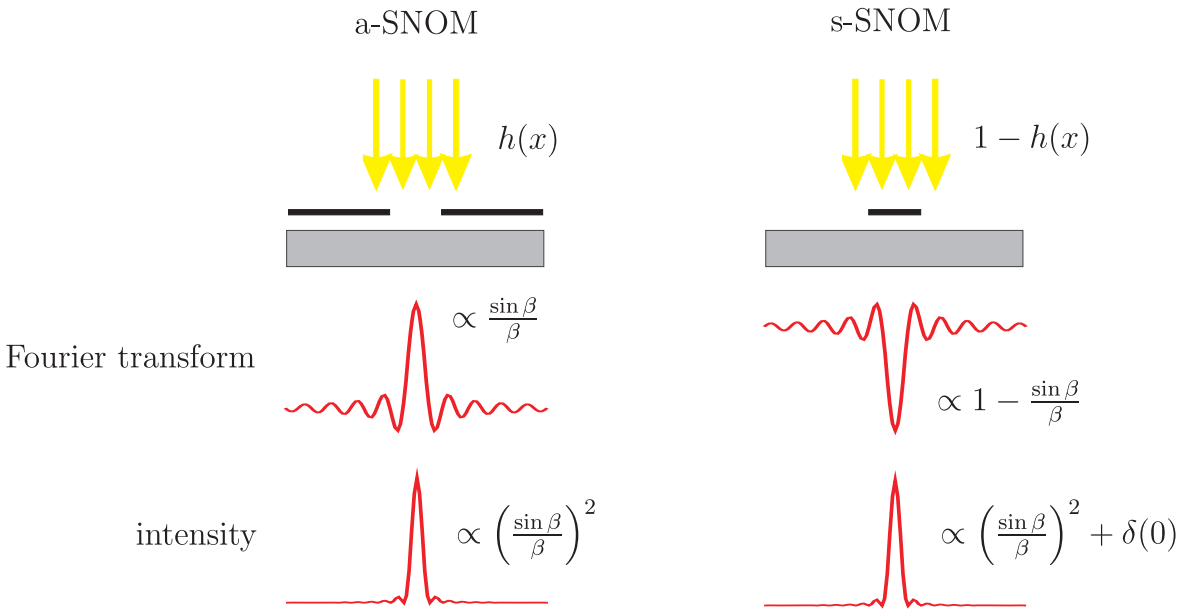

Figure 2.1: *Diffraction pattern of two complementary objects illustrating Babinet's theorem. Thereby, two objects are complementary if the sum of their transfer functions is equal to 1. If $h(x)$ is the aperture's transfer function and $H(\omega)$ is the Fourier transformation $F(h(x))$ then the Fourier transformation of the complementary transfer function $1-h(x)$ is $F(1-h(x)) = \delta(0) - H(\omega)$.*

phase signals [Hub07, Kno00, Kei09, Sti10]. Other reported applications are material recognition due to vibrational absorptions [Kno99] or simple near-field contrast [Hil02], spectroscopy of nanoparticels, viruses and organic molecules [Bre06, Kop07] and the identification of different optical domains in ferroelectric materials [Sch07a, Keh08]. The latter were done using a free-electron laser as a widely tunable light source for infrared light between 4 and 200 µm. This is a major improvement to the common s-SNOM since it breaks the limit given by the carbon dioxide lasers and opens the door to a wide range of new applications.

2.2 Scattering theory

Scattering by a particle

Since the idea of scattering-type near-field microscopy is the substitution of the aperture by a particle acting as a scatterer, the simplest approach for a theoretical description is the Rayleigh scattering for particles small compared to the wavelength. A detailed treatment of this topic is given, for example, in reference [Boh83]. The following discussion is based on this reference. The restriction of a scatterer small compared to the wavelength is fulfilled, for example, if the scatterer is the apex of a scanning probe tip which is the case in common apertureless near-field microscopes. If the particle is illuminated, an external electrical field $\mathbf{E_0}$ is generated at the position of

the particle[1]. While the scattering behavior of the particle is described by its complex scattering coefficient $\widehat{\sigma}$, the scattered electrical field $\mathbf{E_{sca}}$ follows from the coupling of both quantities:

$$\mathbf{E_{sca}} = \widehat{\sigma} \cdot \mathbf{E_0} = \frac{e^{ikr}}{-ikr}\mathbf{T} \tag{2.1}$$

with k the wave number, being $2\pi/\lambda$,
λ the wavelength,
r the distance between the particle and the observer and
$\mathbf{T}$ the far-field scattering amplitude.

The ratio between the scattered $|\mathbf{T}|^2$ and incident light intensity $|\mathbf{E_0}|^2$ is called the differential cross-section $dC_{sca}/d\Omega$. Integrating this quantity over a sphere around the particle yields the scattering cross-section C_{sca} as a measure of the total scattered light intensity:

$$\frac{dC_{sca}}{d\Omega} = \frac{|\mathbf{T}|^2}{k^2|\mathbf{E_0}|^2} \tag{2.2}$$

$$C_{sca} = \int_0^{2\pi}\int_0^{\pi} \frac{dC_{sca}}{d\Omega}\sin\theta \mathrm{d}\theta\mathrm{d}\Phi. \tag{2.3}$$

The generated external field induces a dipole moment $\mathbf{P}$ in the particle that can be expressed as:

$$\mathbf{P} = \varepsilon_0\varepsilon_m\widehat{\alpha} \cdot \mathbf{E_0} \tag{2.4}$$

with ε_0 the vacuum permittivity, being $8.854 \times 10^{12} F/m$,
ε_m the complex dielectric constant of the surrounding medium and
$\widehat{\alpha}$ the complex polarizability which depends on shape and material of the particle.

Knowing the induced dipole moment $\mathbf{P}$, one can substitute the unknown scattering amplitude $\mathbf{T}$ in equation (2.2) and (2.3) by

$$\mathbf{T} = \frac{ik^3}{4\pi\varepsilon_m\varepsilon_0}\mathbf{e_r} \times (\mathbf{e_r} \times \mathbf{P}), \tag{2.5}$$

where $\mathbf{e_r}$ is the unit vector in radial direction with the scatterer in the center. This substitution allows one to express the scattering cross-section in terms of the known quantities $\mathbf{P}$ and $\mathbf{E_0}$. Carrying out the integration of (2.3) over the full solid angle then yields:

$$C_{sca} = \frac{k^4}{6\pi\varepsilon_m^2\varepsilon_0^2}\frac{|\mathbf{P}|^2}{|\mathbf{E_0}|^2}. \tag{2.6}$$

[1] In this work the following nomenclature is used: vectors are bold face, tensors with a circumflex and parameters (real or complex) are plain. Furthermore the International System of Units (SI-system) will be used.

When using equation (2.4) it becomes obvious that the cross-section strongly depends on the direction of the external electric field $\mathbf{E_0}$ in relation to the polarizability tensor $\widehat{\alpha}$ of the particle. This will be discussed in the following.

Up to now there were no restrictions related to the shape of the particle. The importance of it can be seen when having a closer look at the polarizability $\widehat{\alpha}$ of the scatterer [vdH81]. For generalization the particle is described as an ellipsoid

$$\frac{x^2}{a_1} + \frac{y^2}{a_2} + \frac{z^2}{a_3} - 1 = 0 \tag{2.7}$$

with a_i $(i = 1, 2, 3)$ being the three main axes. If the external electric field $\mathbf{E_0}$ is applied along the direction of axis a_i, then the field $\mathbf{E}$ at any point inside the particle is given by

$$\mathbf{E} = \mathbf{E_0} - L_i 4\pi \mathbf{P}. \tag{2.8}$$

The factor L_i thereby depends on the ratio of the three axes and can be calculated using

$$L_i = \int_0^\infty \frac{a_i a_j a_k}{\left(s + a_i^2\right)^{3/2} \left(s + a_j^2\right)^{1/2} \left(s + a_k^2\right)^{1/2}} \mathrm{d}s \text{ with } i \neq j \neq k \in \{1, 2, 3\}. \tag{2.9}$$

This equation is valid for an arbitrary ratio of the semiaxes. Moreover, only two of the three geometrical factors L_i are independent because of the relation

$$\sum_{i=1}^{3} L_i = 1. \tag{2.10}$$

It can then be shown that the elements α_i of the diagonal polarizability tensor fulfill

$$\frac{V}{4\pi\alpha_i} = L_i + \frac{\varepsilon_m}{\varepsilon - \varepsilon_m}, \tag{2.11}$$

where ε is the complex dielectric function and V the volume of the ellipsoid. In the special case of a spherical particle with radius r the values L_i are equal to $\frac{1}{3}$ due to the equality of the three axis a_1, a_2 and a_3. This results in the identity of the three tensor elements

$$\alpha_i = \alpha_j = \alpha_k = r^3 \frac{\varepsilon - \varepsilon_m}{\varepsilon + 2\varepsilon_m}. \tag{2.12}$$

The scattering cross-sections C_{sca} then are equal for arbitrary directions of the incident electrical field $\mathbf{E_0}$. The situation changes drastically if one of the axes is elongated like in the case of a prolate (cigar-shaped) spheroid. Here one axis is longer than the others which have the same length ($a_i > a_j$, $a_j = a_k$). In this case one obtains

$$L_i = \frac{1 - e^2}{e^2} \left(-1 + \frac{1}{2e^2} \ln \frac{1 + e}{1 - e} \right) \text{ with } e^2 = 1 - \frac{a_j^2}{a_i^2} \tag{2.13}$$

and

$$L_{j,k} = \frac{1}{2}(1 - L_i). \tag{2.14}$$

Here e is the eccentricity which indicates how strong the ellipsoid differs from a sphere. Now C_{sca} shows a strong dependence on the orientation of $\mathbf{E_0}$ with respect to the pronounced axis of the ellipsoid

$$C_{sca} = \frac{k^4}{6\pi} \frac{|\widehat{\alpha} \cdot \mathbf{E_0}|^2}{|\mathbf{E_0}|^2}. \tag{2.15}$$

This can be seen in figure 2.2. If the particle is a sphere (eccentricity $e = 0$) then the scattering cross-section has the same value for external fields perpendicular and parallel to the distinct axis. When the eccentricity increases and $\mathbf{E_0}$ is perpendicular to the main axis, the cross-section decreases until zero for the case of a needle ($e = 1$). This is fully understandable because an ideal needle (extension only along one axis) is not polarizable perpendicular to its axis. The other case is a field parallel to the longer axis. Here an increase of the eccentricity yields an increase of the scattering cross-section with a maximum in the case of the needle. Again, this is the behavior which one can expect from a very intuitive understanding. Another visible feature is the shift of the resonance (indicate by the red color in the plot). For a sphere the resonance occurs for $\mathrm{Re}(\varepsilon) \approx -2$ due to a singularity of the tensor elements α_i (see equation (2.12)). This resonance shifts to more negative values of $\mathrm{Re}(\varepsilon)$ when the eccentricity increases and the electric field is parallel to the main axis.

Scattering in the presence of a sample

The scattering behavior of the particle changes again, when it is placed above a dielectric material. Now one has to investigate the properties of a coupled system containing the particle and the sample. For simplification the material fills the half-space below the scatterer while they are separated by the distance h (see figure 2.3). In a real experiment these simplifications are valid as long as the sample is not, for example, a thin-film on a substrate and as long as the probe is small compared to the lateral and vertical dimensions of the sample. Furthermore the distance h is assumed to be small compared to the wavelength so that retardation effects can be neglected.

The dipole of the illuminated particle (in the following everything related to the particle has the index "p") induces charges in the sample. These charges then distort the electric field emitted by the particle itself. Thus, the presence of the sample modifies the dipole of the particle. This effect can be calculated by the method of image charges, which has already been applied numerous times [Kog97, Ras03, Wu04, Roy05]. To calculate the resulting field outside the sample, an additional dipole $\mathbf{P_s}$ in the sample is defined:

$$\mathbf{P_s} = \beta \widehat{C} \cdot \mathbf{P_p}. \tag{2.16}$$

It is linked to the dipole of the particle via β being the surface response function and

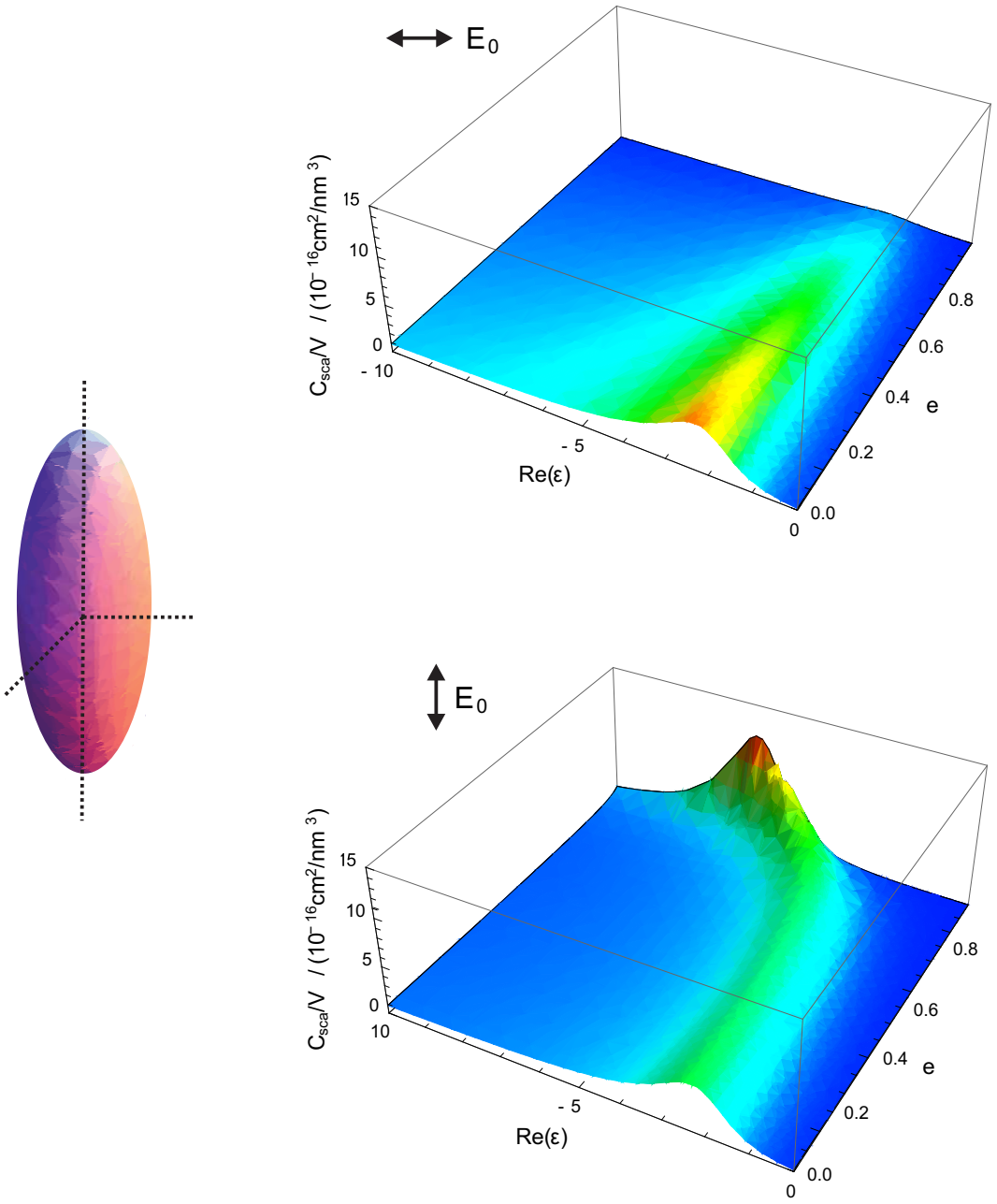

Figure 2.2: *Dependence of the scattering cross-section without sample on the orientation of the incident electric field* $\mathbf{E_0}$ *with respect to the pronounced axis of the ellipsoid as calculated from equation* (2.15)*. Plotted is the cross-section normalized to the ellipsoid volume as a function of the real part of the dielectric function* ε *and of the eccentricity* e *(*$\varepsilon_m = 1$*,* $\mathrm{Im}(\varepsilon) = 1$*,* $\lambda = 633$ nm*, color for better visibility only).*

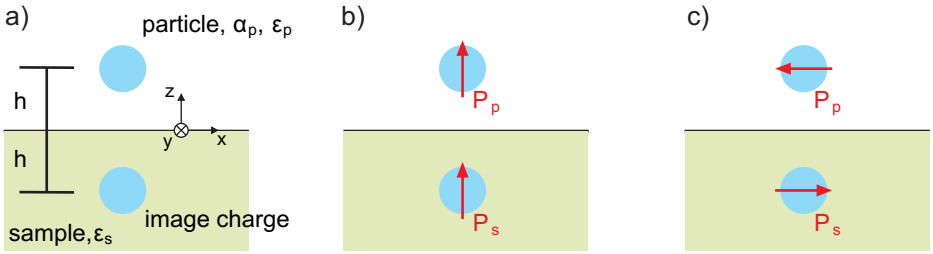

Figure 2.3: *a) Sketch of the particle-sample system as defined in Cartesian coordinates. b) Effect of the coupling matrix $\widehat{C}$ when the particle dipole is orientated vertically. c) Effect when orientated horizontally.*

$\widehat{C}$ describing the coupling between them:

$$\beta = \frac{\varepsilon_s - \varepsilon_m}{\varepsilon_s + \varepsilon_m} \tag{2.17}$$

$$\widehat{C} = \begin{pmatrix} -1 & 0 & 0 \\ 0 & -1 & 0 \\ 0 & 0 & 1 \end{pmatrix} \tag{2.18}$$

with ε_s being the complex dielectric function of the sample. The distortion of the particle's electric field is expressed by an additional field $\mathbf{E_s}$, generated by the image charge at the position of the particle ($\mathbf{r_0} = h\mathbf{e_z}$):

$$\mathbf{E_s} = \frac{3\mathbf{n}(\mathbf{P_s}\mathbf{n}) - \mathbf{P_s}}{4\pi\varepsilon_0|\mathbf{r_0} - \mathbf{r}|^3} \text{ with } \mathbf{n} = \mathbf{e_z}. \tag{2.19}$$

When the sample dipole is expressed using (2.16), this can by written as

$$\mathbf{E_s} = \widehat{K} \cdot \mathbf{P_p} \tag{2.20}$$

with the interaction matrix

$$\widehat{K} = \frac{1}{64\pi\varepsilon_0 h^3} \begin{pmatrix} 2\beta & 0 & 0 \\ 0 & 2\beta & 0 \\ 0 & 0 & 4\beta \end{pmatrix}. \tag{2.21}$$

As the dipole of the particle is modified by this field, equation (2.4) has to be replaced by

$$\mathbf{P_p} = \varepsilon_0\varepsilon_m\widehat{\alpha}_p \cdot (\mathbf{E_0} + \mathbf{E_s}) \tag{2.22}$$

$$= \varepsilon_0\varepsilon_m\widehat{\alpha}_p \cdot \left(\mathbf{E_0} + \widehat{K} \cdot \mathbf{P_p}\right). \tag{2.23}$$

This is solved by

$$\mathbf{P_p} = \left(\widehat{\mathbb{I}} - \varepsilon_0\varepsilon_m\widehat{\alpha}_p \cdot \widehat{K}\right)^{-1} \varepsilon_0\varepsilon_m\widehat{\alpha}_p \cdot \mathbf{E_0} = \widehat{\alpha}'_p \cdot \mathbf{E_0}, \tag{2.24}$$

where $\widehat{\mathbb{I}}$ is the identity matrix and $\widehat{\alpha}'_p$ the modified polarizability tensor of the particle. From this an effective or total dipole moment of the coupled particle-sample system can be derived as the sum of the modified particle dipole and the sample dipole:

$$\mathbf{P_{tot}} = \mathbf{P_p} + \mathbf{P_s} = \varepsilon_0 \varepsilon_m \widehat{\alpha}_{tot} \cdot \mathbf{E_0}, \tag{2.25}$$

where the total polarizability

$$\widehat{\alpha}_{tot} = \left(\widehat{\mathbb{I}} + \beta \widehat{C}\right) \cdot \widehat{\alpha}'_p \tag{2.26}$$

has been introduced. The total dipole moment can then be treated as a particle like it was discussed in the previous section. Thus, the scattered light intensity can be calculated according to equation (2.6) by replacing the undisturbed dipole moment $\mathbf{P}$ with the total dipole moment $\mathbf{P_{tot}}$:

$$C_{sca} = \frac{k^4}{6\pi\varepsilon_m^2\varepsilon_0^2} \frac{|\mathbf{P_{tot}}|^2}{|\mathbf{E_0}|^2}. \tag{2.27}$$

Again there were yet no restrictions to the shape of the particle. In the case of an isotropic sphere, the polarizability tensor can be replaced by a scalar polarizability α_p. For a single particle without a sample the cross-section is independent from the orientation of the incident field, but due to the presence of the sample this dependence is conserved. But now the orientation with respect to the sample surface determines the cross-section. For a field perpendicular to the surface this yields

$$C_{sca,\perp} = \frac{k^4}{6\pi} \left| \frac{(1+\beta)\alpha_p}{1 - \frac{\alpha_p \beta}{16\pi h^3}} \right|^2 \tag{2.28}$$

and for a field parallel to the surface

$$C_{sca,\parallel} = \frac{k^4}{6\pi} \left| \frac{(1-\beta)\alpha_p}{1 - \frac{\alpha_p \beta}{32\pi h^3}} \right|^2. \tag{2.29}$$

As the symmetry of this system is changed from the spherical symmetry of the particle to a more cylindric shape of the coupled system, the cross-section for the perpendicular incident field becomes larger than for the parallel field. A straightforward explanation could be the superposition of both dipoles which superpose constructively in the case of the perpendicular field, while they superpose destructively for a field parallel to the sample surface. Furthermore the cross-section now exhibits a strong dependence on the separation of particle and surface. The overall result of these effects is shown in figure 2.4. Here the scattering cross-section is calculated for a platinum-iridium particle (AFM tips coated with PtIr were used as scatterer in the experimental part of this work) situated above a silicon surface as a function of the distance between particle and sample. The strong exponential decay of the near-field is clearly visible when the separation between the particle and the sample increases. The signal drops below $1/e$ within 3 nm which is less then half of the particle radius and decays slowly afterwards.

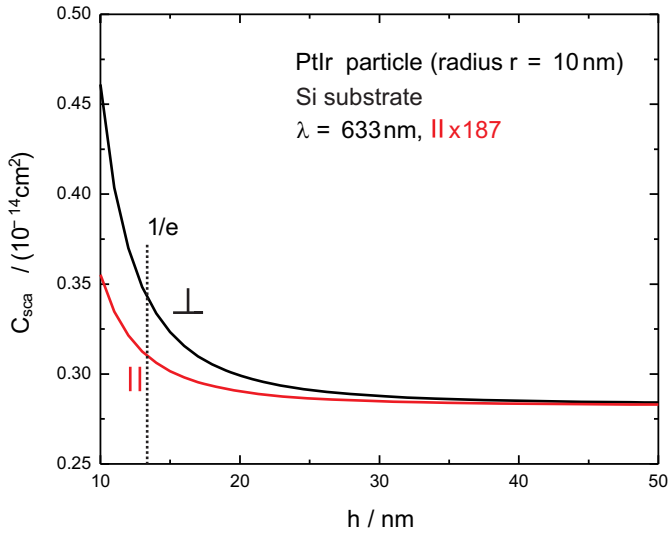

Figure 2.4: *Distance dependence of the scattering cross-section calculated for different orientations of the incident field with respect to the sample surface. Due to the particle radius of* 10 nm *a height of* 10 nm *means contact between particle and surface (see figure 2.3). The cross-section for the parallel-oriented field is multiplied by a factor of 187.*

This shows impressively the critical importance of the particle-sample separation for the scattering cross-section. Furthermore the already mentioned difference between parallel and perpendicular incident fields is depicted, as the parallel case is multiplied by a factor of 187 $\approx \varepsilon_{Si}^2$ which can be derived from the quotient of equations (2.28) and (2.29) in the limit of $h \to \infty$.

AFM tip as scatterer

When adapting the idealized concept of a sphere above a surface to a real experiment, the most significant change is the AFM tip acting as a scatterer instead of a single particle. But while the shape of the tip is well-defined by the fabrication process, it is difficult to say which part of the tip contributes to the near-field signal in the experiment.

If only the very end of the tip contributes to the near-field signal, then describing the tip as an isotropic sphere is a valid approximation. In this case, effects resulting from the shaft and the elongated shape of the tip are neglected. The suitability of this approach to understand material contrasts has been shown many times, for example by Knoll and Keilmann [Kno00] or Ocelic and Hillenbrand [Oce04]. But it reaches its limits when the exponential decay of the near-field is of interest, like it has been shown by Esteban *et al.* [Est07]. In these cases more precise models are necessary which describe the tip as prolate ellipsoids [Cvi07] or even more complex structures [Est07, Est09]. These models are also more suitable to explain polarization effects. They lack analytical expressions for the tip and apply numerical solutions instead. But in principle they also use the dipole-dipole model which is always suitable as long as

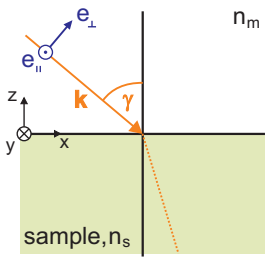

Figure 2.5: *Definition of the incident angle γ and unit vectors $\mathbf{e}_\parallel$ and $\mathbf{e}_\perp$.*

one can express the polarizability of the complex tip structures.

There are a few other approaches to describe the interaction between the tip and the surface. Numerical models like multiple multipoles were used to calculate the electric fields as superpositions of known solutions of Maxwell's equations [Ren04, Nov97, Est09]. These models describe the distance dependence of the near-field signals more exactly than the dipole-dipole model. But in principle, they show comparable results when used for spherical and ellipsoidal tip shapes. Finally there are ideas to describe the interaction based on an antenna-like behavior of the tip [Beh08, Bre08].

Reflection at the sample surface

Finally one has to discuss the effect of reflections from the sample surface, which were neglected in the previous parts. Their importance was recently shown by Samson *et al.* who described the complete near-field response of a s-SNOM in terms of macroscopic reflections [Sam08].

Assuming that the incident electric field consists of components parallel ($E_\parallel$) and perpendicular ($E_\perp$) to the sample surface, it can be written as

$$\mathbf{E_{inc}} = E_\parallel \mathbf{e}_\parallel + E_\perp \mathbf{e}_\perp, \tag{2.30}$$

where

$$\mathbf{e}_\parallel = \begin{pmatrix} 0 \\ -1 \\ 0 \end{pmatrix} \text{ and } \mathbf{e}_\perp = \begin{pmatrix} \cos\gamma \\ 0 \\ \sin\gamma \end{pmatrix} \tag{2.31}$$

are the corresponding unit vectors and γ is the angle of incidence between the **k**-vector of the electric field and the z-axis as (see figure 2.5). Taking into account that the tangential components of the electric and magnetic field have to be consistent at the interface and solving Maxwell's equations yields the reflection coefficients for the perpendicular and parallel field components:

$$r_\parallel = \frac{\cos\gamma - \sqrt{n^2 - \sin^2\gamma}}{\cos\gamma + \sqrt{n^2 - \sin^2\gamma}} \tag{2.32}$$

$$r_\perp = \frac{n^2\cos\gamma - \sqrt{n^2 - \sin^2\gamma}}{n^2\cos\gamma + \sqrt{n^2 - \sin^2\gamma}}. \tag{2.33}$$

Here n is the relative index of refraction, calculated as the ratio of the refraction indices of the sample n_s and the surrounding medium n_m:

$$n = \frac{n_s}{n_m}. \tag{2.34}$$

When knowing the reflection coefficients, the reflected electric field can now be obtained by using (2.30) and (2.18):

$$\mathbf{E_{refl}} = r_{\parallel} E_{\parallel} \mathbf{e}_{\parallel} + r_{\perp} E_{\perp} \widehat{C} \cdot \mathbf{e}_{\perp} \tag{2.35}$$

At the position of the tip the incident and reflected field superimpose so that the external field $\mathbf{E_0}$ can be described as the sum of both fields, as long as the tip-sample separation is small:

$$\mathbf{E_0} = E_{\parallel}(1 + r_{\parallel})\mathbf{e}_{\parallel} + E_{\perp} \left(\widehat{\mathbb{I}} + r_{\perp} \widehat{C} \right) \cdot \mathbf{e}_{\perp} \tag{2.36}$$

The severe impact of the these additional contributions is shown in figure 2.6 for the case of a perpendicular polarized incident field. The reflection coefficients and the scattering cross-section are calculated for a spherical PtIr-particle above a Si-surface. It is clearly visible that the reflection on the sample surface shifts the maximum of the scattering cross-section to lower incident angles. Below the Brewster angle γ_B, the reflected and incident field interfere constructively and even enhance the scattering cross-section by 30 % compared to the case of neglected reflections. But as soon as the incident angle becomes larger than the Brewster angle they interfere destructively and cancel any scattering for $\gamma = 90°$ which was assumed as incident angle in the previous sections. The situation becomes even more complex when the sample exhibits a topography which is not negligible anymore. Additional reflections have to be taken into account, since the angle of incident changes if the incoming light hits, for example, the face of a step edge, where multiple reflections become possible.

Related to these problems, recent investigations [Cvi07] showed a better agreement between experiment and theory when the term $(1+\beta)$ in equation (2.28) is substituted by $(1 + r_{\perp})^2$ or $(1 + r_{\parallel})^2$, respectively, yielding:

$$C_{sca,\perp} = \frac{k^4}{6\pi} \left| \frac{(1 + r_{\perp})^2 \alpha_p}{1 - \frac{\alpha_p \beta}{16\pi h^3}} \right|^2 \tag{2.37}$$

and

$$C_{sca,\parallel} = \frac{k^4}{6\pi} \left| \frac{(1 + r_{\parallel})^2 \alpha_p}{1 - \frac{\alpha_p \beta}{16\pi h^3}} \right|^2 . \tag{2.38}$$

2.3 Detection and demodulation

Having obtained a basic understanding of the interaction between the tip and the sample, it is necessary to discuss how the scattered field can be measured. Depending

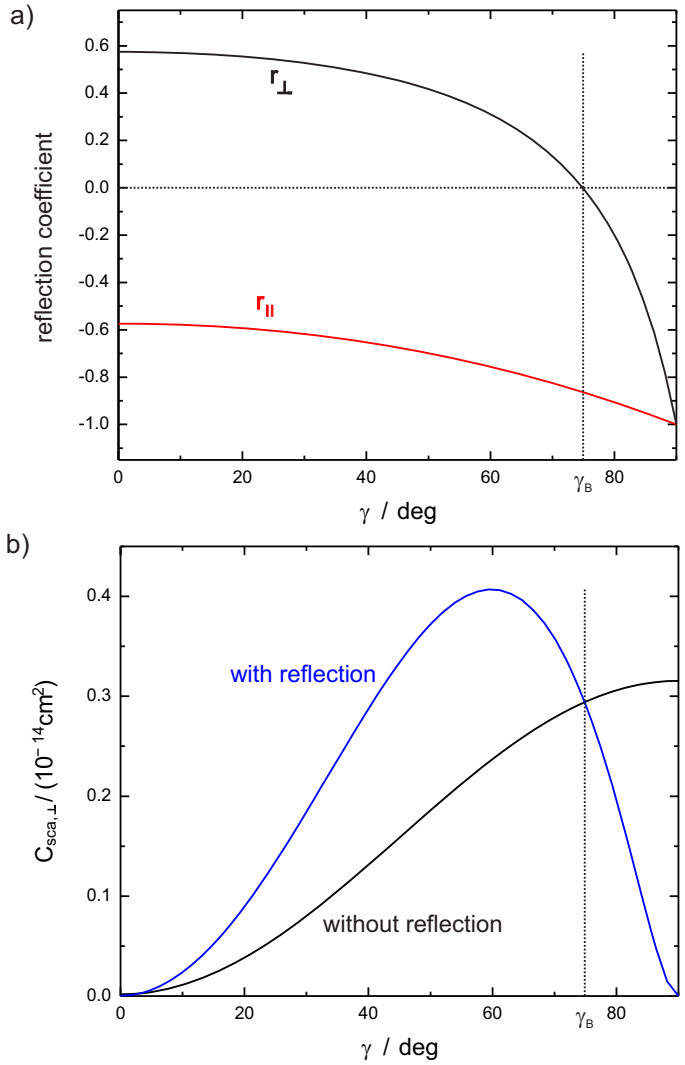

Figure 2.6: *Simulation of a) the reflection coefficients $r_\perp$, $r_\parallel$ and b) of the scattering cross-section $C_{sca,\perp}$ for a spherical PtIr-particle (radius $r = 10$ nm) above a silicon substrate ($\lambda = 633$ nm, $h = 10$ nm).*

on the quantity which is of interest, namely the electric field or the intensity, defined as the square modulus of the electric field

$$I_{sca} = |\mathbf{E_{sca}}|^2 , \tag{2.39}$$

it is possible to choose from different methods. For measuring the amplitude of scattered field directly, optical sampling methods like electro-optic sampling have proven to be versatile tools [Che03a, vR08]. But in most cases it is easier to measure the intensity of the signal and in combination with a phase measurement to subsequently calculate the scattered field amplitude.

Detection of the scattered light

No matter which technique is used, the first step is the detection of the scattered light. Since the tip-sample dipole exhibits a certain radiation characteristic [Bre08], it is not recommended to collect as much light as possible. In fact one would increase the background signal, while the pure near-field signal stays constant, hence decreasing the signal-to-noise ratio (SNR). A compromise has to be found, weighing the total signal against the pure near-field signal. One possible solution is to reduce the solid angle in which the light is collected and to focus on the direction of the lobes of the radiation pattern. For more needle-shaped tips Knight and Woods [Kni76] showed that these tips exhibit a remarkable antenna characteristic. For an antenna of 25 µm (typical length of the tip used in this work) and a wavelength of 10 µm such a lobe can be found around $\approx 30°$ against the horizontal plane which is $\approx 60°$ against the vertical. For example, figure 2.6 of the previous chapter reveals a strong increase in the scattering cross-section for incident angles around 60° against the vertical due to reflections on the sample surface. Making use of such a behavior allows one to increase the detectable near-field signal while keeping the background signal as low as possible, especially if measuring in the backscattering scheme. This means that the light is collected in the backward direction, thus avoiding to collect direct reflections (see figure 2.7a).

Higher-harmonic demodulation

The second step towards a pure near-field signal is to extract the near-field contributions from the scattered light. As already discussed, there are many sources for unwanted signals, like reflections at the sample surface or the shaft of the tip. Since the near-field signals are very small compared to the background, this noise (here the far-field contribution) will exceed the near-field components in a direct measurement. To get access to these signals, one typically uses so called higher-harmonic demodulation.

In figure 2.4 it has been shown that the scattering cross-section strongly depends on the distance between the scatterer and the sample. This effect can be exploited by modulating the tip-sample separation, hence modulating the near-field signal. Since the noise is based on macroscopic phenomena (far-field), the signal is almost not influenced if the distance modulation is small compared to the wavelength. In fact, the far-field only shows a linear dependence, whereas the near-field shows a strong nonlinear behavior. If the tip-sample separation is now modulated with a frequency Ω, this nonlinearity causes a modulation not only at the fundamental frequency Ω, but also at multiples $n\Omega$ with $n = 2, 3, ...$ which are called the higher-harmonic frequencies (see figure 2.7b). Demodulating the measured amplitude signal at such a higher-harmonic frequency yields the pure near-field amplitude, while the background is effectively suppressed.

In an experiment the demodulation is performed by a lock-in amplifier. To obtain the higher harmonics theoretically, one uses the Fourier transformation of the scattering cross-section which is proportional to the measured signal. Assuming a spherical particle/tip with a scalar polarizability α_p and an incident field which is perpendicular

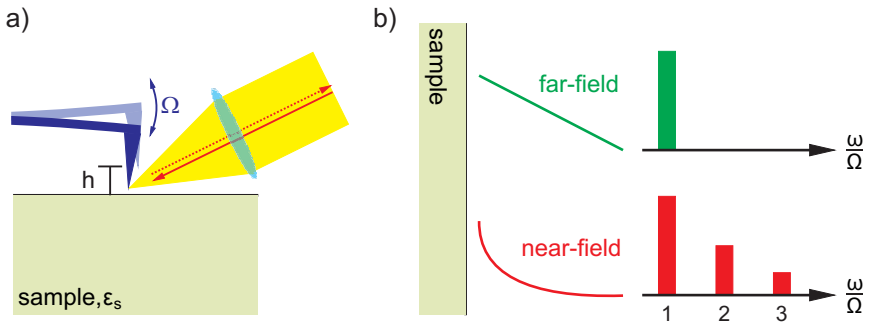

Figure 2.7: *a) Sketch of the detection setup when the light is collected in the backward direction. Illumination and detection takes place with the same lens. b) Background suppression: due to components at multiples of the fundamental frequency, the near-field can be extracted by higher-harmonic demodulation.*

to the sample surface then the cross-section is expressed by (see equation (2.28))

$$C_{sca,\perp} = \frac{k^4}{6\pi} \left| \frac{(1+\beta)\alpha_p}{1 - \frac{\alpha_p \beta}{16\pi h^3}} \right|^2 . \tag{2.40}$$

In this equation h denotes the separation of tip and sample. This has to be substituted by a modulated tip-sample separation

$$h(t) = h_0 + A\,(1 + \cos \Omega t)\,. \tag{2.41}$$

Here h_0 is the separation at the lower turning point of the oscillation, A is the amplitude and Ω the oscillation frequency. The contribution of the n^{th} harmonic can then be obtained by calculating the corresponding Fourier coefficient H_n of the modulated scattering cross-section

$$H_n = \frac{\Omega}{\pi} \int_0^{2\pi/\Omega} C_{sca,\perp}\left(h(t)\right) e^{-i(n\Omega t)} \mathrm{d}t. \tag{2.42}$$

Amplitude and phase of the near-field signal can be recovered from this integral by calculating the absolute value and the argument of H_n, respectively.

The major drawback of this method is already indicated in figure 2.7b. With increasing order of n, the total signal amplitude decreases rapidly. Hence, it is not possible to demodulate at an arbitrary harmonic to reduce the background to almost zero. Again a compromise has to be found. Typically one measures the second and third harmonic, as they offer a sufficient signal level while the background is almost negligible.

Interferometric Detection

Measuring solely the intensity yields another disadvantage. Since the intensity is the square modulus of the scattered electric field, only the amplitude of the field is recorded

(see equation (2.39)). The information about a possible phase shift with respect to the incident field is lost during the measurement. Furthermore, Gomez *et al.* [Gom06] showed that it is not possible to avoid that the scattered field $\mathbf{E_{sca}}$ interferes with the background field $\mathbf{E_b}$ generated by reflections, yielding constructive and destructive interferences. This is sometimes called self-homodyning and is shown in figure 2.8a. The fact that the phase relation between these fields can change during a measurement, aggravates the interpretation of the amplitude signal as long as the phase is not controlled. This has already been discussed and demonstrated experimentally in Ref. [Aub03]. But the unknown phase can be determined, if an additional field of fixed phase is allowed to interfere with the scattering field. If this reference field $\mathbf{E_{ref}}$ has the same frequency as the scattered field, it is called homodyne interferometry which is depicted in figure 2.8b. In the case that the reference field is additionally modulated by shifting the frequency, for example with an acousto-optical modulator, it is called heterodyne interferometry. As this is difficult at longer wavelengths, for example in the infrared, another modulation technique has evolved which is called pseudo-heterodyne or phase-shifting interferometry [Oce06, Deu08]. Instead of shifting the frequency of the reference arm, the phase is altered sinusoidally (see figure 2.8c).

In the case of self-homodyning (see figure 2.8a) it is assumed that the scattered field and the background field can be written as

$$\mathbf{E_{sca}} = |\mathbf{E_{sca}}|\, e^{i(\omega t+\varphi_{sca})} \tag{2.43}$$

$$\mathbf{E_b} = |\mathbf{E_b}|\, e^{i(\omega t+\varphi_b)}. \tag{2.44}$$

In these equations $|\mathbf{E_{sca}}|$ and $|\mathbf{E_b}|$ are the amplitudes of the fields and φ_{sca} and φ_b are the corresponding phases. The intensity measured by the detector is then defined as the square modulus of the sum of the fields:

$$\begin{aligned} I &= |\mathbf{E_{sca}} + \mathbf{E_b}|^2 \\ &= |\mathbf{E_{sca}}|^2 + |\mathbf{E_b}|^2 + 2\,|\mathbf{E_{sca}}|\,|\mathbf{E_b}| \cos(\varphi_b - \varphi_{sca}) \\ &= I_1 + I_2 + I_3. \end{aligned} \tag{2.45}$$

Keeping in mind that only the scattered field $\mathbf{E_{sca}}$ is modulated by the tip oscillation, the term I_2 can be neglected as it is filtered by the higher order demodulation. Since the amplitude of the background field is usually much bigger than the amplitude of the scattered field, the term I_1 is small compared to I_3. Hence, the component I_3 dominates the signal at the detector and is recorded and demodulated. It is obvious that a change of the phase relation $\Phi = \varphi_b - \varphi_{sca}$, for example by a change of the background phase φ_b, alters the detected intensity significantly.

In figure 2.8b an additional reference field is introduced to solve this problem. It can be written as

$$\mathbf{E_{ref}} = |\mathbf{E_{ref}}|\, e^{i\left(\omega t+\varphi_{ref}\right)}. \tag{2.46}$$

Here $\mathbf{E_{ref}}$ and φ_{ref} are the amplitude and the phase, respectively, of the reference field.

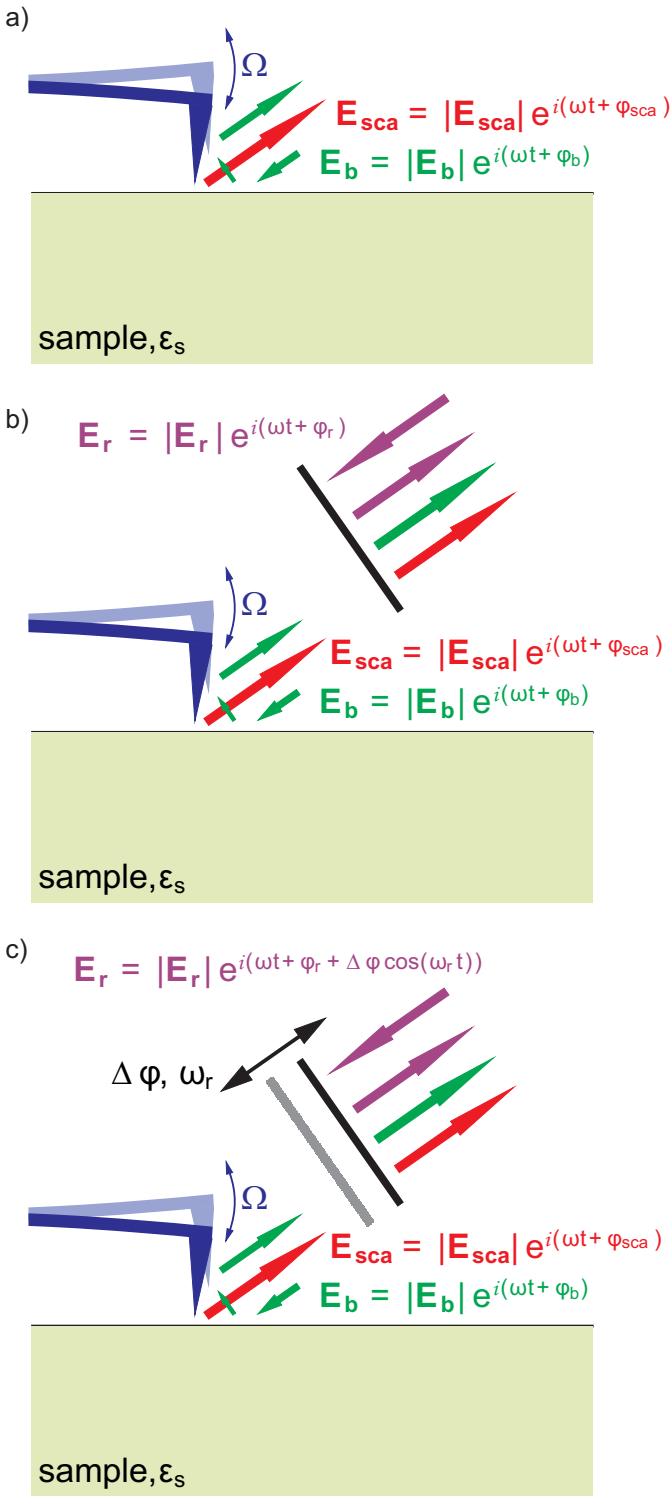

Figure 2.8: *Sketches of different measurement conditions. a) Uncontrolled interference between the scattered field and the background field. b) Homodyne interferometry by adding a reference beam with a fixed phase relation between reference and scattered field. c) Pseudo-heterodyne/phase-shifting interferometry due to a sinusoidal modulation of the reference arm length.*

The intensity at the detector now contains an additional component:

$$\begin{aligned} I &= |\mathbf{E_{sca}} + \mathbf{E_b} + \mathbf{E_{ref}}|^2 \\ &= |\mathbf{E_{sca}}|^2 + |\mathbf{E_b}|^2 + |\mathbf{E_{ref}}|^2 \\ &\quad + 2\,|\mathbf{E_{sca}}|\,|\mathbf{E_b}|\cos(\varphi_b - \varphi_{sca}) \\ &\quad + 2\,|\mathbf{E_{ref}}|\,|\mathbf{E_b}|\cos(\varphi_b - \varphi_{ref}) \\ &\quad + 2\,|\mathbf{E_{sca}}|\,|\mathbf{E_{ref}}|\cos(\varphi_{ref} - \varphi_{sca}) \\ &= I_1 + I_2 + I_3 + I_4 + I_5 + I_6. \end{aligned} \tag{2.47}$$

Now only I_1, I_4 and I_6 have to be considered, as they are the only components which are modulated at the tip oscillation frequency. Again the amplitudes of the fields can be compared which reveals that I_1 and I_4 are much smaller than I_6, because the reference field usually originates directly from the incident field which is split at a beam splitter, yielding a much higher amplitude than the background field. Therefore only I_6 has to be considered. Since the phase of the reference field φ_{ref} is now fixed, changes in the intensity have their origin in a change of the scattering amplitude $\mathbf{E_{sca}}$ or in a change of the phase φ_{sca} of the scattered field. But amplitude and phase are still not distinguishable by a single measurement. There are at least two measurements necessary where the phase of the reference beam is shifted by $\pi/2$ in between. The measurements are then proportional to the cosine and sine from which amplitude and phase can be calculated, as it is done by Taubner *et al.* [Tau04].

If the reference field exhibits an additional modulation, as shown in 2.8c, it is possible to obtain the scattering amplitude and phase from a single measurement. In the visible this modulation is usually a frequency shift of the reference field. The interference signal then beats due to the mixing of the frequencies which can be demodulated using an extra lock-in amplifier. But in the infrared this is rather difficult, since the necessary frequency shift is technically more demanding. An easier approach is the modulation of the phase of the reference field [Deu08, Oce06]. In this case the field can be written as

$$\mathbf{E_{ref}} = |\mathbf{E_{ref}}|\, e^{i\left(\omega t + \varphi_{ref} + \Delta\Phi\cos(\omega_{ref} t)\right)}. \tag{2.48}$$

The term I_6 of equation (2.47) is still the dominating component, but exhibits now an extra modulation with the depth $\Delta\Phi$ and the frequency ω_{ref}:

$$I_6 = |\mathbf{E_{sca}}|\,|\mathbf{E_{ref}}|\cos(\varphi_{ref} - \varphi_{sca} + \Delta\Phi\cos(\omega_{ref} t)). \tag{2.49}$$

If the phase modulation depth $\Delta\Phi$ is small compared to other phase differences, then this expression can be simplified to

$$I_6 = |\mathbf{E_{sca}}|\,|\mathbf{E_{ref}}|\left[\cos(\varphi_{ref} - \varphi_{sca}) - \Delta\Phi\cos(\omega_{ref} t)\sin(\varphi_{ref} - \varphi_{sca})\right]. \tag{2.50}$$

Again this can be used to disentangle the phase and the amplitude of the scattered field, yielding the pure near-field amplitude and phase.

All kinds of the discussed interferometric measurements allow the separation of phase and amplitude of the scattered field. They have their specific advantages and disadvantages, but all offer the possibility to enhance the scattered field by a factor proportional

to the amplitude of the reference field. As the scattered field contains the near-field information, one has the chance to increase the signal-to-noise ratio by scaling the reference field amplitude.

2.4 Optical material contrast

In a measurement, it can be assumed that parameters like the tip condition, wavelength and power of the light source, as well as the tip-sample distance are constant. The scattering cross-section is then solely defined by differences of the dielectric function. Hence, this allows one to distinguish materials with different dielectric functions. To compare measurements, for example, at different wavelengths, on has to define a quantity that accounts for the signal intensities of the different regions A and B of the sample. This quantity is generally known as contrast and is defined as [Web34]

$$K = \frac{I(A) - I(B)}{I(B)}. \tag{2.51}$$

Here $I(A)$ and $I(B)$ are the intensities of an arbitrary sensible quantity at the positions A and B. The position B is emphasized, since it defines a background or a reference as it appears in the denominator. The contrast K reveals whether the intensity at position A is higher ($K > 0$) or lower ($K > 0$) than at position B. It also shows how much more or less signal one has obtained at position A. This amount is returned in units of the intensity at the position B. In the case of a near-field measurement, the measured intensity is proportional to the scattering cross-section C_{sca}. Hence, the equation can be written as

$$K = \frac{C_{sca}(A) - C_{sca}(B)}{C_{sca}(B)}. \tag{2.52}$$

Now the quantity K corresponds to an optical materials contrast, as it compares the amounts of scattered light at the positions A and B, defined by the values of the scattering cross-section at these positions. In this thesis, the term “optical contrast” will always refer to this equation, if not specially mentioned.

2.5 Summary

In this chapter the theoretical framework for s-SNOM has been presented. It was assumed that the apex of the scanning probe tip can be treated as a small sphere. The quasi-static dipole model was then used to describe the scattering behavior of this model system and to discuss the influences of the shape of the particle and of the polarization of the incident electric field. Furthermore the scattering cross-section was introduced as a measure for the amount of scattered light.

The model of an isolated particle was then extended by a sample filling the half space below the sphere. It was shown that the presence of the sample yields a distortion of the electric field of the particle which results in an enhanced scattering cross-section for the coupled system. Moreover, it was explained that this distortion depends on

the dielectric function of the sample, allowing the distinction of different materials by means of the near-field signal.

In the last sections of this chapter some critical issues of a near-field measurement were discussed. The impact of reflections at the sample surface was shown as well as methods to extract the near-field signal from the background. Especially the methods of higher harmonic demodulation and different interferometric setups were explained.

3 The free-electron laser

The following chapter discusses the working principle of a free-electron laser. By using classical electrodynamics it is shown how the electrons are excited to radiate spontaneously. The interaction of this spontaneously emitted light with the electrons in the beam is discussed afterwards, resulting in the understanding how the stimulated emission can occur in free-electron lasers. At the end of this chapter it is explained how the amplification of the light in the optical cavity is achieved and which impact the electron energy has on the gain.

3.1 Historical survey

The word *laser* is an acronym for *light amplification by stimulated emission of radiation* and describes the basic principle of all lasers with only seven words. In the common usage it refers to the concept of T. H. Maiman [Mai60], where the amplification is the result of a gain medium and the transition between bound electron states. Therefore a historic overview of lasers would start with Maiman. But free-electron lasers (FEL) differ from other lasers in this specific feature. So it is necessary to start the overview with the development of the first wigglers or undulators, which are the names for the light amplifiers in FELs.

It dates back to 1951, when H. Motz proposed and subsequently demonstrated an arrangement of magnets with alternating polarization to create radiation by fast electrons [Mot51, Mot53]. He named this device "undulator" and showed that magnetic fields can be used to obtain incoherent radiation in the visible and millimeter regime. Later he was able to demonstrate that an amplification of the radiation is also possible with this arrangement [Phi88]. Following this work, R. M. Phillips developed a device called "ubitron" [Phi60]. This is known as the first (low-voltage) free-electron laser [Bra90], operating at 10 cm to 5 mm with a power beyond 1 MW and an efficiency above 10 %. In the year 1970, John M. J. Madey proposed the first device called free-electron laser [Mad71]. Based on the studies of synchrotron-radiation sources, he developed a device for visible wavelengths and explained it theoretically by a quantum-mechanical approach. This made the device a laser by definition, a quantum-mechanical device based on stimulated emission from an inverted population of quantum-states of the electron beam. In the year 1976, Madey and his co-workers finally succeeded in amplifying the beam of a CO_2-laser with a 24 MeV electron beam and a 5 m long undulator [Eli76]. Only one year later they demonstrated laser oscillations at 3.5 µm by setting up mirrors around the undulator and using a 43 MeV electron beam [Dea77]. At the same time it was shown that is is more accurate to describe the free-electron laser using classical electrodynamics [Hop76]. Although the lasing of such devices was demonstrated, it was

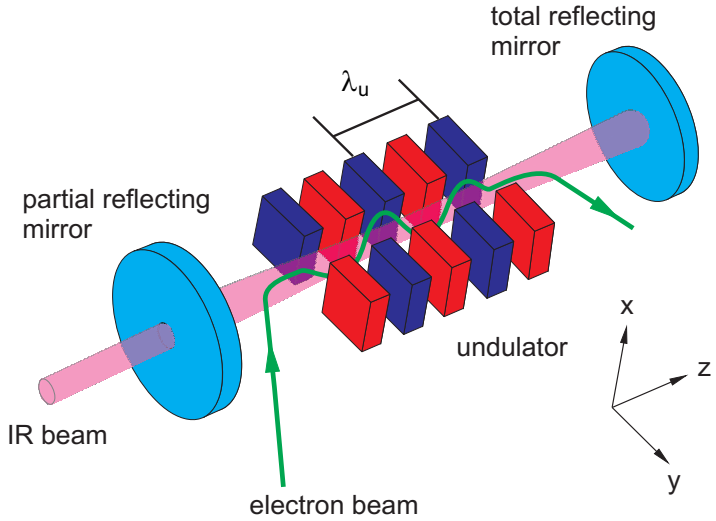

Figure 3.1: *Basic design of a free-electron laser, where an electron beam passes an arrangement of magnets with alternating polarization, called undulator. The electrons are forced to oscillate in transverse direction due to the Lorentz force, thereby emitting synchrotron radiation which bounces between the mirrors (optical cavity). With each pass of the undulator it interacts with the successive electrons and is amplified.*

not possible to obtain radiation in the visible spectrum until 1983. In this year the FEL at the electron storage ring ACO at Laboratoire pour l'Utilisation du Rayonnement Electromagnétique (LURE), in Orsay, France, started operations [Bra90].

Since then numerous FELs were built and operated successfully. Operation at ultraviolet wavelengths was also reported as well as high average powers. But since free-electron lasers are complex and expensive facilities, applications are limited to scientific research where users need tunability combined with high peak power. A more complete review of the history and the current status is given, for example, in Ref. [O'S01].

3.2 Basic principles

Conceptually, free-electron lasers are rather simple devices, consisting of a bunch of electrons moving in a magnetic field. This essential simplicity allows to describe the theoretical background in terms of classical electrodynamics and led to the phenomenon that the theoretical description preceded the experimental development, especially in the early days. The following discussion is analog to the ideas of reference [Bra90], where a full treatment of this issue is given.

Spontaneous emission

The basic configuration of a free-electron laser is shown in figure 3.1. The undulator consists of magnets with alternating poles, so that the magnetic field is reversed every half of the undulator period λ_u. In the illustrated case it is parallel or anti-parallel to

the y-axis. Hence, the magnetic field can be written as

$$\mathbf{B_u} = B_u \mathbf{e_y} \sin \frac{2\pi z}{\lambda_u}, \tag{3.1}$$

where B_u is the amplitude of the magnetic field and $\mathbf{e_y}$ is the unity vector in y-direction. Such a configuration is called a linear undulator, while it is called helical if the magnetic field exhibits an additional component in the x-direction. A beam of electrons with velocity $\mathbf{v}$ is then injected at one end of the undulator. The motion should be restricted to the z-axis, yielding

$$\mathbf{v} = v_z \mathbf{e_z}, \tag{3.2}$$

where $\mathbf{e_z}$ is the unity vector parallel to the z-axis. As they pass the undulator, they are forced to oscillate by the Lorentz force

$$\mathbf{F} = e\mathbf{v} \times \mathbf{B_u} \tag{3.3}$$

$$= -ev_z B_u \sin \frac{2\pi z}{\lambda_u} \mathbf{e_x}. \tag{3.4}$$

As a result of this oscillation, synchrotron light is emitted by the electrons each time they interact with the undulator field. Furthermore, it appears that the electron emit only in the forward direction. This is an already known relativistic phenomenon and can be explained by the different frames of observation: In the moving frame of the electron, the light is emitted in all directions, like the radiation of an antenna. In the stationary frame of the laboratory, where the electron velocity is almost the speed of light c, the radiation directed toward the sides cannot move very far from the undulator axis before the electron has moved further down the undulator. It appears that the emitted light is confined in a small cone around the axis of motion.

To calculate the wavelength of the emitted light, an observer is placed at the end of the undulator. The electrons move towards him and he will notice a higher frequency of the electron oscillation due to the Doppler effect. Considering the relativistic velocity of the electrons, it can be shown that the wavelength of the spontaneous emitted light is described by

$$\lambda_s = \frac{\lambda_u}{2\gamma^2} \text{ with } \gamma = \frac{1}{\sqrt{1 - \frac{v^2}{c^2}}}. \tag{3.5}$$

The Lorentz factor γ appears quadratic, as the electron sees the Lorentz contracted undulator period in the moving frame that has to be transformed into the stationary frame of the observer. But the expression has to be corrected by an additional term that considers the increased path length of the electrons due to their oscillation, so that equation (3.5) reads, for a linear undulator,

$$\lambda_s = \frac{\lambda_u}{2\gamma^2} \left[1 + \left(\frac{eB_u \lambda_u}{2\pi m_0 c} \right)^2 \right] \tag{3.6}$$

$$= \frac{\lambda_u}{2\gamma^2} \left(1 + K^2 \right), \tag{3.7}$$

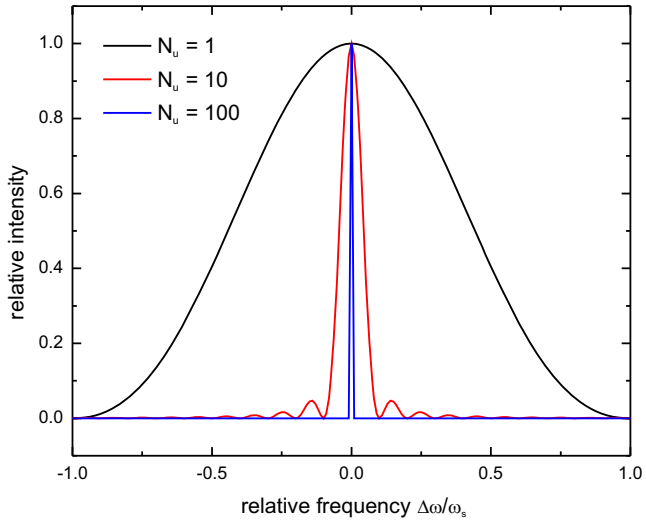

Figure 3.2: *Spectrum of the spontaneous emission by the electrons passing the undulator. It exhibits a characteristic linewidth that scales with* $1/N_u$.

where m_0 is the electron rest mass, e is the electron charge and K is the dimensionless undulator parameter.

From (3.6) and (3.7) it becomes obvious that the laser wavelength can be tuned by altering the electron energy, thereby changing the electron velocity. Another possibility is to change the amplitude of the magnetic field, which modifies the undulator parameter K. At the same time the spectral width of the emission line is limited by the number of undulator periods N_u, since this limits the number of oscillations in the wave packet emitted by an electron. To illustrate this, one calculates the intensity of the spontaneous emission at $\omega_s = 2\pi c/\lambda_s$ which is given as

$$I(\omega) \propto \left| \int_0^{N_u \lambda_s / c} e^{-i(\omega-\omega_s)t} \mathrm{dt} \right|^2 \tag{3.8}$$

$$\propto \left(\frac{\sin\left(\pi N_u(\omega-\omega_s)/\omega_s\right)}{\pi N_u(\omega-\omega_s)/\omega_s} \right)^2 . \tag{3.9}$$

In figure 3.2 the spectrum is plotted for different undulator periods. It can be seen that the spectra sharpen with increasing periods, yielding a linewidth below 1 % for $N_u > 100$. Hence, each undulator exhibibts a characteristic broadening of the emission line.

Up to now the discussion concentrated on the undulator as radiation source. The obtained radiation is comparable to the spontaneous emission in conventional lasers. It is weak and incoherent since the electrons passing the undulator are randomly positioned in the electron beam, with the result of random phases of the emitted waves with respect to each other. An amplification process is therefore not possible.

Stimulated emission of light

To understand the stimulated emission, the undulator is now placed between two reflecting mirrors. The spontaneously emitted electromagnetic wave is now able to oscillate between the mirrors, thereby passing the undulator. The electrons in the undulator interact with the electromagnetic field of the light which results in a bunching of the electrons. Due to the collective radiation of the electrons, the emitted light becomes coherent.

To discuss this bunching effect, an electromagnetic field is assumed to exist between the mirrors. It might be the beam of an external laser that should be amplified or the spontaneous emission of an electron that passed the undulator one moment ago. The electric field of the plane wave might be written as [Mil88]

$$\mathbf{E} = E_0 \left[\mathbf{e_x} \sin\left(\frac{2\pi z}{\lambda} - \omega t + \phi_0 \right) + \mathbf{e_y} \cos\left(\frac{2\pi z}{\lambda} - \omega t + \phi_0 \right) \right]. \tag{3.10}$$

As this bunching effect leads to a change of the electron velocity, it is interesting to calculate the different components of it. For this the magnetic field (3.1) of the undulator is extended by a component in the x-direction (helical undulator), as the mathematical description becomes easier. It reads

$$\mathbf{B_u} = B_u \left(\mathbf{e_x} \cos\frac{2\pi z}{\lambda_u} + \mathbf{e_y} \sin\frac{2\pi z}{\lambda_u} \right). \tag{3.11}$$

Solving equation (3.4) yields the equations of motion for the different components of the electron movement in the laboratory frame

$$\dot{v_x} = -\frac{e}{m_0} B_u v_z \sin\frac{2\pi z}{\lambda_u} \tag{3.12}$$

$$\dot{v_y} = \frac{e}{m_0} B_u v_z \cos\frac{2\pi z}{\lambda_u}. \tag{3.13}$$

Integrating these equations and considering the relativistic velocity of the electrons yields the components of the electron velocity in x and y direction

$$v_x = \frac{Kc}{\gamma} \cos\frac{2\pi z}{\lambda_u} \tag{3.14}$$

$$v_y = \frac{Kc}{\gamma} \sin\frac{2\pi z}{\lambda_u}. \tag{3.15}$$

With these equations the z-component can be calculated according to

$$\begin{aligned} v_z^2 &= v^2 - v_x^2 - v_y^2 \\ &= c^2 \frac{\gamma^2 - 1}{\gamma} - v_x^2 - v_y^2 \\ &= c^2 \left(1 - \frac{1 + K^2}{\gamma^2} \right). \end{aligned} \tag{3.16}$$

Since the velocity v is almost the speed of light, the Lorentz factor γ becomes very large. This can be used to simplify the last expression

$$v_z \approx c\left(1 - \frac{1+K^2}{2\gamma^2}\right). \tag{3.17}$$

Having all components of the velocity vector, it is possible to discuss the energy transfer between the electrons and the electric field. This is given by the power delivered or absorbed by the electric field

$$P = e\mathbf{E}\cdot\mathbf{v}. \tag{3.18}$$

Inserting equations (3.10), (3.14) and (3.15) yields

$$P = \frac{eE_0Kc}{\gamma}\sin\phi \tag{3.19}$$

with

$$\phi = 2\pi\left(\frac{1}{\lambda} + \frac{1}{\lambda_u}\right)z - \omega t + \phi_0. \tag{3.20}$$

Using Einstein's mass-energy-formula, equation (3.19) can be written as

$$P = \dot{W} = \frac{d}{dt}mc^2 = \frac{d}{dt}\gamma m_0c^2 = \frac{eE_0Kc}{\gamma}\sin\phi. \tag{3.21}$$

Differentiation yields

$$\dot{\gamma} = \frac{eE_0K}{\gamma m_0c}\sin\phi. \tag{3.22}$$

This corresponds to a rate at which the plane wave interacts with the electron. In the last step the change of the electron velocity along the undulator axis is now calculated. It is derived from the the first derivative of equation (3.17) with respect to the time

$$\dot{v_z} = \frac{d}{dt}c\left(1 - \frac{1+K^2}{2\gamma^2}\right) \tag{3.23}$$

$$= \frac{c(1+K^2)}{\gamma^3}\dot{\gamma}. \tag{3.24}$$

It is clearly visible that the electron gets accelerated or decelerated depending on whether it gains ($\dot{\gamma} > 0$) or loses ($\dot{\gamma} < 0$) energy to the plane wave. Hence, the presence of the electromagnetic field between the two mirrors results in a redistribution of the electrons along the z-axis of the undulator. The faster electrons catch up the slower ones, yielding the phenomenon of bunching. Shortly after the injection of the electrons the electron beam therefore consists of bunches of electrons spaced by the optical wavelength. The electrons are now emitting in phase with respect to each other. The emission of the electrons is now coherent, stimulated by the presence of the incident optical field. That is the stimulated emission.

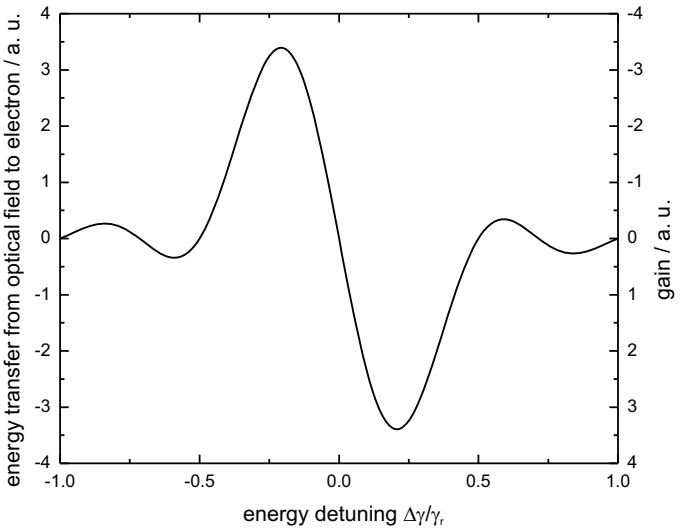

Figure 3.3: *Energy transfer from the optical field to the electrons in the undulator as a function of the energy detuning. Since the gain is an energy transfer from the electrons to the optical field, it exhibits the opposite sign (right ordinate axis).*

Amplification of the optical field

Up to now the energy/velocity of the electrons was only a parameter which determines the wavelength of the spontaneous emission. But it has a much more important effect concerning the gain of the optical field of a given wavelength λ_0. For this the resonance energy γ_r is defined as the electron energy where they emit exactly the same wavelength as the optical field. It is derived from equation (3.7) by replacing λ_s with λ_0 and solving this equation for γ

$$\gamma_r^2 = \frac{\lambda_u}{2\lambda_0}\left(1 + K^2\right). \tag{3.25}$$

The intensity of the spontaneous emission was already shown in figure 3.2 using equation (3.9). Using (3.25) the argument of (3.9) can be transformed into

$$\frac{\pi N_u(\omega - \omega_s)}{\omega_s} = \frac{\pi N_u \Delta\omega}{\omega_s} = \frac{2\pi N_u \Delta\gamma}{\gamma_r}. \tag{3.26}$$

The derivative of equation (3.9) with respect to $\Delta\gamma$ then yields the energy transfer from the optical field to the electrons and is illustrated in figure 3.3 [Mad79]. This is also known as the Madey theorem. The gain of the optical field corresponds to an energy transfer in the opposite direction, hence it has the opposite sign. From this figure it becomes clear that there is no gain for an electron energy equal to the resonance energy γ_r, although the microbunching leads to stimulated and coherent emission. It needs a slightly higher electron energy to achieve a positive energy transfer from the electrons to the optical field, resulting in a net gain. The electron thereby gets decelerated due to the energy loss. It is also visible in the figure how strong the detuning of the energy has to be, since the figure shows the situation for only one undulator period $N_u = 1$. In this case the electron energy is approximately 20 % larger than the resonance energy.

In general it is given by

$$\gamma \approx \left(1 + \frac{0.2}{N_u}\right) \gamma_r. \tag{3.27}$$

As the electron beam and the optical wave exhibit different velocities along the undulator axis, the position of the electrons bunches shifts continuously with respect to the traveling wave. This is known as the slippage. At the end of the undulator, when the electrons radiate most strongly, they have slipped to the end of the optical pulse. The result is a higher gain for the tail of the optical pulse than for the front of the pulse. Since the pulse performs several round-trips in the undulator, this leads to an asymmetric gain of the pulse. This can be compensated by shortening the optical cavity slightly, so-called *cavity detuning*, which leads to an improved microbunching and a uniform gain of the optical pulse.

Effect of high magnetic fields in the undulator

It has been shown in equation (3.7) that the wavelength of the free-electron laser can be tuned by changing the magnetic field of the undulator. Besides technical limitations, there are in principle no restrictions to the strength of the field. But with increasing field amplitude, higher harmonics of the emission frequency $\omega_s = 2\pi c/\lambda_s$ can occur. This can be used to increase the tuning range of the laser, but can also have negative effects, for example in SNOM experiments.

To understand the reason of the higher harmonics, the electron motion in a linear undulator field is examined again. It is assumed that the electron has only a velocity component parallel to the z-axis ($v_{z_0} \approx c$) when it enters the undulator. The Lorentz force then results in an additional motion parallel to the x-axis (see equation (3.4))

$$v_x = Kc \cos \omega_s t. \tag{3.28}$$

As this is proportional to the undulator parameter K, it exhibits a linear dependence on the undulator field. For strong magnetic fields the velocity component in x-direction is not negligible anymore. The result is an interaction of the transversal motion of the electrons with the magnetic field, yielding a further longitudinal velocity component due to the Lorentz force. Together with the initial velocity v_{z0}, the velocity parallel to the z-axis then reads

$$v_z = c\left\{1 - \frac{1}{2\gamma^2}\left[1 + K^2 - K^2 \cos 2\omega_s t\right]\right\}. \tag{3.29}$$

The electrons now oscillate slightly in z-direction while they move down the undulator. Viewing this motion in the frame of the electrons, the motion looks like a “figure-eight” [Bra90]. This results in a distortion of the emitted waves with a frequency of twice the undulator frequency, yielding the appearance of Fourier components at the fundamental frequency ω_s plus multiples of $2\omega_s$. These are the odd harmonics. Additionally, the even harmonics can occur, when the electron beam is slightly off-axis, so that it is not running exactly at the center.

Under certain conditions the gain for these harmonics can be higher than for the fundamental. This can be used to extend the wavelength range of the FEL to shorter wavelengths. But in SNOM experiments this is a very strong drawback, since the tip-sample system is then excited at different wavelengths, yielding an extremely complex near-field signal. Especially when investigating samples with one or more resonances, it has to be verified that the harmonics do not overlap with these resonances when off-resonance effects shall be examined.

3.3 Summary

This chapter provided a basic understanding of the working principle of a free-electron laser. It was shown that the the magnetic field in the undulator forces the electrons to emit synchrotron light due to the Lorentz force. The electric field of the emitted light then leads to an effect, called bunching, where the electrons are redistributed in the beam. The result is the stimulated emission by the electrons, since they then have a fixed phase relation with respect to each other. In the last sections it was finally discussed, how an amplification of the optical field can be achieved by increasing the electron energy with respect to the resonance energy and which effect high magnetic fields have on the emission.

4 Scanning Probe Microscopy

The subsequent chapter deals with the fundamentals of atomic force microscopy and of Kelvin probe force microscopy. The former is necessary for near-field optical microscopy, since it allows to bring the small scatterer close to the sample surface and to control the distance between them. The different operation modes are discussed as well as their influence on a near-field measurement. The latter is used to compensate surface charges which can have negative influence on the near-field signal. It will be shown how electrostatic forces act on the tip and sample and how they can by compensated.

4.1 Atomic Force Microscopy

It was discussed in chapter 2 that the scattering-type near-field optical microscope is based on the scattering of light at the apex of a scanning probe tip. The tip has to be in close proximity to the sample of interest which requires a technique that can control the tip-sample distance in the nanometer-regime. In the present work this is done using an atomic force microscope. Hence, it is reasonable to have a closer look at the physics of this technique.

The atomic force microscopy is the second scanning probe technique developed by Binnig *et al.* [Bin86]. It applies the motion of a cantilever of very small mass as a measure of interatomic forces, mainly covalent forces, van der Waals forces, electrostatic forces and magnetic forces. These forces are described very well by the Lennard-Jones potential, explaining the long-range attractive components and the short-range repulsive components. Since these forces are very weak ($< 10^{-9}$ N), the cantilever has to be as soft as possible. On the other hand, it is necessary that the cantilever exhibits a high resonance frequency so that unwanted vibrations do not influence the measurement. The resonance frequency f_0 is thereby given as [Sch06]

$$f_0 = \frac{1}{2\pi}\sqrt{\frac{D}{m_{eff}}}, \tag{4.1}$$

where D is the spring constant and m_{eff} is the effective mass of the cantilever. It is clear that to maintain a high frequency, the mass of the cantilever has to be reduced in the same order as the spring constant is reduced. This is achieved by decreasing the size of the cantilever. For example, a cantilever made of silicon (Young's modulus $E = 1.69 \times 10^{11}$ N/m^2, density $\rho = 2.33 \times 10^3$ kg/m^3) with the dimensions length $l = 225$ µm, width $w = 38$ µm and thickness $t = 7$ µm (standard cantilever used in this work) has a spring constant of [Mey92]

$$D = \frac{Et^3w}{4l^3} = 48\,\frac{\mathrm{N}}{\mathrm{m}}, \tag{4.2}$$

resulting in a resonance frequency of approximately 190 kHz. This is high enough to suppress, for example, influences by the building's vibrations.

There are different modes to operate an atomic force microscope, namely static modes (contact modes) and dynamic modes (non contact modes). Thereby the static modes are distinguished in *equiforce* and *variable deflection*, while dynamic modes are separated in *variable gradient* and *constant gradient*.

In the contact modes, the cantilever bends according to the forces acting on the tip, until an equilibrium is reached. As the deflection is described by Hooke's law, it is proportional to these forces with the proportional constant being the spring constant of the cantilever. In the *equiforce* mode a feedback loop keeps the tip-sample distance constant while the sample is scanned. Thus, the deflection of the cantilever is constant. The recorded height profiles then represent the topography of the sample. In the *variable deflection* mode the feedback loop is open, so that the tip-sample distance changes with the topography of the sample, resulting in a variable lever deflection. The topography is then derived from recording the bending of the cantilever.

In the non contact modes, the cantilever oscillates close to its resonance frequency. The resonance curve is thereby shifted by a distance dependent force acting on the lever. In first approximation it is the force gradient $F' = \partial F/\partial z$ which shifts the resonance frequency. Hence, a new effective spring constant can be defined as [Mey92]

$$D_{eff} = D - \frac{\partial F}{\partial z}. \tag{4.3}$$

The resonance frequency then reads

$$f_0 = \frac{1}{2\pi}\sqrt{\frac{D_{eff}}{m_{eff}}} = \frac{1}{2\pi}\sqrt{\frac{D - \frac{\partial F}{\partial z}}{m_{eff}}}. \tag{4.4}$$

If an repulsive force ($F' < 0$) acts on the tip, then the resonance frequency is increased whereas an attractive force ($F' > 0$) lowers it. This can be used to control the tip-sample distance with a feedback loop. If the amplitude of the lever is kept constant by varying the tip-sample distance, it is called amplitude-modulated (AM-) AFM. Here, a shift of the resonance frequency causes a decrease of the oscillation amplitude, as the excitation frequency is not adapted to the changed resonance (see figure 4.1). The amplitude variations are then interpreted as the topography. In the case that the excitation frequency is tracking the resonance frequency it is called frequency-modulated (FM-) AFM. Here, the topography is derived from the frequency shift, which allows an additional controller to maintain a constant oscillation amplitude. In a near-field experiment the FM-mode should be preferred as it keeps the scattering condition constant, since a change of the oscillation amplitude would cause a change of the mean tip-sample separation which then alters the scattering cross-section (see chapter 2.2) [Bil06].

There are a variety of methods to detect the bending of the cantilever. This can be done, for example, by the measurement of the tunneling current, the capacitance or of an interferometric signal. The most common method is the beam deflection method,

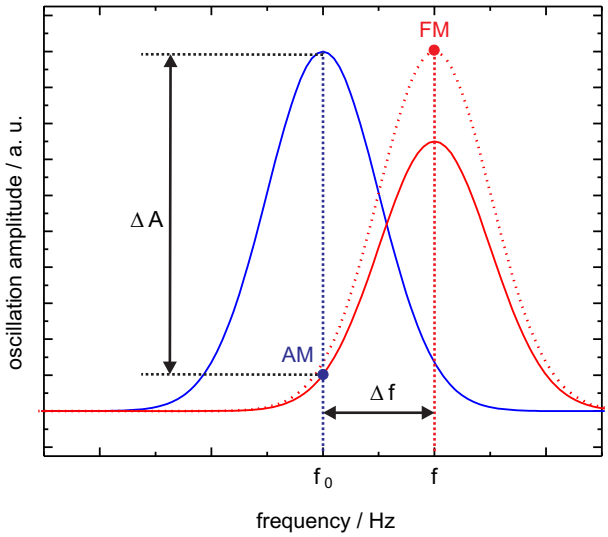

Figure 4.1: *Resonance of the oscillating cantilever with sample interaction (solid red line) and without (solid blue line). The sample induces a shift of the resonance frequency f_0 to the new frequency f and a decrease of the amplitude. As the excitation frequency in the AM-mode is fixed to f_0, the working point for the AM-mode is far of the resonance (blue dot). In the FM-mode, on the other hand, the excitation frequency is adapted to the frequency shift so that the cantilever is always excited at its (altered) resonance frequency. An additional controller ensures a constant oscillation amplitude (dotted red line), so that an optimal working point is given (red dot).*

where the beam of a laser is focused on the back of the lever and is reflected back onto a positioning sensing device, for example a four-quadrant photodetector [Ale89]. The deflection causes a shift of the laser spot on the photodetector, so that a certain quadrant collects more light than the others. The difference of the signals from the top quadrants and the bottom quadrants represents the oscillation of the lever, while the difference between the left and right quadrants represents a torsion.

4.2 Kelvin probe force microscopy

The previous chapter showed that different forces influence the oscillation of the cantilever. From these forces only the electrostatic and magnetic forces are present in the long-range regime. As the cantilever used in this work is made from a non-magnetic material (Si), it is allowed to neglect the magnetic force. However, the electrostatic or Coulomb force can not be neglected, since surface charges due to the air moisture are always present and the attractive and repulsive forces between them influence the interaction between tip and sample. It was also shown already that the near-field signal depends strongly on the separation of tip and sample. Hence, the electrostatic forces can influence the near-field signal, leading to artifacts induced by a wrong cantilever signal [Bil06]. Kelvin probe force microscopy (KPFM) [Lop04, Non91] is able to counteract these forces, although it was designed to measure the work function of a metal

or the surface charges on an isolated sample.

KPFM applies the capacitor method of Lord Kelvin [Kel98] which he used to measure the contact potential difference of two metals. The method is based on two conductors arranged as parallel plates with a small gap in between. The contact potential is then given by

$$U_{CPD} = \frac{1}{e}\left(\Phi_1 - \Phi_2\right), \tag{4.5}$$

where e is the electron charge and Φ_1 and Φ_2 are the work functions of the two conductors. When the distance between the plates is varied periodically, a current

$$I(t) = U_{CPD}\omega\Delta C\cos\omega t \tag{4.6}$$

can be measured. ΔC is the change in capacitance and ω the frequency of the distance variation. To measure the contact potential U_{CPD} an additional dc voltage is applied between the two plates, so that the resulting current is zero. In this case the dc voltage is equal to the contact potential. If the work function Φ of one of the metals is known then the work function of the second metal can be calculated.

In an AFM one of the metal plates could be the cantilever. To ensure conductivity the silicon tip is metal-coated. The second conductor is the sample. Both interact via the electrostatic force given by [Che03b]

$$F = -\frac{1}{2}\frac{\partial C}{\partial z}U_{CPD}^2. \tag{4.7}$$

This force results in an additional modification of the cantilever oscillation. According to the previous paragraph it is possible to compensate this force by applying a dc voltage $U_{K,0}$ between tip and sample.

In an experiment an ac voltage U_K is applied sinusoidally between tip and sample so that the electrostatic force is modulated and can be measured by lock-in techniques. The modified cantilever signal is then fed into a feedback loop which nullifies the influence of the electrostatic force by applying the compensating dc voltage $U_{K,0}$.

Part II

Setup of a permanent SNOM at ELBE

5 Infrared radiation sources

While the previous part of this thesis provided the theoretical background of the applied techniques and concepts, the next part will describe the experimental setup. In this context, the following chapter presents the infrared radiation sources used in this work. At the beginning the FELs are explained in detail and characterized in terms of emission, polarization and beam-profile. Later on, the second source, a commercial table-top carbon dioxide laser, is introduced.

5.1 Free-electron lasers U27 and U100

The main sources of infrared radiation for the developed SNOM are the two free-electron lasers U27 and U100 at the Forschungszentrum Dresden-Rossendorf, whose technical specifications are listed in table 5.1. They are combined with the linear accelerator ELBE (**E**lectron **L**inear accelerator for beams with high **B**rilliance and low **E**mittance) which delivers the necessary electron beam. Based on superconducting rf-acceleration cavities, it provides electrons with energies up to 40 MeV at a repetition rate of 13 MHz. These electrons are injected into the undulators U27 and U100, which are named according to their undulator period λ_u.
Using the information from table 5.1, the emission wavelengths of the undulators can be calculated using (see chapter 3)

$$\lambda = \frac{1 + K^2}{2\gamma^2}\lambda_u, \tag{5.1}$$

where γ is the electron energy in units of the electron rest mass. This is illustrated in figure 5.1. The emitted wavelength is plotted as a function of the undulator parameter K and the electron energy E_e^{kin} for both undulators. The U27 is usable between 4 µm and 22 µm, whereas the U100 delivers far infrared light between 18 µm and 250 µm. For this purpose the U100 utilizes a partial waveguide in the gap between the poles of the magnets to allow the pass of radiation above 40 µm. This is not necessary for the shorter wavelengths of the U27.

		U27	U100
Undulator period	λ_u	27.3 mm	100 mm
Number of periods	N_u	2×34	38
Undulator parameter	K	0.3 - 0.7	0.5 - 2.7

Table 5.1: *Specifications of the undulators U27 and U100.*

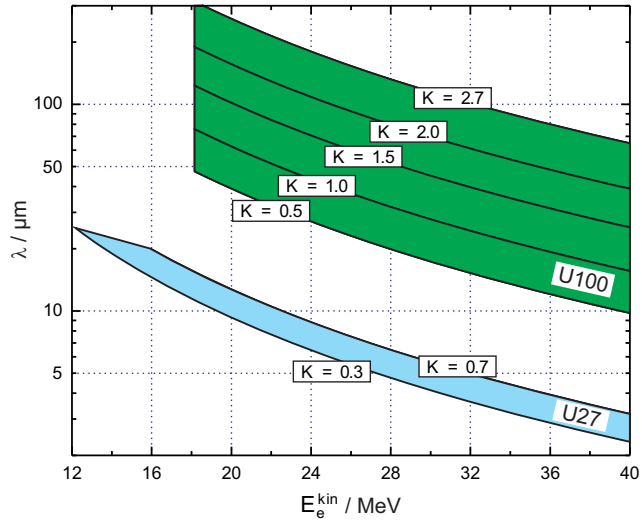

Figure 5.1: *Emission wavelengths of the undulators U27 and U100 as function of the undulator parameter K and the electron energy* E_e^{kin}.

Each undulator is situated in a separate optical resonator. The length of them is determined by the electron repetition rate to ensure that the circulating optical pulse overlaps with the following electron pulse. According to this restriction both resonators are 11.53 m in length. The specifications of the resonators are given in table 5.2. The average power emitted by the lasers thereby varies between 0.1 W and 40 W which strongly depends on the used outcoupling hole. Experiments have shown that the power drops with increasing hole diameter for the U27, while it rises with increasing hole diameter for the U100. The possible hole diameters are also given in table 5.2.

Beam characteristics of the U27

After these more general information about the two FELs, a more detailed characterization of the radiation of the U27 is given now. Due to the nature of the investigated samples, the main work in this thesis was done with this undulator.

As denoted in table 5.1, the U27 consists of a total of 68 periods of permanent magnets. As the linewidth of the emission scales with the number of periods (see figure 3.2), it can be expected that the U27 exhibits a spectral width of approximately $1/68 = 1.5\,\%$. Measurements showed that this estimation is almost correct. In fact, the width is slighly smaller than this for longer wavelengths, as the absolute linewidth is almost independent of the emission wavelength. The absolute width varies between 60 nm and 140 nm, so that the relative spectral linewidth drops with increasing wavelength as depicted in figure 5.2. Moreover, the spectral width of the emission can be tuned slightly by shortening the optical cavity [Ste06, Kni96], so that the smallest possible linewidth can be assumed for the near-field measurements. This also simplifies the comparison with theoretical results since it is not necessary to calculate near-field effects for a broad spectral excitation of the tip-sample system.

The polarization of the emitted light is predetermined by the electron orbit in the

			U27	U100
Resonator length		L_R	11.53 m	
Mirror radius of curvature	M1	R_h	5.94 m	6.33 m
		R_v		3.61 m
	M2	R_h	5.94 m	6.33 m
		R_v		∞
Mirror diameter	M1	horizontal	7 cm	13 cm
		vertical		17 cm
	M2	horizontal	7 cm	13 cm
		vertical		1 cm
Outcoupling hole diameter			1.5 mm	2.0 mm
			2.0 mm	4.5 mm
			3.0 mm	7.0 mm
			4.0 mm	

Table 5.2: *Specifications of the optical resonators for the undulators U27 and U100.*

undulator [Pap96]. Because both undulators at the Forschungszentrum exhibit a linear magnetic field, the electron orbit is planar. Thus, the light is linearly polarized, parallel to the plane of motion. In the case of the U27, this plane is horizontally orientated, so that it emits horizontally polarized light. In the notation of chapter 4 this means s-polarized (parallel to sample surface). The polarization characteristic is shown in figure 5.3, where the transmission of the beam is measured with a free-standing wire grid filter in dependence of the angle α between the grid and the optical table. The maximum of the transmission can be found at an angle of 90° against the plane of the optical table. Hence, the beam is horizontally polarized, since only an electric field perpendicular to the grid can pass the filter. Furthermore, the beam exhibits a perfect Gaussian shape directly behind the outcoupling hole (see figure 5.4a). The same is valid for the U100.

The U27 (as well as the U100) can be operated in three different modes, but only one is of interest for near-field measurements. One can choose from single pulse (< 10 ps) operation with repetition rate of a few kilohertz at most, macro pulse (bunch of pulses, > 100 µs) operation with maximal 25 Hz repetition rate or quasi continuous wave operation (quasi cw). This is the preferred mode for near-field measurements where the pulses occur continuously with a rate of 13 MHz defined by the accelerator.

Beamline

During the operation of the FELs, it cannot be avoided that additional ionizing radiation like Bremsstrahlung occurs. To shield the users from this radiation, the FELs are separated from the optical laboratories by thick concrete walls. The access to the infrared beam is granted by a system of mirrors which forwards the beam to the optical labs. This beamline is either operated under nitrogen atmosphere or under low

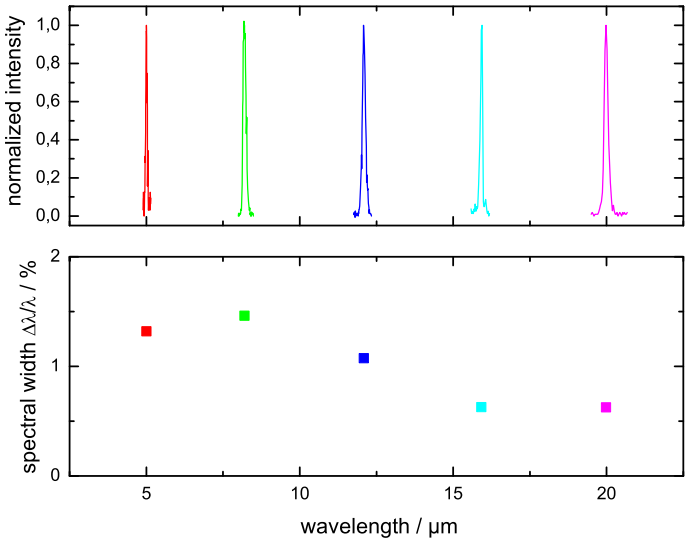

Figure 5.2: *Relative spectral width $\Delta\lambda/\lambda$ for different emission lines of the U27. The absolute linewidth is almost constant.*

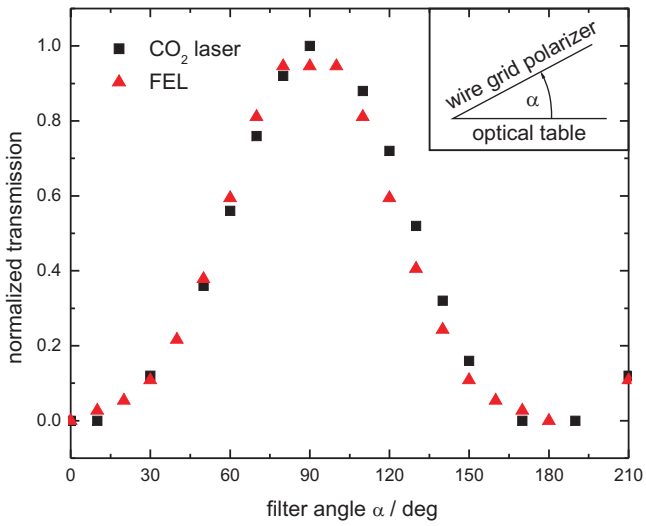

Figure 5.3: *Comparison of the polarization of the U27 and the table-top CO_2-laser.*

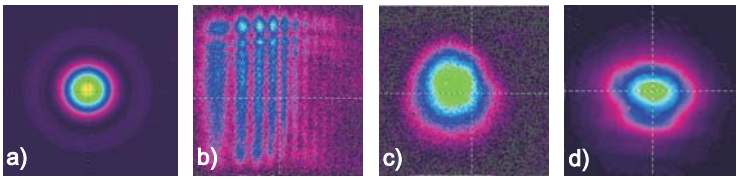

Figure 5.4: *Beam profiles for the U27 a)-c) and the CO_2-Laser d). a) Profile of the U27 directly behind the resonator. b) Phase front before the Gaussian filter. c) Profile after enhancement with the Gaussian filter.*

pressure. The beamline starts directly behind the FEL resonator and is sealed with a diamond window against the FEL vacuum. This windows is transparent for the complete range from 4 µm to 250 µm. In the laboratories the beamline is sealed with a window that has to be adapted to the requested wavelength. For the operation with the U27 the preferred windows are zinc selenide (ZnSe) or thallium-bromoiodide (KRS-5) in combination with the Brewster's angle to avoid losses due to reflections. When the U100 is used, the preferred window is a polymethylpentene (TPX) foil which provides a good transparency over a broad wavelength range in the far infrared. Regardless which FEL is operated, the laser beam leaves the beamline slightly convergent so that it exhibits a focus approximately 3.5 m behind the beamline window. Furthermore it was observed that the beam profile exhibit sometimes a more line shaped profile. The worst case is depicted in figure 5.4b. The reason is yet unknown and topic of further discussion. To restore the Gaussian profile, the beam can be directed through a Gaussian filter which is implemented in the optical setup leading to the near-field microscope. The Gaussian filter, also known as spatial filter, thereby focuses the beam which is then guided through a small pinhole. This pinhole has a very small diameter so that only the zero-order maximum of the diffraction pattern can pass. The beam is then expanded to its original diameter, but contains only the Gaussian mode. The profile is restored (see figure 5.4c).

5.2 Carbon dioxide laser

The second infrared radiation source for the experiments is a small table-top carbon dioxide laser. Manufactured by Access Laser Company it is a rf-driven laser source (LASY 4S), emitting between 10.3 µm and 10.8 µm. The typical operation mode is cw, but it can be chopped electronically with a maximum repetition rate of 200 kHz. The average power is almost 1 W with a temperature stabilized emission. Furthermore, by choosing the temperature setpoint, the emission wavelength can be changed between 8 lines in the given range. The emitted beam of the laser is slightly divergent and exhibits a Gaussian profile (see figure 5.4d). In order to allow the comparison of CO_2- and FEL-measurements, the linearly polarized beam of the carbon dioxide laser has been rotated with a half-wave retarder to match the polarization of the FEL (see figure 5.3).

6 The scattering-type near-field optical microscope

The following chapter describes the s-SNOM setup which was developed during this thesis. The requirements for the AFM and the optical setup introduce the corresponding sections and are followed by a discussion of the technical realization. Critical points like the interferometric measurement and the alignment of the setup are also presented in detail. The chapter is complemented by a performance check of the developed setup in respect to the topographic and optical resolution.

6.1 The atomic force microscope

The basis of the scattering-type near-field optical microscope is a home-built AFM whose main idea was an unblocked access to the tip-sample system for as many as possible different **k**-vectors. Furthermore it should allow the simultaneous measurement of the topography, the near-field signal and the Kelvin response of the sample. To achieve this, a design with a free-standing AFM tip was required, where the interaction zone of tip and sample is accessible by the laser beam without being shadowed by parts of the AFM. Furthermore it should apply a beam deflection method to control the tip oscillation, instead of shear-force or other methods.

The technical realization can be seen in figure 6.1. It offers a beam access of almost 180° in the horizontal plane and approximately 70° in the vertical plane. The scattering tip is spatially fixed with respect to the incoming beam. Instead of scanning the tip during a measurement, which would require a tracking of the laser focus, the sample is scanned below the tip. For this purpose the sample is mounted on top of a piezoelectric scanner[1] with a scan range of $40 \times 40 \times 4.3\ \mu m^3$ ($x \times y \times z$). The scanner itself is placed on a stack of piezoelectric slip-stick actuators[2] which allow a coarse movement of the sample and an automatic approach. The traveling range of the positioners is approximately 5 mm in the x, y and z direction, offering an accuracy of 50 nm.

The cantilever with the tip[3] is attached to the AFM head with the help of an alignment chip[4]. This chip exhibits three ridges which fit to the corresponding grooves on the backside of the cantilever. Due to this combination, it was possible to exchange the tip with a precision of less than 10 µm with respect to the maximum of the 3^{rd}-harmonic near-field signal, although the complete AFM head has to be lifted for the

[1] attocube systems AG, ANSxyz100
[2] attocube systems AG, ANPx101 and ANPz101
[3] NANOSENSORS, PPP-NCLPt
[4] NANOSENSORS, Align-10

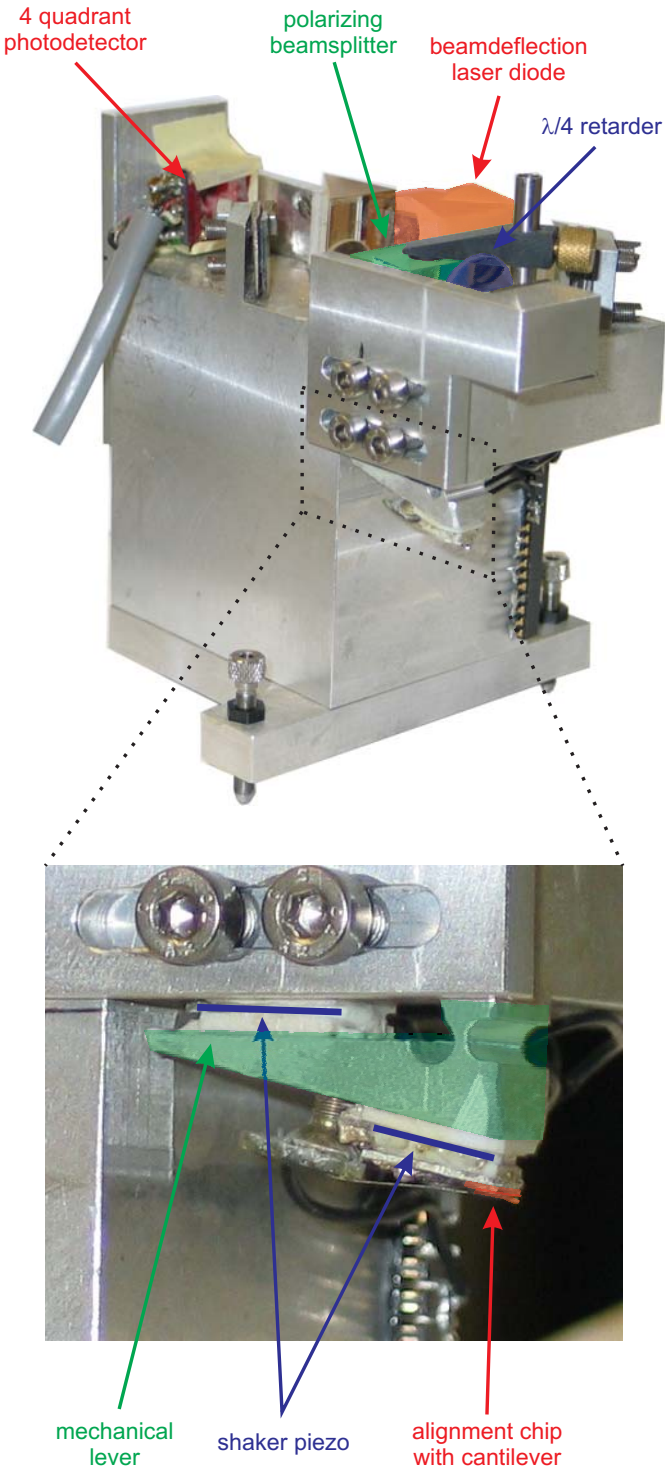

Figure 6.1: *Picture of the home built atomic force microscope without the sample holder.*

tip replacement procedure.

The oscillation of the tip is driven by a set of two piezoelectric shakers. The first one is situated directly beneath the alignment chip, the second one uses a mechanical lever to allow smaller oscillation amplitudes. To ensure electrical insulation from the applied voltage, the shaker piezo and the alignment chip are separated by a thin ceramic plate. The oscillation itself is monitored with a beam deflection setup, where the beam of a laser diode is focused on the backside of the cantilever and then reflected on a positioning-sensing device (PSD), a four-quadrant photodiode. Although the principle is very common, it is very critical with respect to the noise level during AFM measurements. To achieve low noise in the signals from the PSD, it is necessary to maximize the total signal on the PSD. The easiest way to achieve this, is increasing the laser output power. But this reduces the lifetime of the laser diode and could disturb the near-field measurement due to unwanted reflections of the beam deflection laser on the sample surface. A better way is to minimize the focus of the laser spot on the backside of the cantilever, so that almost the total laser power is reflected to the PSD. For this purpose the applied laser should have a Gaussian beam profile, since it offers a focus without optical errors and with that the smallest diffraction limited focus diameter. But Gaussian beam profiles are only achieved by single mode laser diodes. They would be suited very well, if they did not exhibit a high coherence length of the emitted laser light. This property causes unwanted interference effects between the reflected beam from the cantilever and parasitic reflections. This issue was already addressed by Fukuma *et al.* [Fuk05], but they also proposed a possible solution by modulating the laser power with a 500 MHz radio frequency. This would change the laser oscillation mode from single to multi-mode which results in a much shorter coherence length. However, in the present AFM this technique is not yet implemented. Instead of modulating the emission, a polarization dependent detection is used. For this purpose the output of the laser diode is reflected to the cantilever at the plane of a polarizing beam splitter. A quarter-wave retarder afterwards changes the polarization from linear to circular for the beam to the lever, and from circular to linear, but rotated by 90°, for the reflected beam. Since only light with the correct polarization can pass the beam splitter, it is ensured that parasitic light does not contribute to the signal on the PSD. Furthermore, a cover for the path from the beam splitter to the PSD eliminates background illumination.

The AFM can be operated in either static (contact) or dynamic mode (non-contact). In the dynamic mode, the signal of the photodiode is split into two signals. From these, the difference between the top and bottom quadrants is the equivalent for the oscillation amplitude of the lever. Hence, it is used as the input signal for the controller, whose task is to ensure a constant tip-sample separation and a constant oscillation amplitude. It directly acts on the the driving voltage of the shaker piezos and on the sample height. In combination with the x-y-z-scanner, the setup allows a stable operation with an oscillation amplitude below 10 nm and an oscillation frequency of approximately 140 kHz. The amplitude is increased to 50 nm during SNOM experiments to gain a better signal-to-noise ratio in the optical signal. The typical topographic resolution in the lateral direction is below 30 nm, but can be enhanced by strongly decreasing the

scan velocity. In the vertical direction it is below 2 nm and is mainly influenced by the tip condition and the oscillation amplitude.

In addition to the topographic information, the AFM always provides the electrostatic properties of the sample at the same time by Kelvin probe force measurement (see chapter 4.2). An ac-voltage is permanently applied between tip and sample. As the voltage has a direct influence on the tip-sample separation, it is measurable in the top-minus-bottom (T-B) signal of the PSD. Hence, the (T-B) signal is also fed into the KPFM controller, which nullifies the influence of the electrostatic forces on the tip-sample separation by applying an additional dc-voltage between tip and sample. Using the PSD-signal directly is called amplitude-sensitive (AM) Kelvin probe force microscopy [Lop04]. If the (T-B) signal is first demodulated at the cantilever oscillation frequency and then fed into the KPFM controller, it is called frequency-modulated (FM) Kelvin probe force microscopy, which is advantageous compared to the AM-KPFM [Lop05]. FM-KPFM is sensitive to the gradient of the electrostatic forces between tip and sample, whereas AM-KPFM only measures the force itself. As the gradient is more confined to the tip, FM-KPFM offers a higher lateral resolution. Both techniques can be realized with the built AFM. The typical frequency of the ac-voltage is 3 kHz with an amplitude of 1 V.

6.2 s-SNOM setup

Besides the AFM an optical setup had to be realized that allows wavelength independent operation of the near-field microscope. Especially when changing from mid-infrared to far-infrared, crucial elements of the setup, such as detectors or beam splitters, should be easy to change. Furthermore, the setup should minimize the alignment time when the radiation source is changed from FEL to CO_2. At last it should allow the interferometric detection of the near-field signal.

The optical setup is schematically illustrated in figure 6.2. It is solely based on reflection optics to account for the wavelength independent operation. Each mirror has a gold coating with almost 100 % reflectivity throughout the infrared and exhibits a diameter of 2 inch. From the first iris diaphragm, labeled with id, the beams of the FEL, the CO_2-laser and the alignment laser take the same optical path. By using flip mounts (fm) and separate alignment mirrors (am) for the different lasers, it is possible to change the source while keeping the beam focused on the tip. Flip mounts are also used for switching the polarization of the beam from horizontal (s-polarized) to vertical (p-polarized). An alternative beam path with an additional set of mirrors rotates the polarization of the beam by 90°. The next optical element is a beam splitter (bs) which directs a certain amount of the beam onto a powermeter (pm). As this splitter is situated behind the polarization switcher, a dependence on the splitting behaviour has to be considered. The beam is then fowarded to the second beam splitter which reflects the beam to the focussing mirror next to the tip and transmits the beam partially to the reference arm of the Michelson interferometer. The length of the arm can be altered by displacing the mirror at its end, since it is mounted on a piezo tube. The focussing mirror is situated on a piezo stage which allows the adjustment of the

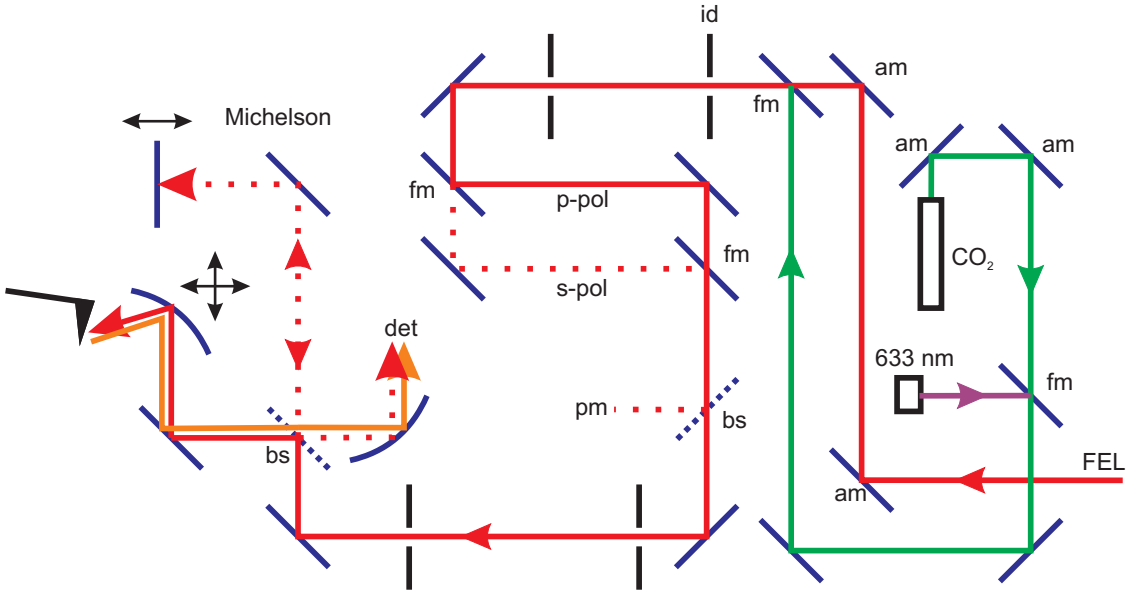

Figure 6.2: *Layout of the optical setup. Solid blue elements are mirrors, either parabolic or plane, while dotted blue elements represent beam splitters BS. The beam of the FEL is marked red and the beam of the CO_2-laser is green. id is the label for the iris diaphragms, while fm means flip mount. am denotes mirrors used for the beam alignment.*

mirror in all three directions (x, y and z). With this device it is possible to adjust the near-field signal by altering the position of the laser focus on the tip. The accuracy of the stage is approximately 1 µm which is controlled by a closed-loop position feedback along the axes. This focussing mirror illuminates the tip-sample system at an angle of 70° against the vertical and is also used to collect the backscattered signal from the tip. These signals are then forwarded to the beam splitter, where they are transmitted and superimposed with the beam of the reference arm. At the end both beams are focused on the detector (det). As for longer wavelengths absorption by air moisture becomes critical, it is possible to purge the entire setup with dry nitrogen.

As already mentioned, a few elements have to be adapted to the used wavelength. These are the beam splitters and the detector. For this reason, those elements are placed with the help of magnetic clamps and by a special detector holder. Small mirrors on flip mounts (not shown) facilitate the alignment of the changed elements. Furthermore, a set of different liquid nitrogen cooled mercury cadmium telluride detectors[5] (MCT) exist to cover the spectral range of the U27. Finally, different beam splitter materials can be used. These are polyethylene, polypropylene, zinc selenide and Mylar.

[5]Teledyne Judson Technologies

Phase controlled Michelson interferometer

In chapter 2 it was explained that the near-field signal is a complex quantity, described by an optical amplitude and an optical phase. To separate both quantities, the designed optical setup contains a Michelson interferometer. The beam path from the second beam splitter to the tip represents the interferometer path with the fixed length, while the transmitted beam is the reference arm with variable length. Both, the near-field signal and the reflected beam in the reference arm, are superimposed by the same beam splitter and then focused on the detector, where they interfere.

The principal concept of phase shifting interferometry was already topic of different publications [Deu08, Oce06]. But both groups have in common that they actually do not measure the optical phase. Instead they are calculating the phase from the obtained near-field amplitude signals when the reference phase is altered. This requires a lot of post processing and is very time consuming. An alternative and, in this context, more advantageous principle was invented by Stebounova *et al.* [Ste03]. Their aim was to maximize the near-field signal by an active control of the reference phase, so that the signals always interfere constructively. This approach was enhanced by M. Cebula [Ceb06], who interpreted the output of the phase controller as equivalent to the optical phase. While he suffered from technical problems and could not show the realization for near-field measurements, this principle was successfully implemented in the present setup.

In figure 6.3a the basic setup of the phase shifting Michelson interferometer is illustrated. A beam splitter divides the incoming beam into two parts. Under static conditions both paths have the same optical length, while during a measurement the length of the beam path in the reference arm is altered sinusoidal with a modulation depth of $\lambda/10$. For this purpose, the mirror is mounted on a piezo tube. This allows not only the movement of the mirror by extending and contracting of the tube, but also the alignment of the mirror by bending the tube. In combination with a kinematic mirror mount this allows a very fine adjustment of the mirror to achieve good interferences. The oscillation of the mirror during a measurement has a frequency of 50 Hz and an amplitude of 1.8 µm peak-peak. The beam which is reflected at the beam splitter is focused on the tip. The backscattered signals from the tip and the beam in the reference arm are superimposed by the same beam splitter and interfere on the detector.

In the previous part it was described, how the presence of a reference field alters the signal of the detector. It was shown in equation (2.50) that a phase modulation in the reference field also modulates the interference signal. This equation reads

$$I_6 = |\mathbf{E_{sca}}|\,|\mathbf{E_{ref}}|\left[\cos\left(\varphi_{ref}-\varphi_{sca}\right)-\Delta\Phi\cos\left(\omega_{ref}t\right)\sin\left(\varphi_{ref}-\varphi_{sca}\right)\right]. \tag{6.1}$$

To understand the working principle of the phase measurement, this equation shall be analyzed in detail. First of all it has to be recalled that the scattered field is modulated

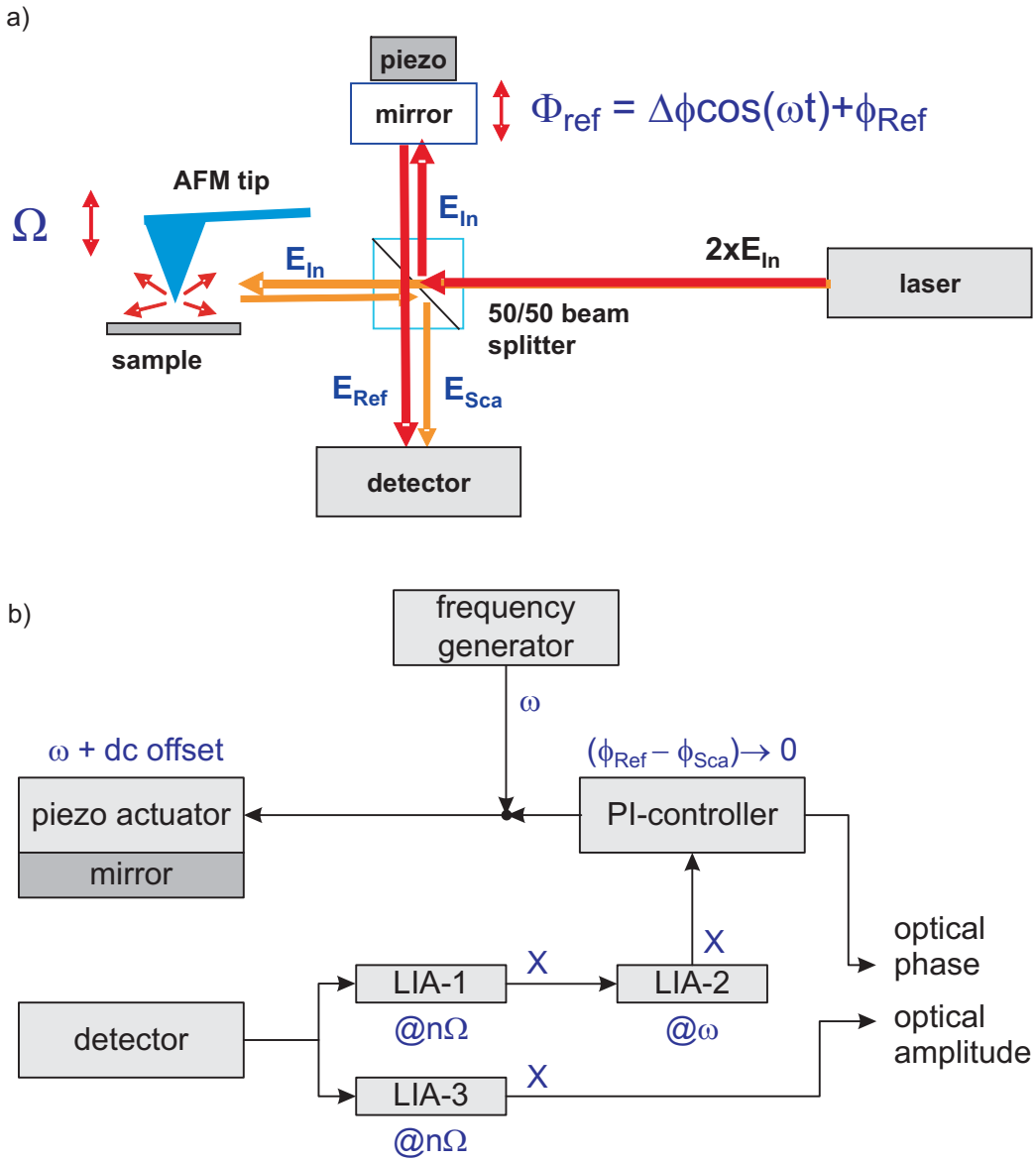

Figure 6.3: *Working principle of the phase shifting interferometer as conceived by M. Cebula. a) Setup of the Michelson interferometer. b) Scheme of the signal processing to obtain the optical phase information. A set of lock-in amplifiers (LIA) is used to evaluate the signal, which is then used as input for an analog proportional-integral (PI) controller.*

by the oscillation Ω of the tip. Hence, the equation can be expressed as a Fourier series

$$I_\Omega \propto |\mathbf{E_{ref}}| \sum_n s_{sca,n} \cos(n\Omega t) \bullet \\ [\cos(\varphi_{ref} - \varphi_{sca,n}) - \Delta\Phi \cos(\omega_{ref} t) \sin(\varphi_{ref} - \varphi_{sca,n})] \tag{6.2}$$

with $s_{sca,n}$ being the scattering amplitude. To gain access to the phase information, the signal is analyzed in two paths. This is illustrated in figure 6.3b. The first path

results in the optical phase $\varphi_{sca,n}$ of the n-th harmonic, the second yields the associated optical amplitude $s_{sca,n}$.

The signal from the detector is fed into the first lock-in amplifier (LIA-1 in figure 6.3b). It demodulates the signal with respect to the higher harmonic $n\Omega$ of the cantilever oscillation frequency. By choosing the harmonic at this lock-in, one can select the optical phase of the harmonic of interest. The lock-in operates with a short time constant compared to the mirror oscillation period, so that the ω_{ref}-modulated term persists in the Ω-demodulated signal. Hence, the X-output signal of the lock-in is equivalent to

$$I \propto s_{sca,n} \left[\cos\left(\varphi_{ref} - \varphi_{sca,n}\right) - \Delta\Phi \cos\left(\omega_{ref} t\right) \sin\left(\varphi_{ref} - \varphi_{sca,n}\right)\right]. \tag{6.3}$$

This signal is fed into the second lock-in amplifier (LIA-2), which demodulates the signal with respect to the mirror oscillation frequency ω_{ref}. The X-output reads

$$I \propto s_{sca,n} \sin\left(\varphi_{ref} - \varphi_{sca,n}\right). \tag{6.4}$$

This signal is sent into the phase controller. By displacing the reference mirror, it nullifies the input signal (6.4). As the position of the mirror corresponds to a certain reference phase φ_{ref}, an input signal of zero corresponds to the equality $\varphi_{ref} = \varphi_{sca,n}$. Looking at (6.3), this means that the sine vanishes and the cosine becomes 1, resulting in constructive interference of reference field and scattered field. Because the phase of the reference arm is constant (except when adjusted by the controller), the controller only reacts to changes of the optical phase $\varphi_{sca,n}$ which implies that the mirror-displacement voltage is a measure for the optical phase.

At the same time the amplitude is derived from a separate demodulation of the detector signal with an additional lock-in amplifier (LIA-3), using a comparatively long time constant. Alternatively the output of the first lock-in (LIA-1) can be fed into an appropriate high-pass filter (not shown) to eliminate the reference phase modulation.

The concept of this technique allows the measurement of optical phase and amplitude at the same time at the cost of a high technical effort. In principle, this system allows interferometric measurements at arbitrary wavelengths, as long as the necessary modulation depth can be realized with the piezo actuator. In the present setup, this limitation is approximately 20 µm, which theoretically corresponds to the full spectral range of the U27. But experiments with the interferometer in combination with the FEL were not successful, so the usage is limited to the carbon dioxide laser. The most significant problem thereby is the adjustment of the reference mirror to achieve strong interferences.

6.3 Alignment and performance

When operating a scattering-type near-field optical microscope, the most critical issue is the proper alignment of the optical parts of the system. Especially focusing the beam correctly onto the tip can determine whether results can be obtained at all. For this purpose it is useful to have some kind of step-by-step guide, but to cover all

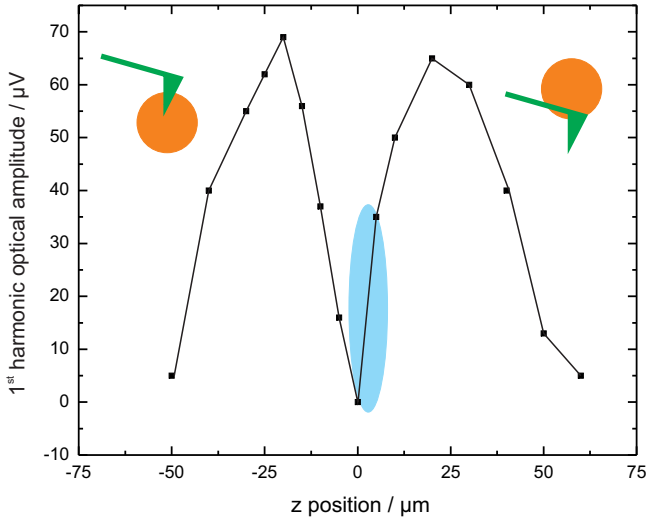

Figure 6.4: *Intensity of the 1^{st} harmonic optical amplitude as a function of the position of the laser focus. For $z = 0$, the center of the focus is at the apex of the tip, while it is below for $z < 0$. The focus position that yields a good higher harmonic signal is emphasized blue.*

details would go beyond the scope of this thesis. Therefore only some major points are discussed in the following.

Alignment for the near-field signal

First of all, the focus of the beam has to be positioned at the tip. A rough method can be the alignment with a visible laser, for example a helium-neon laser or a laser diode. The tip is positioned while imaging the beam behind the focus. Depending on the size of the focus a diffraction pattern or an image of the tip can be seen.

A far better method is measuring the demodulated optical amplitudes. At the beginning the beam is aligned so that a good signal of the 1^{st} harmonic is achieved. If the oscillating tip is properly adjusted, two peaks in the demodulated signal can be seen when changing the vertical position of the tip, like it is depicted in figure 6.4. The peaks indicate the two extremal positions of the tip at the upper and lower edge of the focus. This can be explained by the intensity gradient in the profile of the laser focus [Sch07b]. Due to this gradient, the signal is modulated much stronger near the edges of the spot than at the center, yielding a high amplitude in the demodulated signal. If the peaks are identified, the tip should be positioned near the minimum between the peaks, but slightly below the center of the focus. With this method it is also possible to obtain a rough estimate of the focus size. It is diffraction limited to 42 µm for a wavelength of 10.6 µm (numerical aperture of mirror = 0.12), but in most cases it is worse. Typically the spot is bigger than 50 µm. In the next step the sample is approached, and the signal is optimized in the 2^{nd} and 3^{rd} harmonic of the oscillation frequency. Ideally, the criteria for the alignment should be the signal of the 3^{rd} or even higher harmonics. Since it represents the pure near-field signal, it should

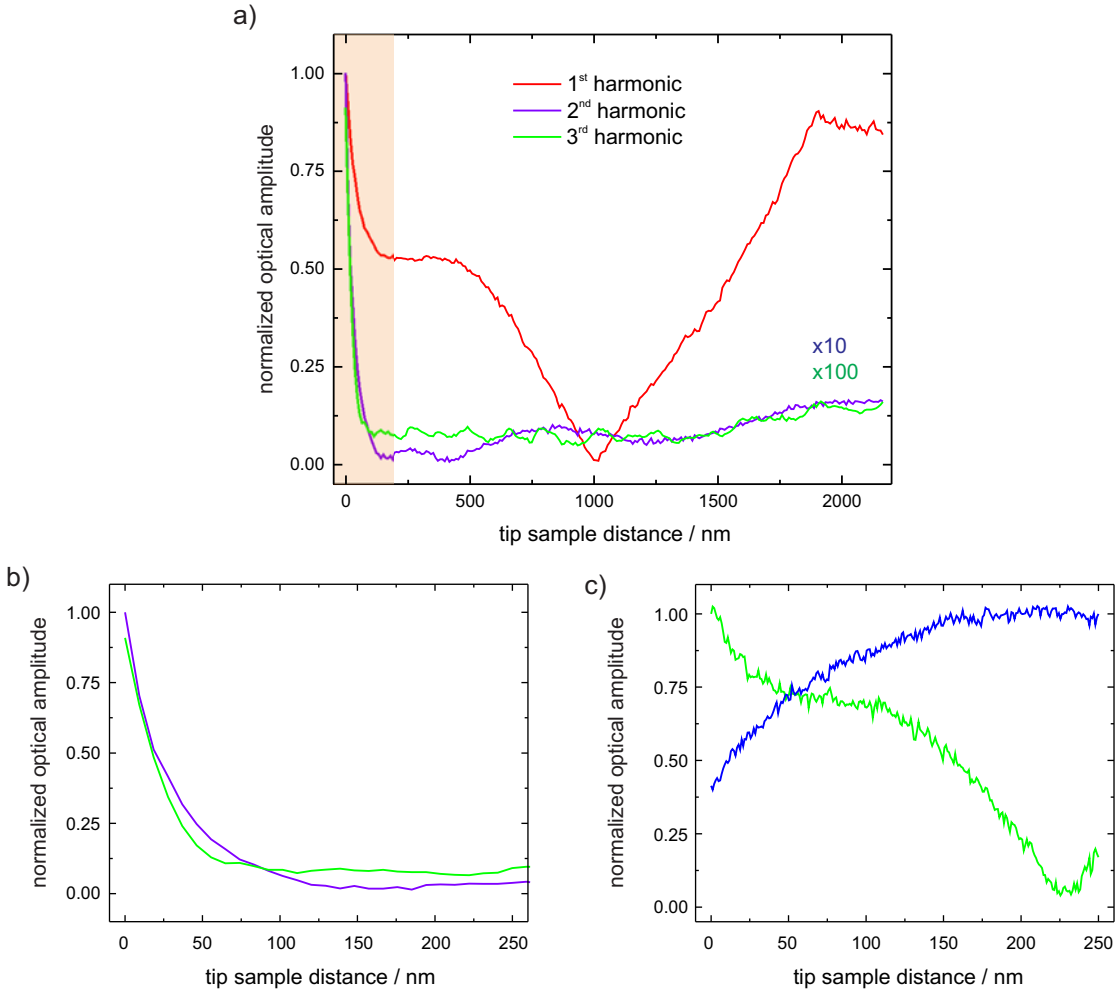

Figure 6.5: *Near-field signals of different harmonics measured on gold at* 10.6 µm *(p-polarized) for different alignments. a) 1st, 2nd and 3nd harmonic observed for a good alignment measured over* 2500 nm *with the near-field region highlighted. b) Magnification of a), showing the range from 0 to* 250 nm*. c) Same range as b), but for a very bad alignment.*

be maximized. Furthermore, the sample for the alignment should be non-resonant, for example a thin gold layer on top of a substrate. On a resonant sample it can occur that the maximum of the signal is observed not directly at the surface, but somewhere above [Sch07a]. That makes the alignment rather difficult. Finally, approach curves are measured, where the distance between tip and sample is reduced and the distance dependence of the near-field signal is recorded. The behavior of the different harmonics indicates the quality of the alignment.

Results of a good alignment can be seen in figure 6.5a. Here a gold film of approximately 100 nm thickness was illuminated at 10.6 µm. While the distance between tip and sample was reduced, the near-field signals of the 1^{st}, 2^{nd} and 3^{nd} harmonics were measured. It is visible that even the 1^{st} harmonic contains a near-field signal that stands out from the background. This background contribution is effectively sup-

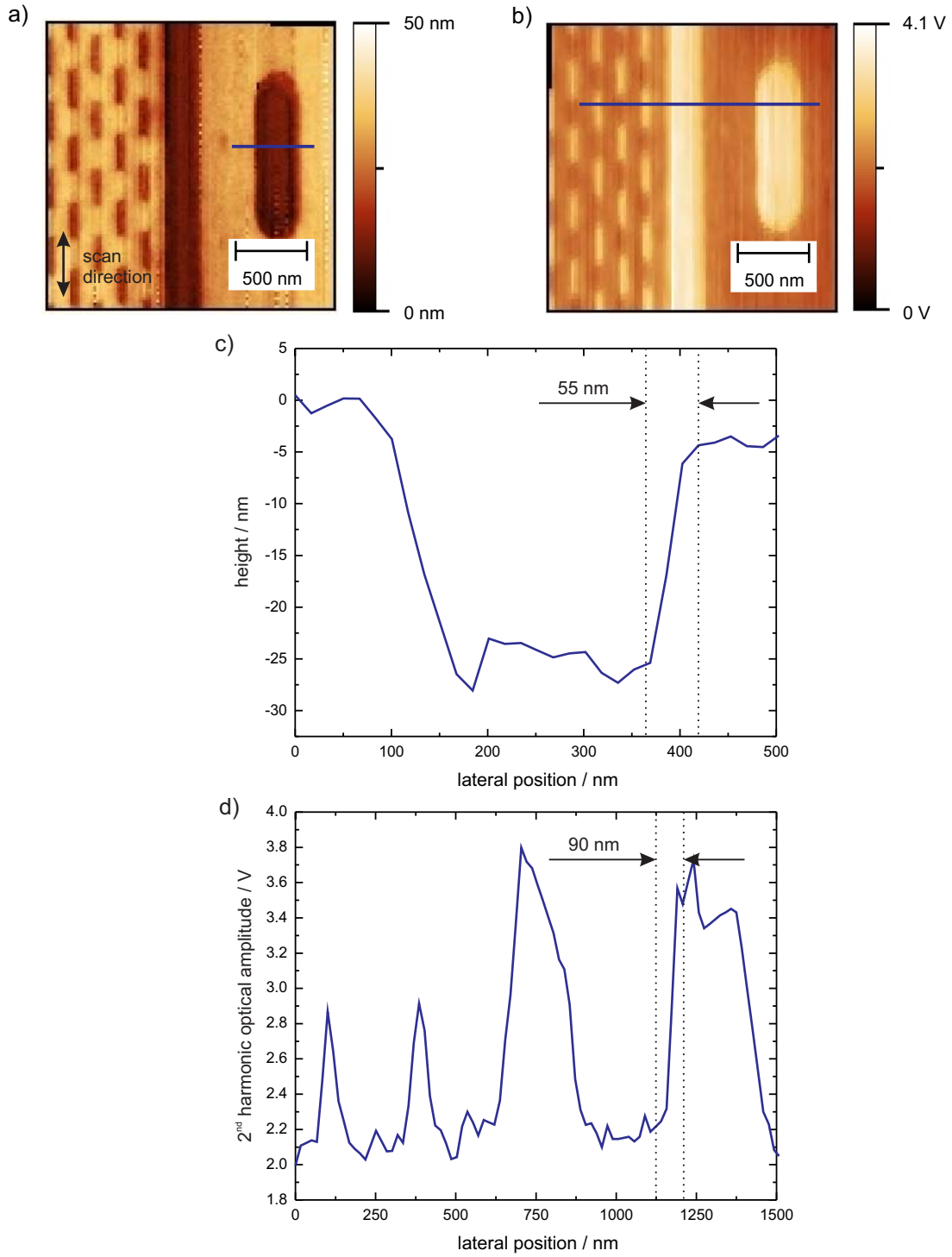

Figure 6.6: *Topographic and near-field optical resolution measured for a sample of SiO_2/Si with the CO_2 laser at* 10.6 µm *(p-polarized). a) Topography where the Si appears darker as it is below the SiO_2. b) Measured 2^{nd} harmonic optical amplitude of the same area. c) Profile along the blue line in the topography image, indicating a lateral resolution of* 55 nm. *d) Line profile from figure b), indicating an optical resolution of* 90 nm.

pressed in the higher harmonics. Figure 6.5b shows the same measurement but zoomed into the near-field region. The fast decay of the signal within 100 nm from the surface is a typical indicator for the near-field. In contrast, figure 6.5c shows the signals for a very bad alignment. Only the 3^{rd} harmonic shows a small near-field signal, while the 2^{nd} harmonic is dominated by a strong far-field.

If a proper alignment is achieved, the quality of the measurement depends on many parameters, but mainly on the oscillation amplitude, the tip condition and the scan velocity. A smaller velocity allows significantly more time for the signal demodulation and in turn less noise in the obtained images. A very good example for the capabilities of the developed system is shown in figure 6.6. The sample is a memory chip fabricated on a silicon wafer that was structured with a silicon dioxide mask. The SiO_2 is on top of the Si with a height difference of approximately 20 nm. The achieved topographical resolution is 55 nm which roughly coincides with the tip diameter. More interesting is the near-field optical resolution of about 90 nm and thus in the same order as the tip diameter. A higher resolution is theoretically not possible. It corresponds to approximately $\lambda/100$. Moreover, figure 6.6c shows that there are no topography artifacts in the optical image, otherwise the edges of the bright areas would be pronounced by a dark border.

Alignment of the interferometer

The alignment of the interferometer is performed in three steps. First, the AFM tip is replaced by a fixed mirror. The mirror has to be exactly in the focus of the parabolic mirror which normally focuses the light on the tip. Furthermore, the mirror plane has to be perpendicular to the **k**-vector. The lengths of the signal and reference arms are then roughly adjusted by measuring the path length with a ruler. In the second step, a multi-mode laser diode of 633 nm wavelength is used to fine tune the path length of the reference arm. For a multi-mode laser diode, the coherence length should be well below 1 mm. In fact, interferometric measurements revealed a coherence length of approximately 400 µm. The beams are then superimposed by adjusting the reference mirror by using a screen which is inserted at different positions in the merged beam. Afterwards, the beam is focused on a charge-coupled device camera connected to small monitor. When both arms have different lengths, the brightness of the spot on the monitor should not change when the beam length of the reference arm is altered, since no interference effects are possible. If the arms lengths are almost equal then a change of the reference arm will result in a clear flickering of the spot on the monitor, due to the small distance of approx. 310 nm between neighboring interference maxima. The mid position between the appearance of this flickering and its disappearance then corresponds to equal length of both arms, also known as white light interference. In the last step, the mirror in the signal arm is replaced by the tip and the interference is maximized with the amplitude signal at the harmonic one is interested in.

However, up to now there has been no proof of principle for the accuracy of the overall concept of the used phase controlled interferometer. For this reason, one of the first tasks was the verification of the idea. This was done with the CO_2-laser,

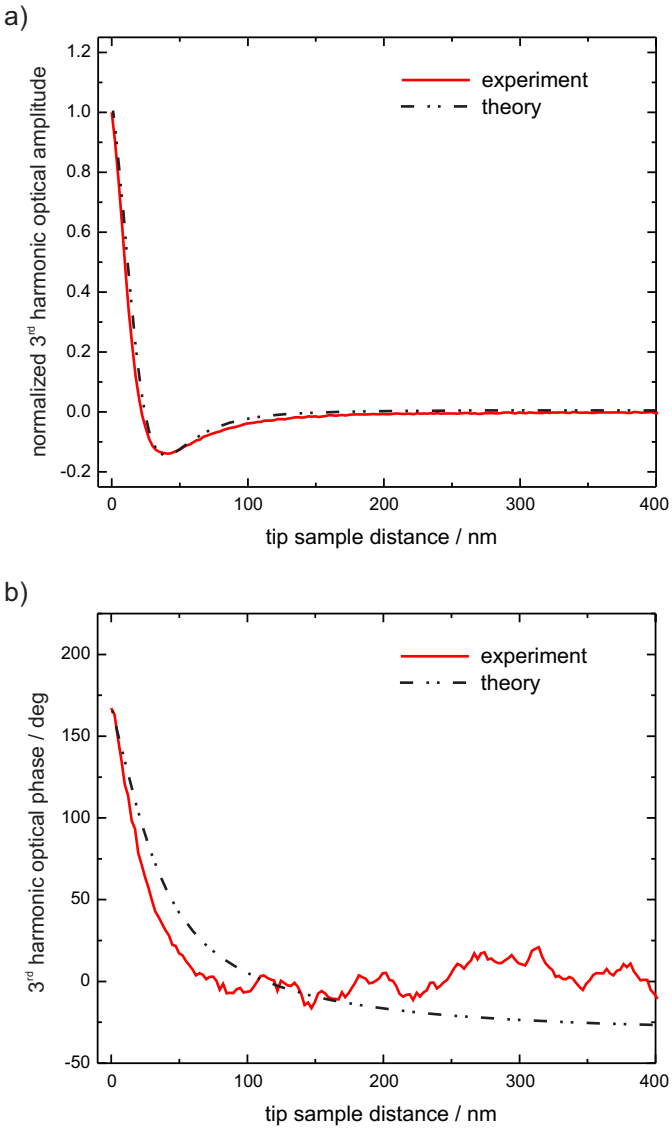

Figure 6.7: *Comparison of the experimental and theoretical behavior of the 3rd harmonic near-field amplitude a) and phase b) for an approach curve on a SiC sample at* 10.6 µm *(p-polarized, background corrected, average over 10 measurements).*

since it provides a beam of high coherence which facilitates the adjustment of the interferometer. Single-crystalline silicon carbide (SiC, 4H polytype) was chosen as test sample, because it exhibits strong phonon resonances around 10.6 µm wavelength [Mut99]. Furthermore, it has already been studied by near-field microscopy numerous times [Oce06, Ren05], and thus, the near-field response of the system is very well known and predictable.

The measurements consisted of multiple approach curves, where the distance between tip and sample was decreased from more than 400 nm to 0 nm, which means contact. During the approach, the amplitude signal and the phase feedback signal were recorded at a certain harmonic of the cantilever oscillation frequency. The input for the phase

controller was derived from a two-step demodulation of the interference signal (see figure 6.3b). The first lock-in amplifier demodulated the detector signal at the n-th harmonic with a time constant of 1 ms and the second lock-in amplifier operated at the mirror oscillation frequency $\omega_{ref} \approx 50$ Hz with a time constant of 30 ms. Parallel to the phase, the amplitude of the near-field was derived from a separate demodulation of the interference signal with a time constant of 50 ms. The approach velocity was 50 nm/s and the tip oscillation amplitude was 60 nm at 150 kHz. The mirror oscillation depth was set to 1.8 µm peak-peak.

In the first run, phase and amplitude were measured at different harmonics, as shown in figure 6.7. The theoretical behavior was derived from the scattering cross-section according to equation (2.28), where the dielectric function of SiC was calculated with the Drude-Lorentz model [Mut99]:

$$\varepsilon_s(\omega) = \varepsilon_\infty + \sum_j \frac{\omega_{j,p}^2}{\omega_{j,TO}^2 - \omega^2 - i\omega\gamma_j} \tag{6.5}$$

$$\omega_{j,p}^2 = \varepsilon_\infty \left(\omega_{j,LO}^2 - \omega_{j,TO}^2\right). \tag{6.6}$$

Here, $\varepsilon_\infty = 6.6$ is the high frequency limit of the dielectric constant and $\omega_{j,p}$ the plasma frequency. $\omega_{j,LO}$ and $\omega_{j,TO}$ are the longitudinal optical and transversal optical phonon frequencies, with $\omega_{1,LO} = 972\,\mathrm{cm}^{-1}$ for the longitudinal optical mode and $\omega_{1,TO} = 796\,\mathrm{cm}^{-1}$ for the transverse optical mode, according to Mutschke *et al.* [Mut99]. Furthermore, $\gamma_j = 3\,\mathrm{cm}^{-1}$ represents the phonon damping. The data were fitted by varying the tip radius. The best fit was obtained for a radius of 150 nm. This is rather high, but no unexpected, since the tip was previously used for other measurements and there was at least one tip crash during this experiment while the reference mirror was adjusted. As visible in the image, a very good agreement could be achieved for the near-field amplitude. Even the local minimum at 40 nm, which is caused by the phonon resonance, could be measured experimentally. Furthermore, a good agreement is achieved for the the phase-signal, although there are some deviations. The difference in the phase signal at distances below 100 nm is attributed to the controller. Because the near-field amplitude is almost zero beforehand, the mirror position for constructive interference is not defined. But as soon as the amplitude reaches a significant level, the controller finds the maximum and moves the mirror to the correct position. However, this requires some time and depends on the controller settings. The shift at 100 nm indicates this reaction time. The differences in the experimental phase signal for large distances can also be explained with the lack of a near-field signal. But apart from this differences, it is clearly visible that the experimental and theoretical data show a relative phase shift of 170° at 0 nm distance with respect to the phase observed outside the near-field. Since the measured phase signals can be explained by theory, these measurements can be interpreted as a proof of principle for this technique.

To further corroborate this approach, phase and amplitude were measured in a second run with different interferometer schemes. The phase controlled interferometer was used at the beginning, while in the second pass a homodyne interferometer was used. For this purpose, the mirror oscillation was stopped and then two measurements were performed at mirror positions corresponding to a phase shift of 90°. From these two

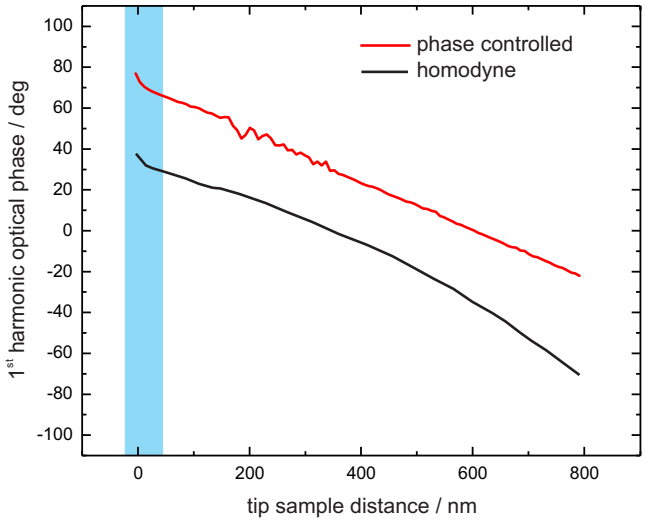

Figure 6.8: *Comparison between different detection schemes for the near-field phase of the 1st harmonic on SiC at* 10.6 µm *(p-polarized, without background correction). The near-field region is highlighted blue.*

measurements, the phase can be calculated from the amplitude measurements (s_{x1}, s_{x2}) at the two mirror positions ($x1$, $x2$) according to [Har92]

$$\frac{s_{x1}}{s_{x2}} = \tan \Delta\phi. \tag{6.7}$$

The result for the first harmonic is shown in figure 6.8. Again a good agreement of the two curves is observable. The offset between the curves can be explained by the mirror position for the maximal interference which was not exactly at 0. Nevertheless both curves show the same relative phase change when approaching the sample. They show the same behavior not only for the far field contribution (linear slope), but also for the near-field (small nonlinear rise near 0 nm). Furthermore, as the homodyne interferometer is the simplest way to perform a phase measurement, the agreement between our phase controlled scheme and the homodyne measurement supports the approach to interpret the output of the phase feedback as equivalent to the shift of the near-field phase.

6.4 Summary

In this chapter the instrumentation for this PhD-thesis was discussed. The home-built atomic force microscope was explained in detail. It is able to measure the topography, the optical near-field and the Kelvin response of the sample at the same time. If necessary the illumination of the sample can be altered as the AFM exhibits a free-standing cantilever. The required optical setup was also discussed. It offers the possibility to use different light sources with minimal alignment effort. Furthermore it includes a setup to measure the near-field interferometrically. Finally it was shown which topographical

and optical resolutions can be achieved with this setup and that the phase controlled interferometer works as expected.

Part III

Experiments on semiconductor materials

7 Boron implanted silicon

The first system that was investigated with the developed setup was a sample of boron implanted silicon. The aim was the determination of the carrier concentration in the implanted region by means of the near-field signal. This specific issue has already been demonstrated by different groups, also on boron implanted silicon. Hence, it can be used to evaluate the built SNOM. Furthermore, its preparation and annealing behavior has already been studied numerous times, so that the final carrier concentration can be predicted from the preparation process. It will be explained in the following chapter which parameters had to be considered for the preparation, as well as their influence on the expected near-field signal. Afterwards, the results of the spectral and interferometric measurements will be presented which were compared to the predictions from the preparation and to the results of other groups.

7.1 Introduction

It was explained in the first part of this thesis that near-field microscopy is sensitive to changes of the dielectric function which are coupled to the scattering cross-section C_{sca} by the surface response function β (see equation (2.28) in chapter 2). A change of the dielectric function should result in an altered near-field response. Hence, it should be possible to exploit this effect when investigating samples of different composition. The easiest design one can think of, is one material (by means of different dielectric functions) next to another. The situation becomes more challenging, when these materials are on top of each other or if one material is embedded in the other. The latter can be found in all kinds of implanted semiconductors, independently from the host material. Thus, in principle it should be possible to distinguish the doped or implanted regions from the undoped or not implanted host material by near-field microscopy.

The correctness of this assumption has been shown by Lahrech *et al.* in the year 1997 [Lah97]. Boron implanted silicon was used to demonstrate the pure dielectric contrast qualitatively. Similar measurements were published by Knoll and Keilmann a few years later [Kno00] and also by Samson *et al.* [Sam06]. In all cases, the presence of additional carriers in the implanted areas altered the index of refraction so that an optical contrast could be measured in the mid-infrared range. Later this idea was extended in the attempt to quantify the number of carriers in the implanted/doped region by means of the optical contrasts.

At this point it is necessary to distinguish between doped and implanted semiconductors. The latter are always created by ion implantation of bulk materials with shallow donor or acceptor ions, which are elements with one valence electron more or less than the matrix. This yields a depth profile of varying concentration of the donors/acceptors.

Furthermore, the implanted bulk has to be thermally annealed, so that the implanted ions are incorporated into the bulk lattice by moving from interstitial to lattice sites. This is also known as electrical activation, because without annealing, the additional charge carriers would not contribute to the bulks conductivity. The term "doped" also refers to ion implanted semiconductors and additionally to semiconductors, where the donor and acceptor elements are added during the growth of the bulk crystal or by diffusion into the bulk. Thus, these elements are incorporated directly into the lattice and no thermal annealing is necessary. This meaning will be used in following chapter.

The first successful experiment to quantify the carrier concentration in doped semiconductors was published by Huber [Hub07, Hub10] on the example of cross-sections of pnp-transistors. Later, Keilmann succeeded in the quantitative contrast measurement on implanted semiconductors [Kei09]. In both examples, the implanted/doped region was situated at the sample surface and extended, in the case of the implanted silicon, approximately 30 nm into the bulk. Recently, the same technique has been successfully applied to indium phosphide nanowires [Sti10].

In all cases, the carrier concentration was extracted from the measurement of the near-field amplitude and phase. The measured data were compared to theoretical predictions according to the dipole-dipole model (see chapter 2), where the carrier concentration is included as fitting parameter via the Drude-Lorentz model for free carriers in semiconductors [Kit06]:

$$\varepsilon_s(\omega, N) = \varepsilon_\infty + \frac{\omega_p^2(N)}{-\omega^2 - i\omega\gamma(N)} \tag{7.1}$$

$$\omega_p^2(N) = \frac{qN}{m^*\epsilon_0}. \tag{7.2}$$

Here, N is the concentration of free carriers, q the electron charge and m^* is the effective mass, which is $0.26m_0$ for Si with m_0 being the free electron rest mass [Spi57]. ε_∞ is the high-frequency limit of the dielectric function, which is 11.9 for silicon. ε_0 is the vacuum permittivity. γ was derived from a numerical simulation that considers the different carrier concentrations [Hum88]. This technique allows the quantification of the carriers by a single measurement at a fixed wavelength. But the wavelength has to match the plasmon resonance of the sample ($\mathrm{Re}(\varepsilon_s) \approx -1$), otherwise almost no contrast in phase or amplitude would be visible. This becomes understandable with the help of figure 7.1. Here the real part of the dielectric function of doped silicon is calculated for different carrier concentrations. It is easy to see that the plasmon resonance depends strongly on the amount of free carriers. If the wavelength is close to this resonance, then one can expect a strong increase in the scattering cross-section (see equation (2.28)) and thus, a strong near-field contrast compared to pure silicon can be measured. With increasing or decreasing wavelength the contrast will drop again, since the absolute value of the surface response function β will converge to zero again. This is illustrated in figure 7.2 for the CO_2-laser wavelength. Here, the optical contrast between doped and undoped silicon is calculated. The reference is silicon with a carrier concentration of 1×10^{15} cm^{-3}. It is obvious that for carrier concentrations below 1×10^{19} cm^{-3} almost no contrast can be obtained and thus a determination

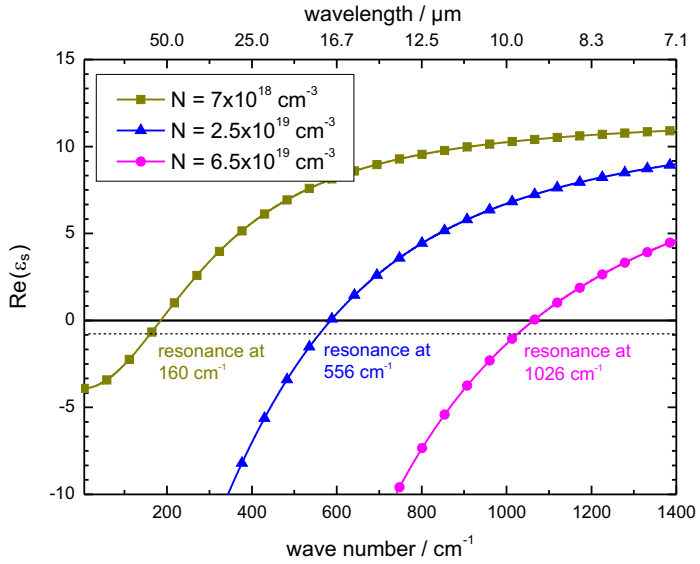

Figure 7.1: *Calculation of the real part of the dielectric function for different carrier concentrations N in silicon plotted versus the wavenumber. The plasmon resonances are denoted to emphasize the dependence on the carrier concentration.*

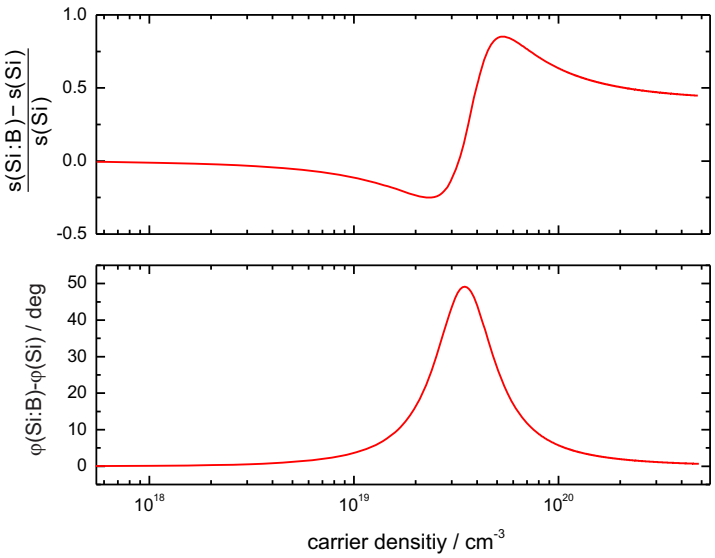

Figure 7.2: *Calculation of the amplitude and phase contrast between doped and undoped silicon for a measurement at* 10.6 µm *(p-polarized) wavelength as a function of the carrier concentration. The reference is undoped silicon with a carrier concentration of* 1×10^{15} cm^{-3}.

of the number of carriers is not possible. The same is true for concentrations above 2×10^{20} cm^{-3}, even though the amplitude contrast is not zero. But it becomes constant the more carriers are present. Only between 1×10^{19} cm^{-3} and 1×10^{20} cm^{-3} a reasonable determination of the concentration is possible. Hence, a closer look at the published measurements will reveal that the measured carrier concentrations are all in this range since those measurements were performed with carbon dioxide lasers around 10.6 µm wavelength. An exception is the measurement from Samson *et al.*. They used a wavelength of 3.22 µm and investigated a sample with a carrier concentration of roughly 5×10^{18} cm^{-3}. However, they did not try to deduce the carrier concentration from their measurements. Furthermore, they only measured the amplitude.

On the other hand, it should be possible to deduce the carrier concentration solely from measuring the optical amplitude contrast at different wavelengths. If one can measure the increase and decrease of the contrast when passing the plasmon resonance, then one can pinpoint the wavelength of this resonance which will only correspond to a certain carrier concentration. But this requires a light source with an emission that is tunable over a few micrometers.

The developed s-SNOM allows the measurement with both concepts - interferometric with phase and amplitude information, as well as wavelength resolved with only the amplitude. Hence, mapping the carriers in semiconductors presents a good benchmark for testing the setup. The obtained results can be compared to existing measurements of other groups and thus a verification of the results is possible. Therefore, it was decided to prepare such a sample by ion beam implantation. Boron was chosen as dopant, since the implantation behavior as well as the annealing/activation behavior of the this element in silicon is well known. The preparation of the sample and the obtained results will be discussed in the following sections.

7.2 Sample preparation

The main objective for the sample preparation was to achieve a carrier concentration around 4×10^{19} cm^{-3}. This would yield a strong amplitude and phase contrast between the implanted and not implanted areas at 10.6 µm wavelength (see figure 7.2). Hence, the interferometric measurement would yield an accurate value for the carrier concentration. Furthermore, in the set of available detectors, the detector for 6 µm to 12 µm is the most sensitive. With this priority, the necessary implantation dose was calculated, for which two parameters had to be known.

The first parameter was the activation A. It defines the amount of implanted ions which are incorporated into the lattice during the annealing in reference to the total amount of implanted ions. An activation of 100 % would mean that all ions are substitutionally built into the lattice. Thus all additional carriers would contribute to the bulk conductivity. Hence, it is necessary to distinguish between the concentration of implanted ions N_{ions} and the concentration of charge carriers N after annealing. They are connected by the activation:

$$N = A \cdot N_{ions} \tag{7.3}$$

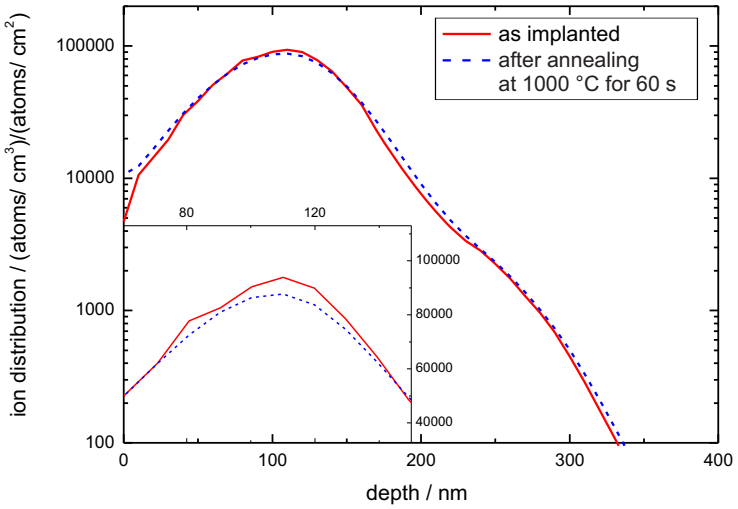

Figure 7.3: *Calculation of the depth dependent ion distribution $c(x)$ for the implantation of boron with* 30 keV *in crystalline (100)-silicon before and after annealing. The inset shows a magnification of the peak.*

The activation strongly depends on the preparation process, especially on the dopant, on the implantation dose, on the annealing temperature and on the annealing time. To obtain the activation one has to perform measurement series, for example, at samples of known ion concentration, while changing time and temperature. As this was not part of this thesis, boron was chosen as dopant, because the annealing behavior in silicon is well known and understood. Hence, the activation could be taken from literature. For example, Solmi *et al.* [Sol91] and Landi *et al.* [Lan88] studied the diffusion behavior of boron for different doses, temperatures and annealing times when using rapid thermal annealing (RTA). Both groups obtained the result that an activation of 100 % can be obtained for a dose of 5×10^{14} cm^{-2} at 1000 °C and 10 s (group of Solmi) and 60 s (group of Landi). Wieser and Panknin [Wie84] deduced the same activation for a dose between 1×10^{14} cm^{-2} and 5×10^{14} cm^{-2}, when annealed by a flash lamp.

The second parameter was the conversion factor c that is necessary to calculate the ion concentration N_{ions} in units of [cm^{-3}] from the implantation dose D in units of [cm^{-2}]. This factor is depth dependent, since it is connected to the depth which the ions penetrate into the bulk during implantation. Hence, it represents the implantation profile of the ions at a certain implantation energy, also known as ion distribution. The ion concentration can then be calculated using:

$$N_{ions}(x) = c(x) \cdot D, \tag{7.4}$$

where x is the depth, measured from the sample surface. The ion distribution, and with it the conversion factor, can be obtained by simulating the penetration depth of the boron ions in the crystalline (100)-silicon bulk. For this, Crystal-Trim [Pos94] has been used and the result is depicted in figure 7.3. The plot shows an inhomogeneous ion distribution with a peak at approximately 100 nm below the sample surface, with

Substrate	n-type (100)-silicon
Specific resistivity	1 . . . 10 Ωcm
Dopant	boron
Implantation energy	30 keV
Implantation dose	6.8×10^{14} cm^{-2}
Implantation	at room temperature, whole surface, ion beam tilted 7° against surface normal
RTA	60 s at 1000 °C

Table 7.1: *Details of the boron implantion.*

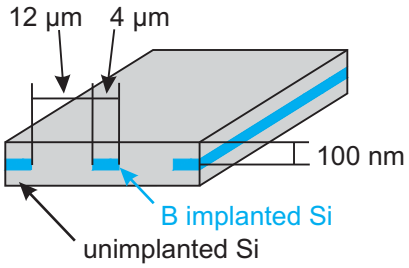

Figure 7.4: *Sketch of the intended sample layout.*

a conversion factor of approximately 100, 000 cm^{-3}/cm^{-2}. This distribution will later influence the optical contrast, as the tip probes different depths at the same time. Based on figure 7.3, one could assume that a dose of 4×10^{14} cm^{-2} is enough to achieve the primary goal of a carrier concentration of 4×10^{19} cm^{-3}, as a complete activation of the ions can be expected from the literature. However, one has to take into account that the boron ions at the peak diffuse to regions of lower concentrations during annealing. This results in a drop of the conversion factor. Hence, the achieved carrier concentration would be lower than the intended concentration. The calculation shows a drop of roughly 10 % in the conversion factor (see inset in figure 7.3), while the peak profile is almost unaffected. On the other hand, Solmi *et al.* [Sol91] observed a drop of 50 % in the peak concentrations in combination with a slight broadening of the profile. A similar result was observed by Ryssel *et al.* [Rys80] for higher doses annealed at 1000 °C. Hence, it was decided to set the dose for the actual implantation to 6.8×10^{14} cm^{-2} to account for the experimental diffusion, but slightly lower to consider the calculations. The thermal activation of the carriers was performed by rapid thermal annealing at 1000 °C for 60 s in dry nitrogen atmosphere, to avoid surface oxidation of the wafer. An overview of the implantation and annealing parameters is given in table 7.1.

After the calculation of the necessary implantation dose, an implantation pattern had to be developed which would define the implanted areas on the substrate wafer by shielding parts of the wafer from implantation. It was decided to use alternating parallel stripes of implanted and not implanted regions. The boron implanted regions should be 4 µm wide, while the not implanted silicon bulk between the implanted stripes should be 10 µm wide. A sketch of the layout is depicted in figure 7.4. This

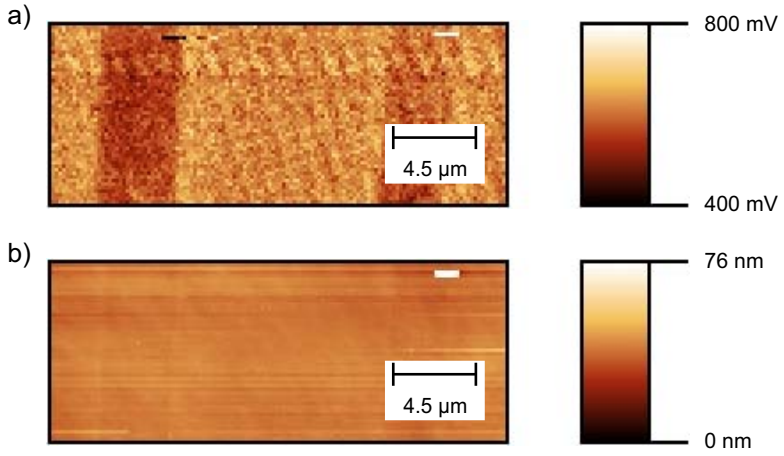

Figure 7.5: *Sample characterization after preparation. a) Kelvin signal and b) topography that were measured at the same time. The ripples in figure a) are induced by electronic noise. The missing parallelism in the figures is an artifact of the sample scanner, whose drift is strongly non-linear.*

would simplify the following near-field measurements, because an easier identification of the different areas would be possible. Furthermore, the necessary lithography masks already existed, which helped saving time.

The sample was then prepared by first cleaning with sulfuric acid. Afterwards the implantation mask of 220 nm silicon dioxide was prepared on the sample surface by dry oxidation, patterning by photolithography and subsequent wet etching. The next step was the implantation, followed by annealing and removal of the mask.

The first measurements after the preparation were the topography and Kelvin response. It was expected that especially the Kelvin signal would give a clear contrast due to the strong difference in the concentration of the free carriers [Bau09, ZT07]. In contrast, the topography should be flat, without topographical indications for the implanted areas, since these could lead to topography induced artifacts in the near-field signal. The result is shown in figure 7.5. Here, topography and Kelvin signal were measured at the same time. But while the Kelvin image (figure 7.5a) shows a clear contrast between two obviously different regions, almost no contrast is visible in the topography (figure 7.5b). The dark stripes in the Kelvin image can be attributed to the boron implanted silicon, since they have a width of 4 µm, which was the intended dimension for the implanted stripes. However, when having a closer look at the topography image, then a very weak contrast can be observed. This is especially true when compared to the Kelvin image, as the human eye notices the contrast more easily when it knows where to look for it. So there is a contrast in the topography, but it is below 1 nm. The implanted regions appear slightly darker than the surrounding silicon, which is an indication that they are deeper than the not implanted silicon. It is a result of sputtering of the silicon by the boron ions during the implantation process. At last, the homogeneous coloring of the topography image indicates that the sample is very flat, as expected.

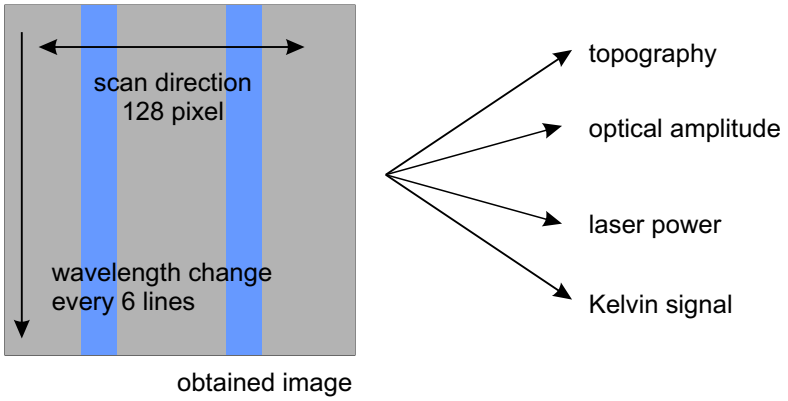

Figure 7.6: *Scheme of the measuring concept.*

7.3 Spectral measurements in the mid infrared

The spectral, non-interferometric near-field measurements between 10 µm and 16 µm were performed with the free-electron laser U27. But as the tunability of the source is limited to roughly 15 % during a measurement run, the experiments were split into parts covering 2 µm each.

The concept of the measurements is depicted in figure 7.6. Scans were taken across at least one stripe of implanted silicon, while the scanned line was repeated after it was finished. This operation mode ensured that the investigated sample area stayed the same during the measurement. After finishing the whole measurement this was checked again. Every 6 lines, the incident wavelength was changed by approximately 100 nm. A line had 128 pixels with a read out of all input channels at every pixel. The scan velocity was set to 6 s/line, which allowed an integration time of 50 ms for the lock-in amplifiers that were used to measure the 2^{nd} and 3^{rd} harmonic of the optical near-field signal. Besides the optical information, the topography, the laser power and the Kelvin signal were measured at the same time. The tip oscillation amplitude was set to 60 nm and the oscillation frequency was roughly 150 kHz. In every measurement 21 wavelength steps were used, yielding 126 lines per image.

A typical result of such a measurement is depicted in figure 7.7, where the four measured channels are shown for a spectral range from 13.18 µm to 10.6 µm. Figure 7.7a shows the topography channel, where some vertical lines are visible. These stripes originate from topographical events during the scan of the sample. Because the line is scanned over and over again, the topography does not change and hence, the image consists in principle of one line only. But it is obvious that there were some changes during the scan, as these vertical stripes are not exactly vertical. This is a result of the drift of the scanner. Furthermore, the black horizontal lines in the figure indicate positions, where the tip lost contact to the sample surface. This can occur when the feedback loop is disturbed by a sudden incident. To prevent the tip from crashing into the surface, the controller retracts the sample which yields these black lines. The boron implanted region is hard to recognize. In figure 7.7b this becomes easier, since this image shows the Kelvin signal. The implanted region appears darker than the

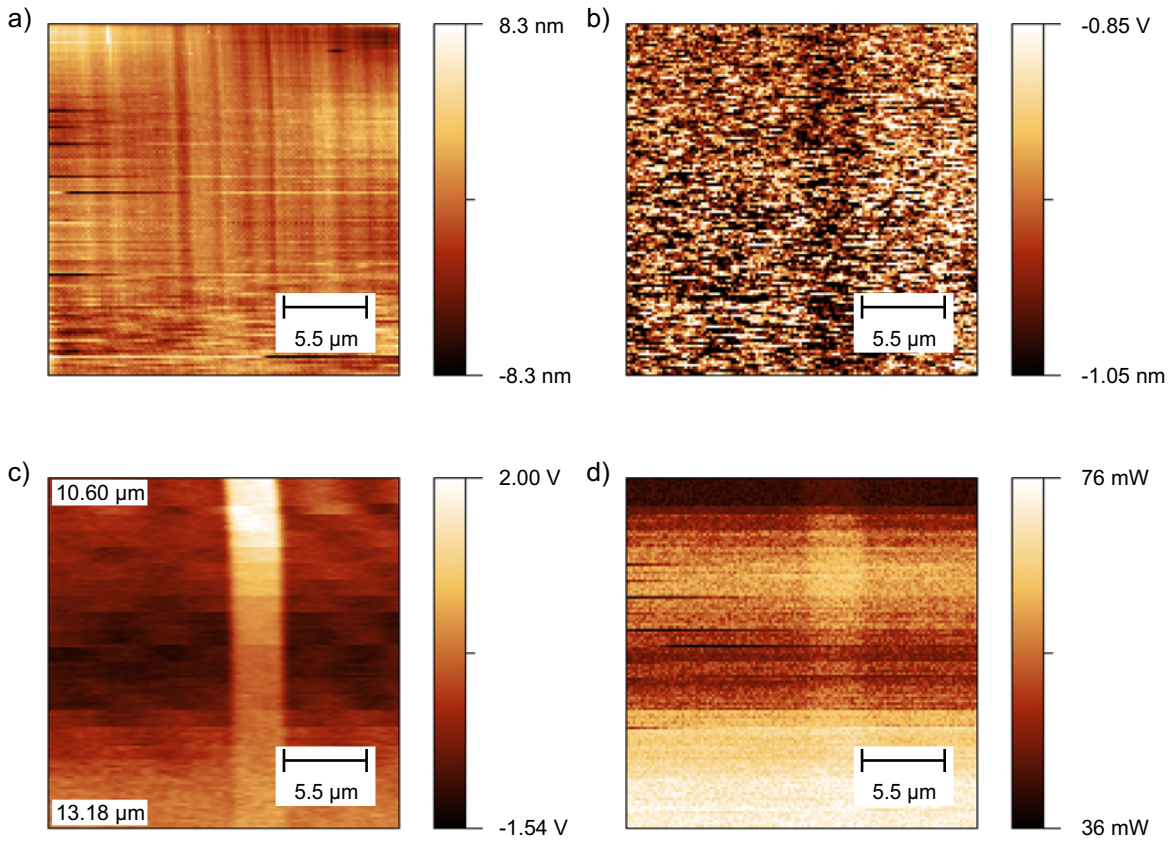

Figure 7.7: *Result of the spectral measurement between* 13.18 µm *and* 10.6 µm *(p-polarized, raw data). a) Topography. b) Kelvin signal. c) X-output of the* 3^{rd} *harmonic. d) Laser power.*

surrounding substrate. Apparently, only one stripe of boron implanted silicon was in the scan range. The optical signal is shown in figure 7.7c, where the X-output of the lock-in amplifier is depicted that was set to 3^{rd} harmonic. Here, the boron implanted region is easy to identify. The top of this image represents 13.18 µm wavelength. The wavelength was changed subsequently to 10.6 µm at the bottom of the image. The stepwise change of the wavelength is recognizable by the mismatch between consecutive lines. That becomes clearer when figures 7.7c and 7.7d are compared. The latter shows the laser power at the specific wavelength. Each time the wavelength was changed, there was a small change in the laser power. This can be seen in 7.7d. Furthermore, the figure shows an artifact, as the boron implanted stripe is visible in the laser power, too. This is however not possible, since the power is measured before the beam is focused on the tip. The stripe in the this figure is thus a result of an electrical cross-talk between the recording channels.

Each measurement produced such a set of data. In addition to these four channels, the wavelength dependent splitting behavior of the mylar beam splitter was measured in each run. This facilitates the comparison of the data when the settings for the sensitivity of the lock-in amplifiers and the laser power are taken into account. For this reason, the data were normalized to the laser power and scaled to a common sensitivity.

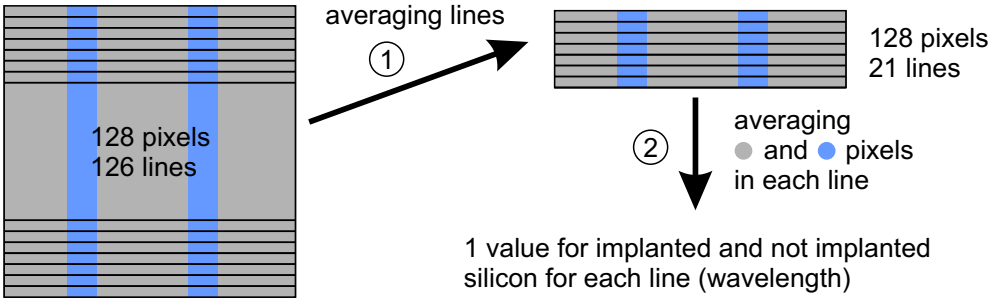

Figure 7.8: *Data processing steps to obtain the wavelength dependent signal for the implanted silicon and the pure silicon.*

Afterwards, the wavelength dependence of the signals of the boron implanted silicon and the not implanted silicon were extracted from the data sets. This was done by averaging the signal of the six lines that belong to a certain wavelength in the first step. In the next step, all pixels that belong to the specific area were averaged. This procedure (schematically depicted in figure 7.8) yielded two values for each wavelength step - $V_{implanted}$ for the implanted region and V_{pure} for the not implanted region.

When having a closer look at figure 7.7c, it can be seen that there are also negative values for the optical signal. So it cannot be a real amplitude, since an amplitude is always positive. What is depicted in that figure is the X-channel of the used lock-in amplifier. This is a result of the adjustment procedure that was used to obtain a near-field signal. In order to achieve a good alignment, a sample was necessary that yielded a strong near-field response. As it was not known, whether the boron implanted silicon will show a clear near-field signal, a sample of silicon carbide was chosen for the alignment. As a polar material, SiC yields a very strong resonance around 10.6 µm (see section 6.3) that can be used to align the setup. After the maximum in the near-field signal was achieved on SiC, the lock-in phase was set to zero. This phase is the phase difference between the oscillating input signal of the lock-in amplifier and the reference oscillation that is fed into the lock-in. If the sample is then replaced, a shift of this lock-in phase can occur. For the correct phase-sensitive measurement it is then better to use the X-output, which can be positive and negative, instead of the amplitude output, which is always positive.

The obtained values $V_{implanted}$ and V_{pure} for the different sample areas were then used to calculate the signal difference, which is similar to the scattering contrast (see equation (2.52)), except that it is not normalized to one of the values. To account for the offset issues of the measurements, only the absolute value of the difference was analyzed. Hence, the experimental contrast was defined as

$$K = |V_{implanted} - V_{pure}| \,. \tag{7.5}$$

As the total signal was often close to zero, the normalization would lead to very strong scattering of the contrast due to the division by small values. Hence, the normalization was skipped, but that aggravated the further interpretation immensely which will be explained later. The experimental contrast K will be referred as (optical) near-field difference and is depicted for the 3^{rd} harmonic in figure 7.9. Since the plot contains

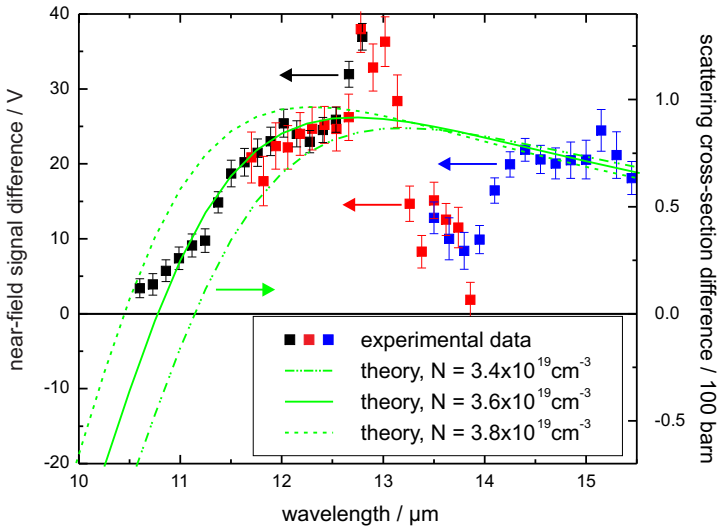

Figure 7.9: *Plot of the experimental contrast and the theoretical calculated cross-section difference as function of the wavelength (p-polarized) for the 3^{rd} harmonic. The colored dots (black, red and blue) represent experimental data, where the color indicate the different measurement runs. The green lines are calculated from theory.*

a lot of information, the different issues will be discussed step by step in the next paragraphs.

First, the plot shows a series of colored dots. All dots refer to measured data of the near-field signal at the 3^{rd} harmonic, like they were obtained with the previously described procedure. The color symbolizes which measurement run the data point belongs to. As already mentioned, the spectral measurements spanned a wavelength range of roughly 10 µm to 16 µm. This range was split into three runs, each covering 2 µm. The three colors represent these three measurement runs. Furthermore, it is visible that the runs overlap slightly and that the experimental data were reproducible in the overlap region.

The plot shows a strong increase of the experimental signal difference for the measurement from 10.5 µm to 12 µm. This increase seems to saturate as the slope decreases towards 12.5 µm. Above this point a strong rise of the difference can be observed, followed by a strong drop. The drop of the signal between 13.3 µm and 14 µm can be attributed to the used mylar beam splitter. It exhibits an absorption line around 13.9 µm that leads to a strong decrease of transmission and reflection (see figure 7.10). The minima of transmission and reflection are slightly shifted against each other, which can be explained with Drude-Lorentz-model. Hence, the affected wavelength range for the near-field measurements is extended around the center of the absorption line, because the beam is reflected at the mylar foil and transmitted later. However, the peak around 12.9 µm cannot be attributed to the beam splitter. A possible explanation could be the phonon resonance of native silicon dioxide at 800 cm^{-1} [Sha01]. This would correspond to 12.5 µm which would be slightly too low. But there have been also slightly lower values for this resonance reported in the literature, for example 796 cm^{-1} (12.6 µm) [Pal98] or 780 cm^{-1} (12.8 µm) [Ahr95]. However, an increase due to the SiO_2 reso-

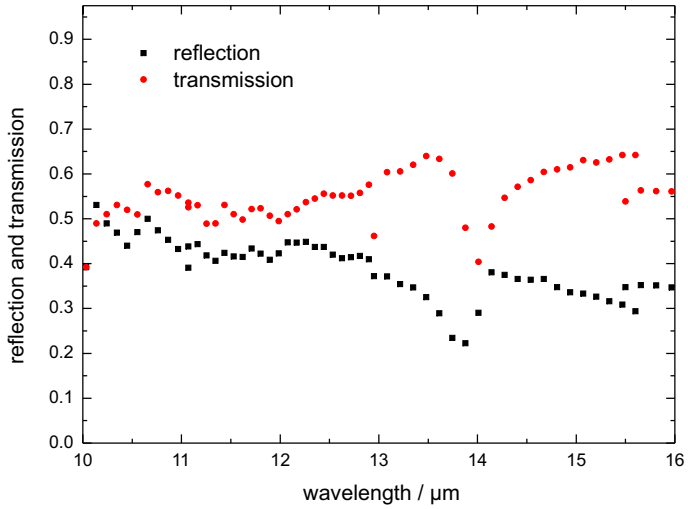

Figure 7.10: *Wavelength dependence of the transmission and the reflection of the used mylar beam splitter.*

nance would only be possible, if there are differences in the thickness of the SiO_2-layer on top of the implanted region and the pure silicon. Otherwise, the resonance would result in an equal increase of the optical near-field signal on both materials. Hence, no peak would be visible. A closer examination of the signals revealed that the signal on top of the boron implanted silicon changed disproportionately between 12.5 µm and 13 µm. This would imply that the native SiO_2-layer is thicker than on the pure silicon. But that would by only possible, if the growth velocity and the resulting layer thickness on the implanted silicon is higher, since the exposure time was the same. Literature research revealed that this problem has been already discussed numerous times [Rai75, Rit65], with the result that the growth velocity increases strongly for highly doped silicon. Wolkenberg showed a two times faster growth on top of highly p-doped silicon than on pure silicon [Wol83]. Later, Takeuchi and Inaba showed a two times higher growth velocity on top of p-doped silicon than on n-doped silicon [Tak91]. Hence, it is reasonable to account the SiO_2 resonance for this peak.

Besides the experimental data, figure 7.9 shows three green lines of different style. Those lines were obtained by calculating the difference of the scattering cross-sections of boron implanted silicon and pure silicon. The calculation were performed by using equations (2.40) and (2.42) of the first part of this thesis. The model contains a set of parameters, which have to be known to obtain the correct values. These parameters are the tip oscillation amplitude A, the oscillation frequency Ω, the tip radius r and the carrier concentration N. The first two were taken from the experiment, as they had to be set before the actual measurement was performed. The third parameter, the tip radius, is much more difficult to measure. But it acts as a scaling factor only, without influence on the wavelength behavior. Nevertheless it had to be within reasonable dimensions. A common assumption in literature is 20 nm to 30 nm, which would imply very sharp tips. As the tip condition changes during an experiment and tip crashes can not be excluded, it was assumed for the calculations that the tip radii

are bigger than those 30 nm. Hence, this parameter was set to 100 nm which is also in agreement with the results described in the alignment section (see section 6.3). The last parameter was the carrier concentration, which should be deduced by comparing the theoretical results with the experimental data. So the model was fitted to the experimental data by modifying the concentration of the free carriers, while keeping the other parameters fixed.

During the fitting process, the earlier introduced simplifications for the experimental contrast K aggravated the comparison of theory and experiment strongly. The experimental contrast lacked a reference which one could refer to. Hence, it still contained the measured unit, in this case volt. In contrast, the theoretical data were obtained in units of the scattering cross-section. That is usually given in barn (10^{-24} cm^2). So in principle both quantities were not comparable, as a conversion factor between both units could not be defined. To be able to compare fit and experiment, four criteria were defined which had to be satisfied after scaling of the plot axis. The first issue was the wavelength, where the theoretical cross-section difference vanishes. Even without normalization, this point has to match the experimental data. In fact, this is not influenced by the scaling of the ordinate. The next point was the slope of the fit in respect to the experimental increase of the signal between 11 μm and 12 μm. This also applied for the wavelength range from 14.4 μm to 15.5 nm, which was the third criterion. The last point was the overall deviation from the experimental data.

The best agreement between the experimental and theoretical data was obtained for a carrier concentration $N = 3.6 \times 10^{19}$ cm^{-3}. The error could be estimated by the range for N in which the postulated criteria were still fulfilled. It is approximately 0.2×10^{19} cm^{-3} which would correspond to a relative error of 6 %. This is indicated by the two additional green lines for the carrier densities of $N = 3.4 \times 10^{19}$ cm^{-3} and $N = 3.8 \times 10^{19}$ cm^{-3}. Furthermore, the calculated data showed that the peak around 12.9 μm as well as the signal drop between 13.3 μm and 14 μm are not induced by the carriers. This result fit well to the expectation from the preparation procedure, which gave an estimated carrier concentration between 2×10^{19} cm^{-3} and 4×10^{19} cm^{-3}.

Due to the simplifications and difficulties during the fitting step, it was intended to cross check the result by a second measurement, which applied a different technique. This would yield an independent result for the carrier concentration. Thus, it was decided to use an interferometric measurement, since the main criterion for the carrier concentration would be the phase contrast. This would render the simplifications unnecessary.

7.4 Interferometric measurements at 10.6 μm

The interferometric measurement were similar to the experiments of Huber and Keilmann [Hub07, Kei09]. Only the expected carrier concentration differed. Hence, the theory that has been used by those groups was used as a reference for the analysis of the measured data.

The experiments were performed using the table-top CO_2 laser which emits at 10.6 μm. The other experimental parameters like the applied laser power, the tip oscil-

lation amplitude or the scan velocity were set to the same values as in the spectral measurements. This allowed a better comparison of the obtained data. Furthermore, the scanned line was not repeated over and over again. Instead a normal two-dimensional image was recorded. In addition to the four previously recorded channels, the optical phase was measured as the fifth input channel. Thus, optical amplitude and phase were available to calculate the carrier concentrations afterwards.

Results of these measurements are shown in figure 7.11. It shows the obtained near-field amplitude (sub-figures a and c) and phase (sub-figures b and d) for two different regions. The implanted stripes are easy to recognize in all sub-figures. But figures 7.11a and 7.11c do not only show the amplitude contrast between implanted and pure silicon. They also show a repetition of dark and bright stripes that are running from the upper left to the lower right corner which is perpendicular to the **k**-vector of the incident beam. These stripes were not visible during the spectral measurement, so they had to be connected to the properties of the used carbon dioxide laser. The extracted line profile (figure 7.12a) reveals that the maxima along the profile had a distance of 5.4 µm which is half the used wavelength. As the scattered light is detected in the back-scattered direction, the path counts twice, so that this corresponds to 10.8 µm. As these stripes were missing in the FEL experiments, they were attributed to an interference effect. This seemed to be plausible, as the coherence length of the carbon dioxide laser is much longer than the coherence length of the FEL. Furthermore, a closer look at 7.11b shows that these stripes also occurred in the optical phase, which corroborates the assumption of an interference effect. The figure displays the boron implanted region as bright stripes, even though it is very noisy.

Figure 7.11d also shows the optical phase, but this time, the stripe appears dark. Between both measurements, the adjustment of the interferometer was optimized, so that the latter figure is less noisy. But the phase of the reference beam has also changed by 180°, so that the phase contrast is inverted. To avoid difficulties in the correct assignment of the sign of the phase, only the absolute value of the phase difference between implanted and pure silicon was later used to calculate the carrier concentration. The obtained experimental phase shift is depicted in figure 7.12b, where the line profile from figure 7.11d is plotted. The shift is 50° with an error of 10°. In contrast, the presence of the interferences pattern in the optical amplitude aggravated the estimation of the amplitude contrast. Hence, only a range could be extracted from the plot which was approximately 20 % to 50 %, calculated according to equation (2.52). The previously used skipping of the normalization of the amplitude contrast could be avoided, since the signal was more stable and not close to zero. In the next step, the values for the amplitude contrast and the phase contrast were compared to the calculations. Both were calculated with the previously used model for the dielectric function (see equation (7.1)). The results are depicted in figure 7.13. It shows the characteristics of the amplitude and phase contrast in dependence on the concentration of free carriers. The experimental data are highlighted as green boxes. For the amplitude contrast, they spread from 20 % to 50 %, while the phase contrast begins at 40°. Furthermore, the vertical dotted lines indicate which carrier concentration would correspond to these data. If only the phase shift is considered for the estimation of the concentration, then

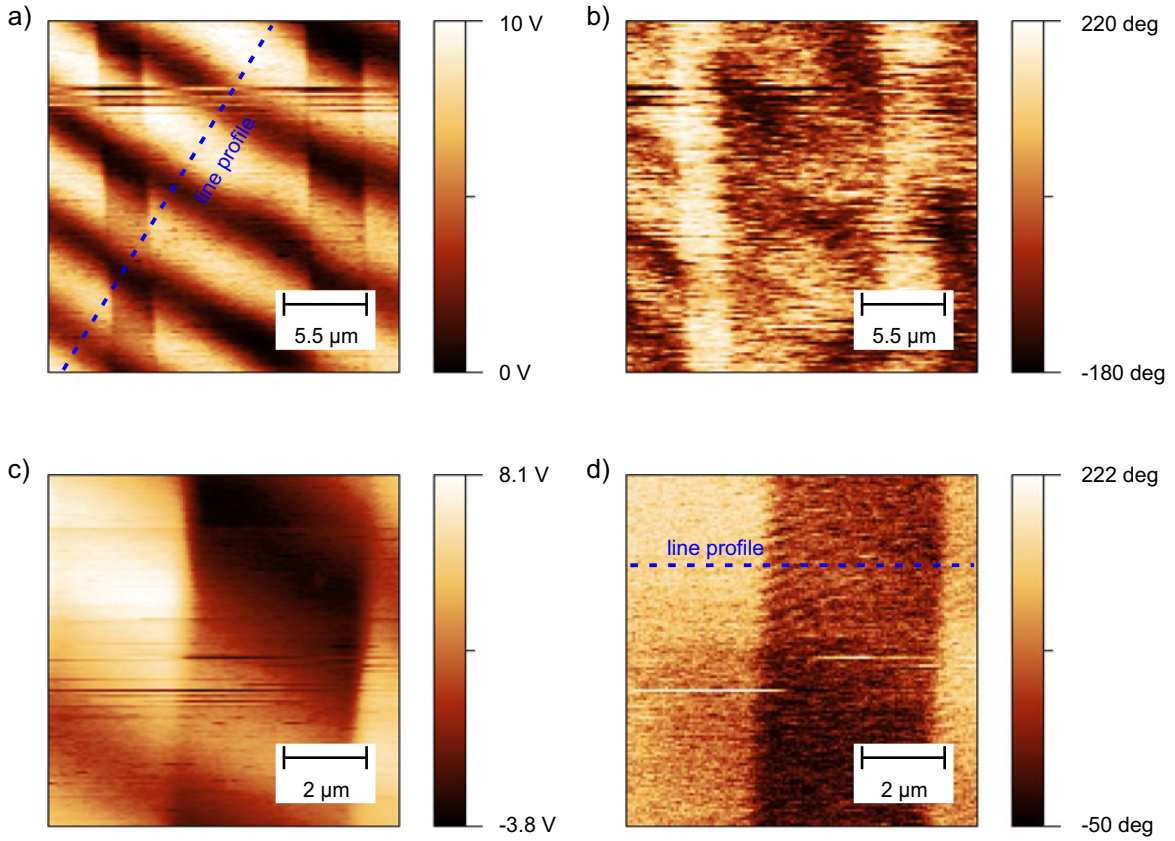

Figure 7.11: *Amplitude and phase measured for the 3rd harmonic at 10.6 µm (p-polarized). a) Optical amplitude and b) optical phase of a 25 × 25 µm² area. c) Amplitude and d) phase of a 7.5 × 7.5 µm² area after signal optimization.*

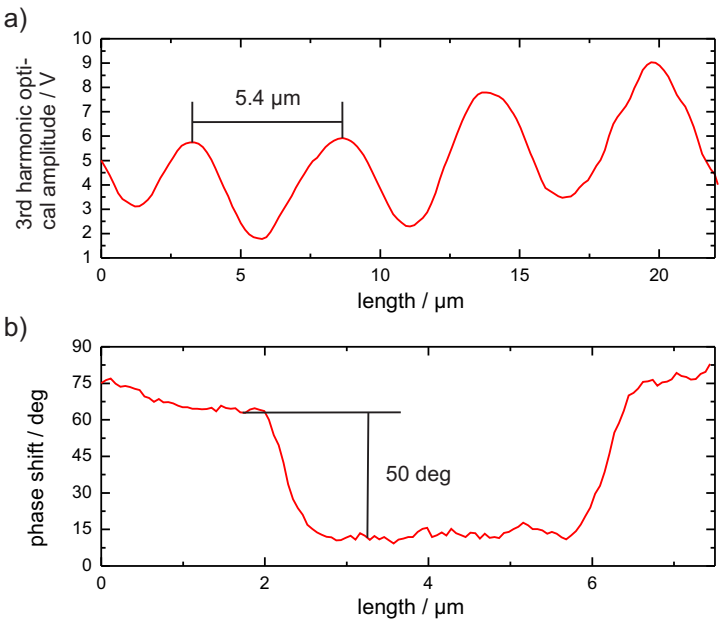

Figure 7.12: *Line profiles extracted from a) figure 7.11a and b) figure 7.11d.*

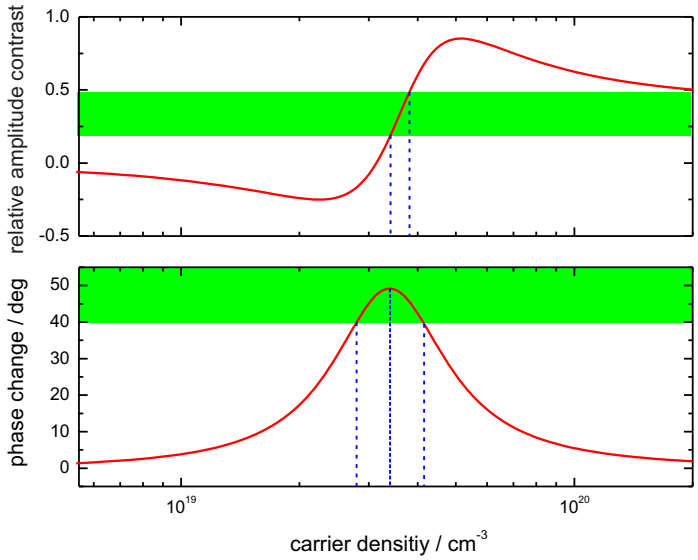

Figure 7.13: *Experimental and calculated data for the amplitude contrast and phase contrast for the 3rd harmonic. The experimental results are highlighted green, whereas the curves represent the theoretical values.*

it would range from $N = 2.8 \times 10^{19}$ cm^{-3} to $N = 4.2 \times 10^{19}$ cm^{-3} due to the significant experimental error. But this would already cover the results from the spectral measurement. If the measured amplitude contrast is additionally taken into account, then this range reduces to 3.5×10^{19} cm^{-3} to 3.8×10^{19} cm^{-3} which is then in very good agreement to the previous results. It is also in agreement with the results from Huber *et al.* [Hub07], who deduced a carrier concentration of 3.5×10^{19} cm^{-3} for a phase shift of 43°. Hence, it is estimated that the carrier concentration in the boron implanted silion is as high as $(3.5 \pm 0.5) \times 10^{19}$ cm^{-3}. The relative error is roughly 15 % which is slightly larger than the error in the spectral measurements.

7.5 Summary

The chapter presented the results obtained on a sample of boron implanted silicon. It was demonstrated with two different measurement techniques that the carrier concentration can be deduced by measuring the optical near-field response. By measuring the wavelength dependence of the near-field signal, it was possible to estimate the concentration even without knowledge of the near-field phase. On the other hand, by measuring amplitude and phase interferometrically, it was possible to verify the obtained results. Both variants yielded a concentration of the free carriers in the implanted regions that is in good agreement with the predictions from the preparation process and with the results of other groups. The results also showed that the applied model is well suited, although it assumes a laterally and vertically uniform carrier concentration, whereof only the former is possible during ion implantation.

It can be seen from the results that the built scattering-type near-field infrared mi-

croscope can be compared to the setups of other groups. Furthermore, the combination with the free-electron laser provides sufficient tunability for quantitative investigations of semiconductors in the mid-infrared.

The main content of this chapter has been published in Optics Express [Jac10].

Expectations from preparation	$< 4 \times 10^{19}$ cm^{-3}
Spectral measurement	$(3.6 \pm 0.2) \times 10^{19}$ cm^{-3}
Interferometric measurement	$(3.5 \pm 0.5) \times 10^{19}$ cm^{-3}

Table 7.2: *Overview of the results on boron implanted silicon.*

8 Indium arsenide quantum dots

In the next chapter the near-field measurements on indium arsenide quantum dots will be discussed. For this purpose, the structure of a quantum dot is briefly introduced, as well as its characteristic properties and common preparation techniques. Afterwards the investigated sample will be discussed in detail. The specific preparation is explained, followed by the characterization of the sample by AFM-measurements and photoluminescence measurements. The major part will be the discussion of the near-field measurements on that sample in the wavelength range of 9.5 µm *to* 11.5 µm *and* 13.5 µm *to* 16.5 µm.

8.1 Introduction

The previous chapter showed the near-field contrasts for a sample consisting of one material whose dielectric function was partially altered by implantation. Another possibility to obtain a material contrast is the combination of different materials, like gold on a glass substrate. Far more interesting is the combination of different semiconducting materials, for example indium arsenide (InAs) and gallium arsenide (GaAs). A very special combination of both materials is the InAs quantum dot in a GaAs matrix.

Quantum dots were discovered at the beginning of the 1980s by the Russian scientists Ekimov and Onushchenko [Eki81]. They studied the absorption behavior of small copper chloride crystals that were grown in a transparent dielectric matrix. During these experiments they observed a shift of the absorption lines when the size of the crystals was changed between a few angstroms and hundreds of angstroms. This represented the first experimental evidence for a quantum size effect and with it the first detection of quantum dots. The term "quantum dot" was later introduced by Reed [Ree86, Ree88]. It refers to the quantization of the electron's free motion due to the almost dot-like dimension. This is schematically illustrated in figure 8.1, where it is shown how the degree of freedom of the electron motion decreases when the dimension of the structures is reduced as well. Starting from a bulk where the electron motion is not confined, it is possible to trap an electron by confining it in all three space dimensions. By introducing a material of smaller band gap than the bulk in a sandwich-like structure, the motion can be restricted to a thin layer. This is is known as quantum well. It is called a quantum wire after decreasing the width of the structure while keeping its length. The electron motion is then confined by two dimensions, so that only one degree of freedom remains. By reducing also the length, the electron is trapped without any degree of freedom for traveling. This case is called a quantum dot. Typically, the size of such a structure is between 10 nm and 100 nm, which is in the range of the de Broglie-wavelength of an electron at room temperature (roughly 28 nm in InAs).

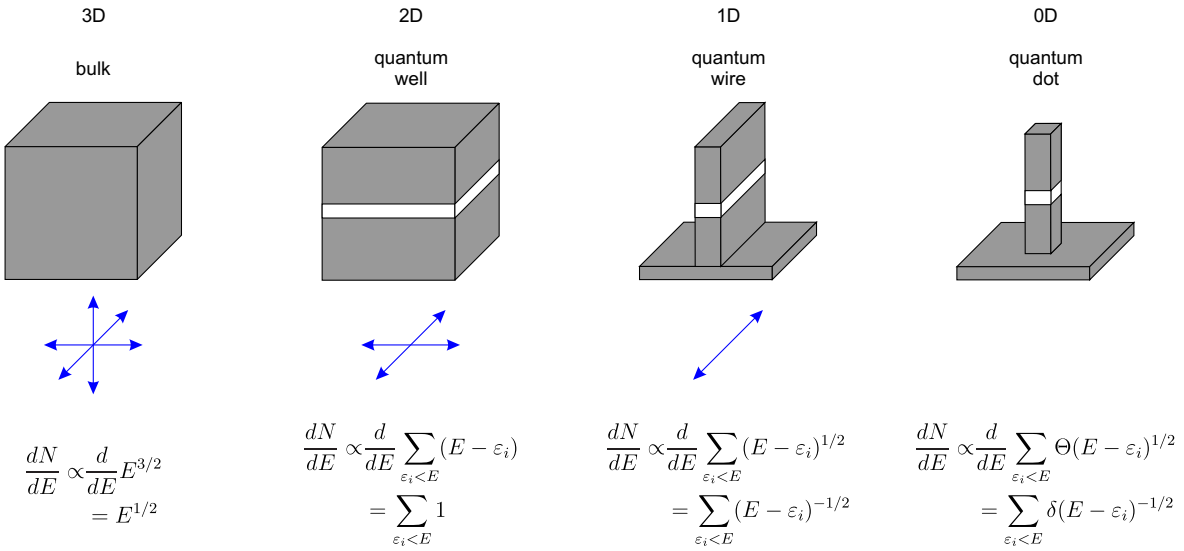

Figure 8.1: *Schematical illustration of the quantization of the electron motion (blue arrows) when the dimensions of the structure are decreased from three to zero. The corresponding density of states $\frac{dN}{dE}$ is also given. E is the energy, and ε_i the energy of the state i. Θ is the Heaviside step function, while δ is the Dirac function.*

With each step in confinement, the quantization of the electron energy increases by one dimension. This can be derived from the density of states $\frac{dN}{dE}$ which is defined as the number of states per energy per unit volume of the real space [Har95]. In $\mathbf{k}$-space, the number of states is equal to the volume of the n-dimensional "sphere" of radius $\mathbf{k}$. For the bulk this corresponds to a sphere, for the quantum well it is a circle, for a quantum wire it is a line and for a quantum dot it is a circle of radius $\mathbf{k} = 0$. Hence, the density of states for a bulk is proportional to the square root of the energy, while it is a step function for the quantum well. The wire exhibits a density of states which is equivalent to the reciprocal square root of the energy and for a dot it has the shape of the Dirac-function δ. Especially at low temperatures the latter becomes important, since the energy of phonons is not high enough to excite electrons. Hence, the strong quantization of the energy determines the electronic properties of the dots [Jac98].

Energy levels and optical transitions

The quantization of the energy is equivalent to a separation of the electronic states. While these states overlap in the bulk material, they are separated by energy gaps in a dot. Hence, it is not unusual that quantum dots are often called "artificial atoms". The energetic position of these states or levels can be calculated analytically in some cases, as it was done by Fock [Foc28] and Darwin [Dar30]. As they were the first who calculated these states, the states are known as Fock-Darwin energy levels. By assuming a confinement of the electrons by a two-dimensional parabolic well, they

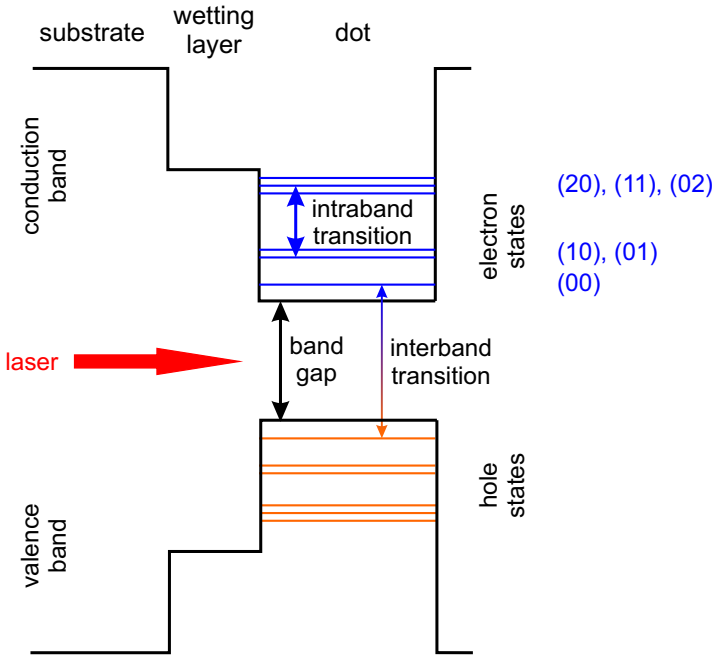

Figure 8.2: *Schematic illustration of the energetic situation in a quantum dot. The quantum numbers on the right label the different electronic states.*

derived for the energy states without magnetic fields

$$\varepsilon(n_x n_y) = \hbar\omega_0 \left(n_x + \frac{1}{2}\right) + \hbar\omega_0 \left(n_y + \frac{1}{2}\right). \tag{8.1}$$

Here, $n_{x,y} = 0, 1, 2, \ldots$ are the principal quantum numbers, which label the energy state, $\hbar = \frac{h}{2\pi}$ is the reduced Planck constant and ω_0 is the eigenfrequency of the oscillator. Since the confinement in the z-direction is much stronger than in the x- and y-direction, this component is separated off. The state with the lowest energy is the ground state, which is labeled as (00) or s-state. The next state is (10) or (01), which is also known as p-state. Above this state is the d-level with the labels (20), (11) or (02).

More interesting than the positions of the energy levels are transitions between them, since in near-field experiments electrons in the dots may be excited to higher levels at an incident wavelength equivalent to the transition energy. It can be shown that such transitions are allowed but follow certain selection rules [Jac98]. For InAs quantum dots it was derived that transitions are allowed when

$$|\Delta n_x| = 1 \text{ and } |\Delta n_y| = 0 \tag{8.2}$$

and vice versa for s-polarized incident fields and

$$|\Delta n_x| = 0 \text{ and } |\Delta n_y| = 0 \tag{8.3}$$

with a change of the energy level due to the z-confinement

for p-polarized incident fields [Vuk06]. Hence, only optical transitions between neighboring levels are allowed. As the participating electron levels are all situated in the

conduction band of the semiconductor, these transitions are called *intraband* or intersublevel transitions. Transitions between valence and conduction band are called *interband* transitions (see figure 8.2) which obey different selection rules. Such transition will occur, when the energy of the incident light is higher than the gap between the conduction and valence band.

Transitions can occur in both directions, from lower energy states to higher states (excitation) and vice versa (relaxation). The former requires an excitation by an external energy source, for example a photon produced by a laser which is then absorbed. The latter yields energy which occurs typically as photons in the case of an interband transition, while the intersublevel relaxation is usually nonradiative. Nonradiative interband and radiative intersublevel relaxations are also allowed, but are less efficient, since the typical time constants for these transitions are some orders of magnitude larger than for the other transitions. For example, in InAs the radiative intersublevel relaxation has a time constant of roughly 10 µs, while the nonradiative relaxation has a time constant of approximately 10 ps [Sau01].

Preparation of quantum dots

Quantum dots can be prepared with different methods. The very first was the growth of semiconductor microcrystals in a dielectric matrix and has been used by Ekimov *et al.* [Eki81]. The matrix was heated for several hours at a temperature of several hundred degrees Celsius, which yielded the crystallization of small dots. A similar technique is used to synthesize colloidal quantum dots (mainly II-VI semiconductors) [Mur93]. Another method was introduced by Reed *et al.* [Ree86], who fabricated dots by etching of quantum well structures. Especially GaAs dots can be prepared with this technique, since the growth of thin, uniform quantum wells with this material is well controlled [Jac98]. However, the common method for the fabrication of InAs quantum dots is self-organized growth.

Self-organized or self-assembled growth of quantum dots is possible, when the lattice constant of the substrate and the dot material differ considerably. For the combination of InAs dots on a GaAs substrate this mismatch is in the range of 7 %. During the growth process, normally by molecular beam epitaxy, the dot material is deposited on the substrate. Due to the lattice mismatch, only the very first monolayers grow epitaxially with the in-plane lattice constant of the substrate. Afterwards the increasing strain yields a break-down of the highly ordered structure and leads to the creation of randomly distributed clusters. This behavior is known as Stranski-Krastanov growth [Str39]. For pure InAs dots, it was demonstrated that the cluster creation will occur around 1.9 monolayers of InAs [Pet91]. The size and the shape of these clusters/dots are not completly uniform and depend on the growth temperature, the growth rate and the lattice mismatch. For example, Raymond *et al.* [Ray96] reported the growth of dots with the shape of flat lenses with diameters around 40 nm and a height of 4 nm. On the other hand, Marzin *et al.* [Mar94] demonstrated the growth of pyramide-like dots with a square base of 20 nm length and 3 nm height. The dependence of the shape on the growth temperature was later observed by Saito *et al.* [Sai99]. Furthermore, it has

thickness	material	time	temperature	comment
	As	20 min	620 °C	oxide removal
250 nm	GaAs		570 °C	smoothing buffer
	Si:As	1.7 s		delta doped layer, 5×10^{18} cm^{-3}
2 nm	GaAs			barrier layer
		15 s		ramp down Si cell temperature
2.3 ML	InAs		515 °C	dot layer at 0.007 ML/s
		15 s	515 °C	interrupt
		1 min	470 °C	ramp down sublimation temperature
20 nm	GaAs		470 °C	cap layer
		3 min	570 °C	ramp up sublimation temperature
50 nm	GaAs		570 °C	cap layer
			180 °C	fast drop of sublimation temperature
1 ML	GaAs		180 °C	Ga-enriched surface
	Si	1 h		delta doped layer, 1×10^{15} cm^{-2}
	As	2 min		anneal

Table 8.1: *Growth sequence for the preparation of the InAs quantum dot sample.*

been reported that the shape of the dots changes to elongated dots during overgrowth with GaAs [Gar97, Joy01], while the shape is conserved when overgrown with InGaAs [Son03]. Besides the shape of the dots, also the size and dot distribution exhibit a strong dependence on the growth temperature [Chu99, Pas07]. The last-mentioned authors also showed that the different sizes have a direct incfluence on the electronic structure.

8.2 Sample preparation and characterization

The specific preparation of the sample used for the near-field experiments will be discussed in the following section. It was prepared by self-assembled growth of InAs quantum dots on a semi-insulating GaAs substrate.

For the near-field experiments it was intended that the optical transitions energies were situated in the mid- and far infrared. Furthermore, the dots should be almost free of topographical signatures to avoid artifacts in the near-field signals. On the other hand, the dots should be still visible in the topography, in order to allow a classification of possible near-field signals. Hence, it was necessary to deposit a capping on top of the dots which would smoothen the surface and decrease the topography signal of the dots. Moreover, the dots had to be populated with a few electrons, otherwise no optical intraband transitions would be possible. Furthermore, it was intended to achieve a dot density of around 1x10^9 cm^{-2}. This would allow the spectroscopy at a single dot, since this corresponds to an average number of 10 dots per square micrometer.

With these requirements, the sample was grown at the Leibniz Institute for Solid State and Materials Research Dresden by Paola Atkinson. The preparation steps are

summarized in table 8.1. During the growth, the growth rate and the layers thickness were monitored with an oscillating crystal situated in the evaporation chamber. The preparation started with the removing of the oxide layer on top of the 2 inch-GaAs-wafer by sputtering with arsenic (As). The roughened surface was then smoothed by the growth of a 250 nm thick GaAs-buffer layer. The growth of this buffer was stopped by closing the shutter of the gallium evaporation cell, while opening the silicon evaporation cell. This resulted in a delta-doped surface of this buffer, which would later provide the electrons for the population of the dots. The next step was the deposition of a 2 nm GaAs barrier layer. This layer was followed by the dot layer, consisting of 2.3 monolayers (ML) of InAs, evaporated at 515 °C. The growth rate of the quantum dots was 0.007 ML/s. The dots were afterwards capped by a 70 nm thick GaAs-layer, which would smoothen the surface and thus decrease the topography signal of the dots during the near-field measurements. Towards the end of this layer, the sublimation temperature was reduced, so that the gallium (Ga) fraction in the layer increased. Furthermore, the very top of this capping layer was doped with silicon, in order to saturate possible surface states in the capping. This should prevent the recombination of electrons from the dots with surface states in the capping layer.

The first step after preparation was the analysis of the topography of the sample, which is shown in figure 8.3. The five images were recorded at different positions on the sample. Figure 8.3a shows the situation directly at the center of the wafer. The uniform brownish background indicates a very smooth and flat surface. In addition, there exist a number of bright spots that are scattered over the whole scan range. These spots appear to be elongated parallel to the vertical border of the image. Such elongated spots on a GaAs-layer on top of an InAs-layer have already been reported [Gar97, Joy01]. Hence, it can be assumed that these spots represent positions where a quantum dot is located below the capping layer. When the dots are counted, then one obtains 269 dots in the scan range which is $5 \times 5\ \mu m^2$. This corresponds to a dot density of roughly $10\ \mu m^{-2}$ which fits the intentions very well. The average measured height of the overgrown dots is roughly 2 nm. The density changes drastically, when the distance from the center increases, as depicted in the following images b)-e). Already 2 mm besides the center, the dot density drops to roughly $3\ \mu m^{-2}$. At 7 mm beside the center, the density decreased to 0, showing only the flat GaAs cap layer (see figure 8.3e).

Other important measurements were the photoluminescence (PL) at a sample from the center of the wafer. During a PL measurement a laser beam is focused on the sample (see figure 8.4). If the photon energy of the laser exceeds the band gap of the semiconductor, electrons can be excited from the valence band into excited states in the conduction band. This is accompanied by the creation of holes in the valence band. Due to the Coulomb interaction, one electron and one hole form a quasi particle which is called exciton. After a certain time, the electron and the hole recombine, accompanied by the emission of a photon. The energy of this photon is equivalent to the energy difference between the electron state and the hole state minus the exciton binding energy. When the laser power is raised, the number of generated electron-hole pairs per time increases while the number of recombining pairs stays constant, since this

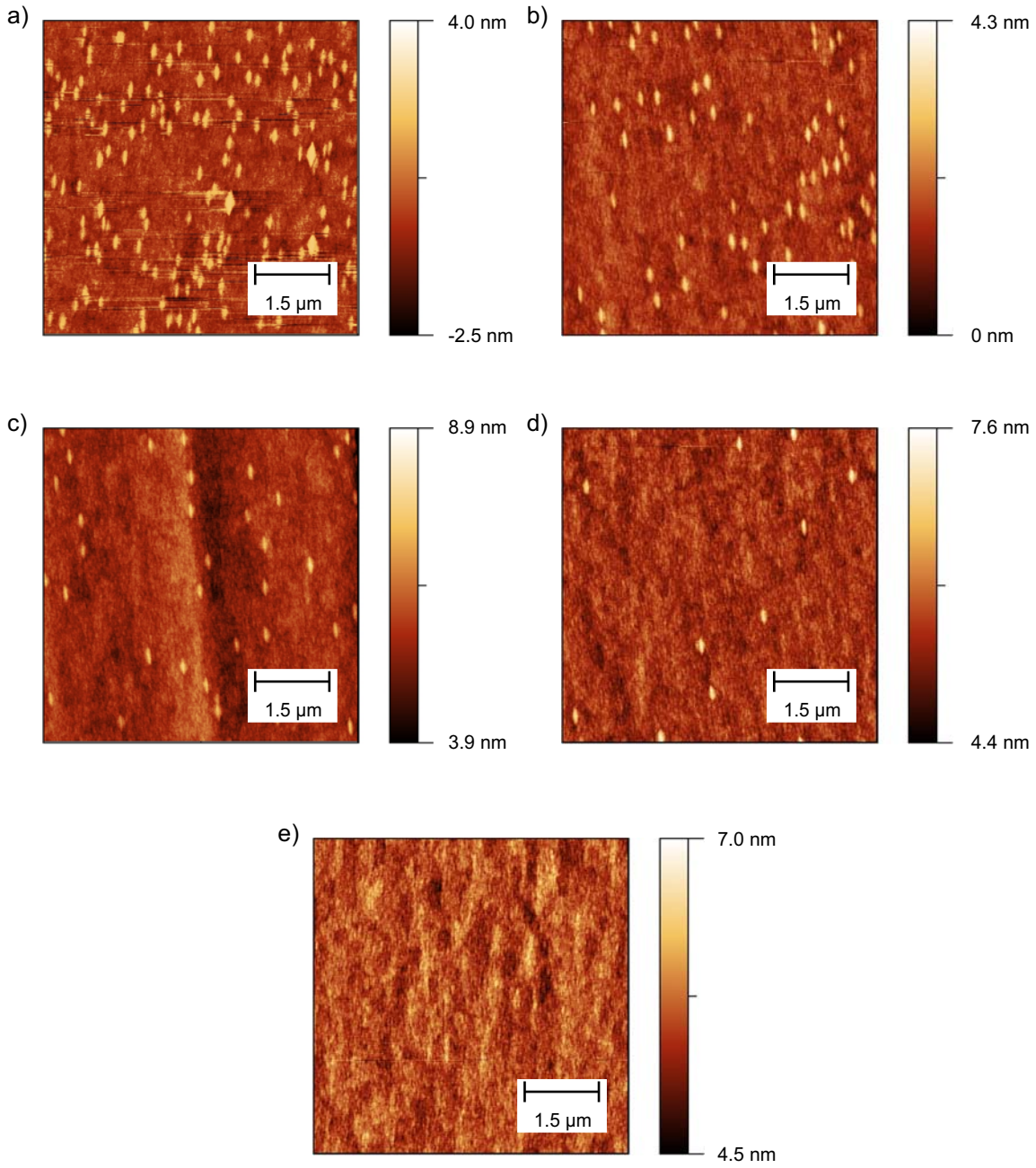

Figure 8.3: *Topography of the prepared sample for different distances from the wafer center. a) Center of the wafer. b)* 2 mm *distance. c)* 3 mm *distance. d)* 5 mm *distance. e)* 7 mm *distance. Horizontal lines are scanning artifacts.*

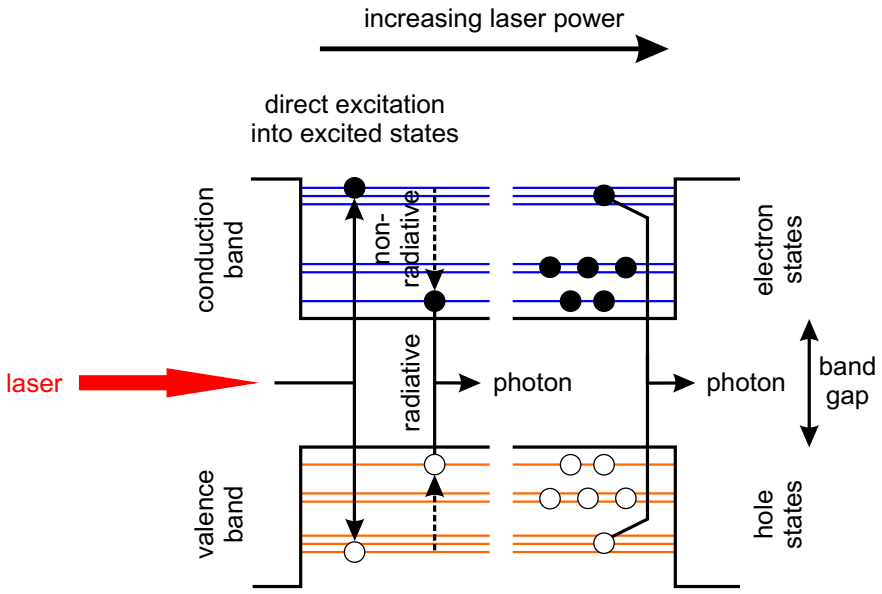

Figure 8.4: *Principle of a photoluminescence measurement.*

is determined by the exciton lifetime. Hence, the electron density in the conductance band increases, which results in the filling of the lower energy electron levels (s- and p-level). Thus, the fast nonradiative intraband relaxation to the ground state is not possible anymore, so that slow radiative recombination of higher levels (e. g. from the d-level) becomes possible. Hence, photoluminescence can be used to determine the energy levels in the conduction and valence band. But PL invariably yields the sum of the electron and hole energies, since the emitted photons are created during the recombination of electrons and holes. Typically, about 70 % of the photoluminescence energy difference between different peaks can be attributed to the intersublevel spacing in the conduction band [Asl08]. This value accounts for the exciton binding energy and the energy of the participating hole state and has to be kept in mind when interpreting PL spectra.

The first PL measurement was performed with a setup that utilized a cw laser, operating at 532 nm, and a normal incidence configuration. The temperature of the sample was 15 K and the result is depicted in figure 8.5a (black curve). It shows two distinct peaks at 1213 nm and 1150 nm. Similar emission wavelengths have already been reported by Joyce *et al.* [Joy00] for InAs quantum dots grown at 0.0065 ML/s and overgrown with 70 nm GaAs. Hence, the first peak can be attributed to a recombination of an electron and a hole of the ground state, while the second peak is a recombination of an exciton from the first excited state. The separation of these levels is 63 nm or 56 meV. After this measurement, the sample was successively heated to 70 K, 150 K and 300 K. At each temperature the measurement was repeated, so that the temperature dependence of the emission could be obtained. It is visible in the figure that both peaks shift towards lower energies. At 300 K, the ground state emission is at 1308 nm and the first excited state emits at 1236 nm. Even though the shift is

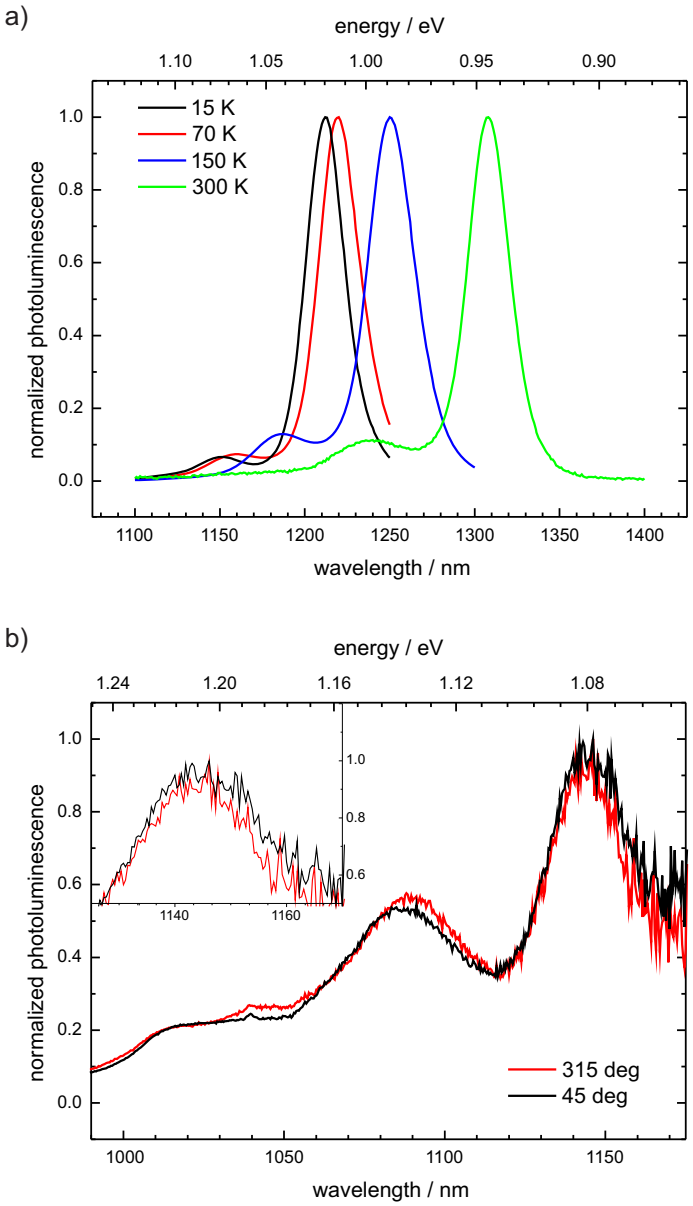

Figure 8.5: *Photoluminescence measurements on InAs quantum dots. a) Measurements with the cw-setup for different temperatures. b) Measurements with the pulsed setup for different polarizations of the incident light at* 15 K*. The inset shows a magnification of the peak around* 1140 nm*.*

roughly 77 meV, the separation of both levels is constant (55 meV). This behavior can be compared to the results of Joyce *et al.* [Joy00] and Chu *et al.* [Chu99], who observed similar PL emissions at room temperature.

In a second experiment, the sample was investigated with a setup that utilized a pulsed laser, operating at 800 nm, again under normal incidence. Due to higher intensities in the focus than with the cw-setup, higher excited states could be probed. Furthermore, the setup provided a possibility to control the polarization of the incident

beam. Hence, it was possible to measure the photoluminescence spectra of the sample for different orientations of the electric field vector with respect to the elongated dot axis (see figure 8.3). The spectra are shown in figure 8.5b. Both curves show three distinct peaks at 1144 nm, 1083 nm and 1015 nm. The position of the first peak roughly coincides with the peak at 1153 nm of figure 8.5a. Hence, this peak corresponds to the first excited state. The shift of the peak is probably due to the spectral sensitivity of the detector, which is almost zero at this wavelength (indicated by the large noise). The second peak can then be attributed to the second excited state and the third peak to the third excited state. The difference between the first and second excited state is 61 meV and the separation of the second and third peak relative to each other is 76 meV. From the previous measurements it can be assumed that the separation of these levels is the same at room temperature. Between the measurement of the curves in figure 8.5b, the polarization with respect to the longer axis of the dots was rotated by 90°, but this had almost no effect on the positions of the peak. Especially the emission from the first excited state should be shifted when the dots exhibit a pyramid like structure [Kim98]. As this is not the case (see inset in figure 8.5b), it can be assumed that the dots have a lens like structure [Wil00] which is in contradiction to the observed topographical asymmetry. Otherwise, it cannot be excluded that this asymmetry is a result of stress in the GaAs cap layer and that the dots are indeed symmetric. This is also supported by the agreement of the PL measurements with the results of Joyce *et al.* [Joy00] and Chu *et al.* [Chu99], as their PL measurements were accompanied by studies of the dots topographical structure which also showed symmetric dots.

As already mentioned, photoluminescence spectroscopy is not able to show intersublevel transitions directly. For this, intraband absorption and transmission measurements in the mid infrared would be necessary. But such measurements on this sample did not show any signatures of the dots, as it only contains one layer of InAs dots. Hence, the absorption was much too low to be detectable with common methods.

Finally, it has to be considered that the near-field measurements were solely performed at room temperature. Otherwise, most published data about InAs quantum dots were obtained at low temperatures. Nevertheless, both can be compared, as with the increasing temperature almost no change in the peak separation occurs. This was demonstrated at the present sample and also by Joyce *et al.* [Joy00]. All peaks are shifted towards lower energy, but the energetic difference stays constant.

8.3 Near-field measurements in the mid infrared

Up to now, only a few publications deal with spectroscopy of single quantum dots that is based on scanning probe techniques. In the visible range, Ogawa *et al.* [Oga10] used the scattering-type near-field microscopy to study interband transitions in single Germanium quantum dots. In the near-infrared, Hess *et al.* [Hes94] used an aperture near-field microscope to perform photoluminescence measurements on single dots. Furthermore, Houel *et al.* [Hou07] and Sauvage *et al.* [Sau11] investigated intersublevel transitions in InAs quantum dots by infrared absorption spectroscopy, where the cantilever oscillation due the local thermal deformation of the sample is monitored.

However, scattering-type near-field microscopy has not yet been used to study intersublevel transitions in single quantum dots in the mid- and far-infrared. Hence, the contrast mechanisms are not known yet. Thus, the present near-field measurements were performed in wavelength ranges where intersublevel absorptions are known from literature. Unfortunately, there were some conflicts with the beam time schedule, so that the very first near-field experiments had to be performed without the above discussed PL measurements. Thus, the experiments were performed at 85 meV (14.5 µm), where a transition was calculated by Zhang *et al.* [Zha04] and demonstrated by Aslan *et al.* [Asl03]. Another transition exhibits an energy of 120 meV [Hou07, Vuk06], which is equal to 10.3 µm. Both transitions will be discussed separately. Nevertheless, a doubtless classification of the transition energies is not possible, even with numerical calculations. The major issue is the unknown shape of the dots, which has a significant influence on the electronic structure.

Transition at 85 meV

The main part of these investigations were the spectral measurements similar to the experiments on the boron implanted sample. A line that contained at least one quantum dot, was scanned repeatedly while the wavelength of the incident light was changed after a specific number of loops. Topography and near-field signal were measured at the same time, so that possible events in the near-field channel can be compared to the topography. Such a measurement is depicted in figure 8.6 for s-polarized light. The bright vertical line in the topography channel represents an InAs quantum dot. Comparing the near-field channel to this topography image reveals that there exists a wavelength range where the near-field signal on top of the dot is lower than besides the dot. From this image the near-field spectrum of this dot was obtained by averaging over all lines recorded with the same wavelength and calculating the near-field contrast according to equation (2.52). The result is depicted in figure 8.7, where the wavelengths are already converted into energy. The figure shows the experimental data as well as the Gaussian fit that is in best agreement to the data. The peak of the Gaussian is at 84 meV with a full width half maximum (FWHM) of 8 meV. This value is in the expected range for the calculated intersublevel transition from the first excited to the second excited level at room temperature [Zha04, Bou08]. Furthermore, similar values for this transition energy were obtained by absorption measurements on InAs quantum dots [Pan98, Asl03] with a polarization perpendicular to the growth axis. This is also in agreement with the performed measurements, as s-polarized light in the developed setup means in-plane or perpendicular to the growth axis. Furthermore, a transition energy of roughly 80 meV can be derived from the PL measurements, when it is assumed that the peak of the first excited state (1144 nm) is blue shifted due to the participating first excited hole state, since a recombination with a hole in the ground state is forbidden due to parity violation [Woj97]. The peak of the second excited state in the PL (1083 nm), however, is not shifted, since it originates probably from a recombination with a hole in the ground state, which is allowed (see figure 8.8). With this assumption the separation of the first and second excited electron state is roughly

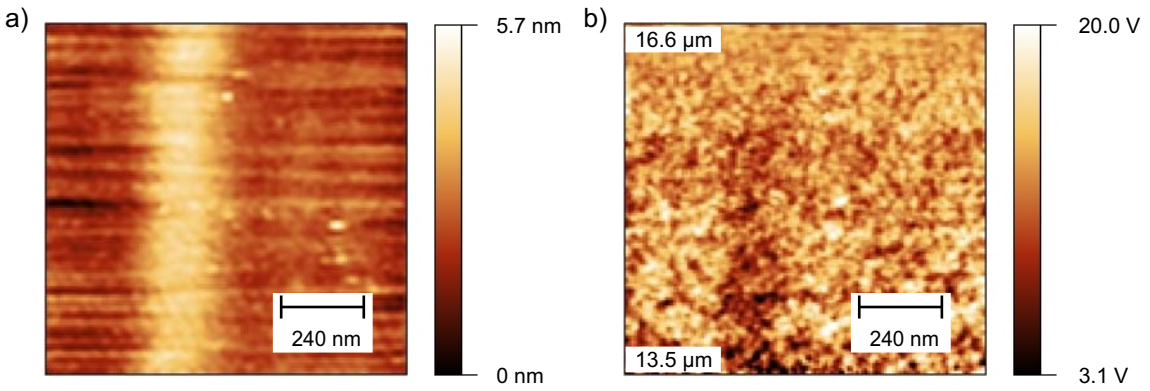

Figure 8.6: *a) Topography and b) 2nd harmonic near-field signal of a spectral measurement with s-polarized light between* 13.5 µm *(at the bottom of the images) and* 16.6 µm *(at the top of the images). The data has been filtered to enhance the contrast.*

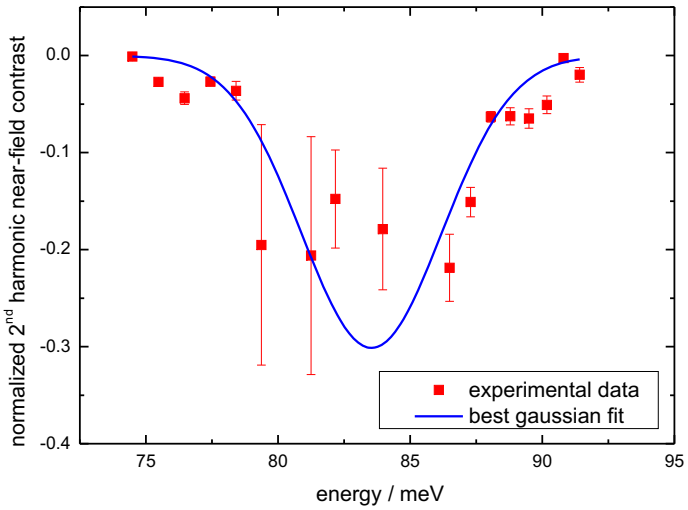

Figure 8.7: *Near-field spectrum of a single InAs quantum dot for an energy range of* 75 meV *to* 95 meV.

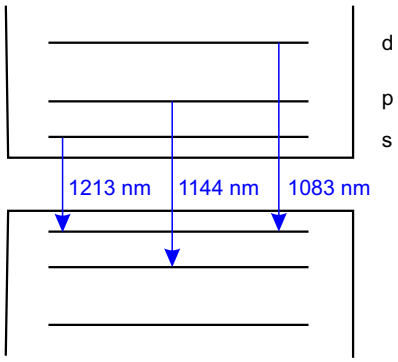

Figure 8.8: *Allowed optical transitions from the conduction band to the valence band in InAs quantum dots. A recombination of an electron in the first excited state with a hole in the ground state is not allowed. The emission wavelengths are denoted next to the corresponding transition.*

78 meV instead of 61 meV as indicated by the photoluminescence. That is in agreement with the result of the near-field measurements. Nevertheless, an exact assignment of the transition is not possible. For example, Vukmirovic *et al.* [Vuk06] attributed the energy of 85 meV to a transition from the ground state to the first excited state by.

To further corroborate this spectrum, additional near-field measurements were performed. These were scans at a fixed wavelength with a least two dots in the scan range. If the near-field signatures of numerous dots are similar to each other, it can be assumed that the previously measured spectrum was not influenced by the particular shape and dimensions of the measured dot. Moreover, another measurement was performed with a polarization parallel to the growth axis at a photon energy of 86 meV. All measurements are summarized in figure 8.9. The left column of this figure depicts the topography channel and the right column represents the 2^{nd} harmonic near-field signal. Figures 8.9a to 8.9f show the measurements with s-polarized light, while figures 8.9g and 8.9h show the measurement with p-polarized light. For the s-polarized measurement at 86 meV (figures 8.9c and d), the optical near-field signal shows a set of dark spots, which coincides with the signatures of the quantum dots in the topography channel. Furthermore, these near-field signatures disappeared when the wavelength was changed to 75 meV. When the energy was changed to 91 meV the contrast decreased but did not vanish completely. Both corresponds to the already discussed near-field spectrum of a single quantum dot. Hence, it can be assumed that the spectrum has a general validity for the majority of the dots on that sample. Moreover, the signatures also disappeared when the polarization was changed from perpendicular to parallel to the growth axis. Unfortunately the images 8.9g and 8.9h do not show the same position as they were from a different measurement series. Nevertheless they can be used for interpretation, as the s-polarized signatures were the same in both series. This behavior corresponds to the strong polarization dependence of the p-d transition [Asl03].

An explanation of this signature with the simple dipole model is rather difficult, since it requires an expression for the dielectric function that accounts for the intersublevel

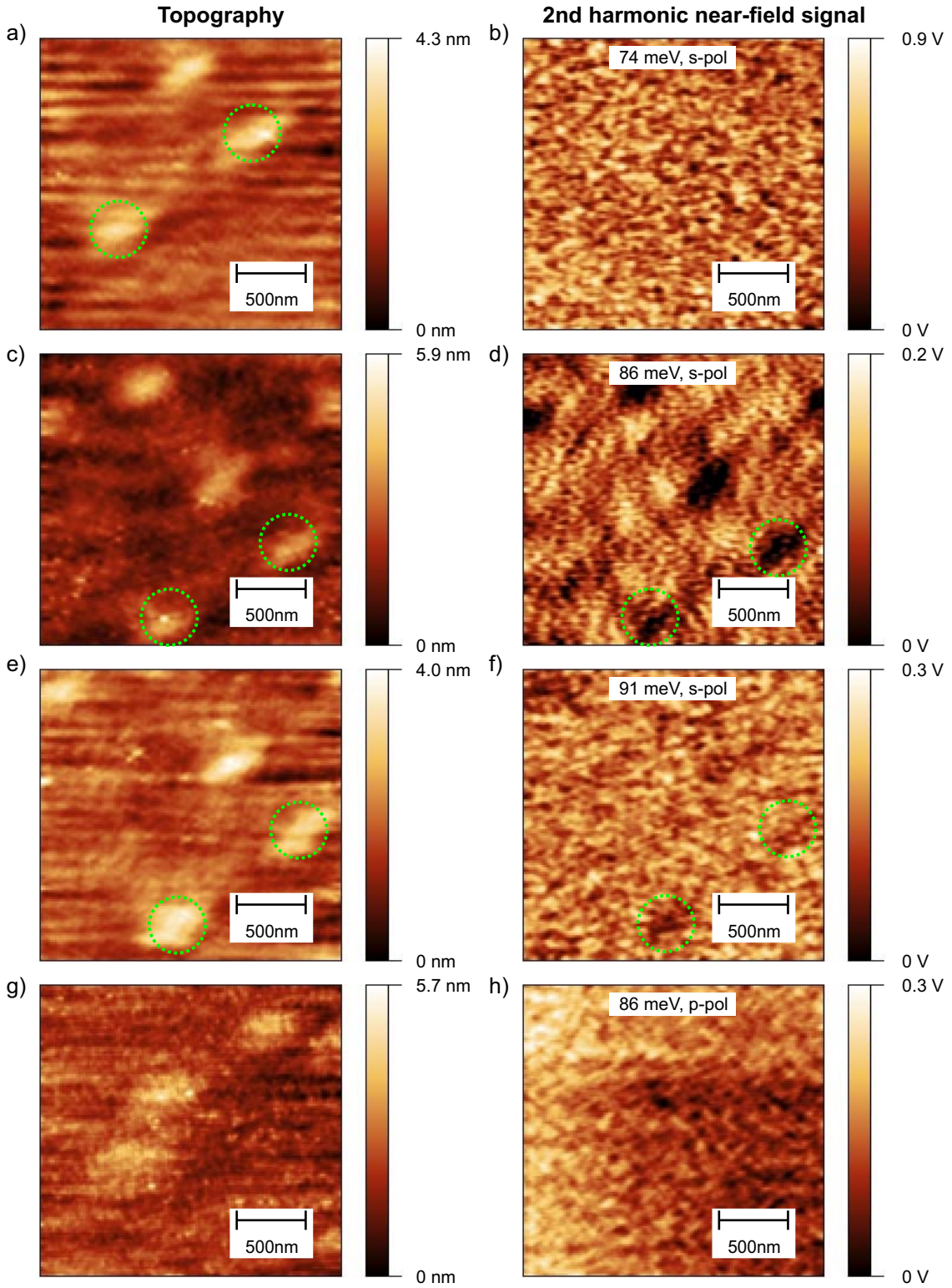

Figure 8.9: *Near-field measurements at different energies. a) Topography and b) 2^{nd} harmonic near-field signal for an energy of* 74 meV *(s-polarized). c) and d) for* 86 meV*. e) and f) for* 91 meV*. Two dots that are the same in all images are encircled green. g) and h) show the measurement at* 86 meV*, but p-polarized.*

transitions in the conduction band. Without those contributions the dielectric functions of InAs [Lor65] and GaAs [Hol77] are almost flat in this wavelength range and the measured contrast is not predicted by the dipole model. A simplified approach may be the model of the intraband transition at 85 meV as a resonance in the form of a Lorentz oscillator with a characteristic frequency that is equivalent to the transition energy (685 cm^{-1}). With these assumptions, the dipole model predicts a clear contrast at the transition energy. However, the transition energy as well as the broadening have to be known beforehand.

To sum it up briefly, the measurements showed a clear near-field signature that is consistent with the energy and the polarization of the p-d transition. Moreover, the small width of this transition at room temperature indicates a strong confinement of the participating levels which excludes a transition to the continuum. The measured transition energy is corroborated by the PL measurements, when it is assumed that the peak of the first excited state is blue shifted.

Transition at 120 meV

The second wavelength range was set around 120 meV, where the s-d transition is expected. This is supported by the PL measurements, since the difference between the ground state and the second excited state at 15 K is roughly 117 meV. However, this violates the selection rules discussed previously [Asl03]. A correct assignment of the transition may, however, be difficult, as shown by Houel *et al.* [Hou07] who initially attributed it to the s-d transition, but revised this assignment later to a transition to the wetting layer [Hou10]. Also Boucaud *et al.* [Bou08] and Pan *et al.* [Pan98] attributed this energy to a transition from the ground state to the second excited state.

The performed near-field measurements were similar to the previously discussed measurements. At the beginning a spectral response of the quantum dots was measured. This is shown in figure 8.10. The topography channel shows three bright stripes that represent the quantum dots. In the near-field signal, these stripes can be recognized again, but only for a certain wavelength range. From these data, the near-field spectrum of these dots was derived which is depicted in figure 8.11. The Gaussian fit of the experimental data has its peak at 123 meV with a FWHM of 5 meV. This is in good agreement with the expectations. Furthermore it can be seen that the contrast is much less than compared to the previously discussed transition. It is roughly 6 %, while the p-d transition showed an optical contrast of almost 20 %. That may indicate that the transition strength is weaker or that the polarization dependence is different.

To cross check these results, scans at certain wavelengths around the peak were performed. Those are shown in figure 8.12. In this figure, topography and 2^{nd} harmonic near-field signal are depicted for different energies similar to figure 8.9. Figures 8.12a and 8.12b show the measurement for 118 meV, 8.12c and 8.12d for 122 meV and 8.12e and 8.12f for 125 meV. The last two images 8.12g and 8.12h show the measurement at 122 meV and p-polarized incident light. The highest contrast can be observed for s-polarized light at 122 meV. A set of dark spots can be seen in the center of the scan range. Comparing this to the topography reveals a good agreement of these spots with

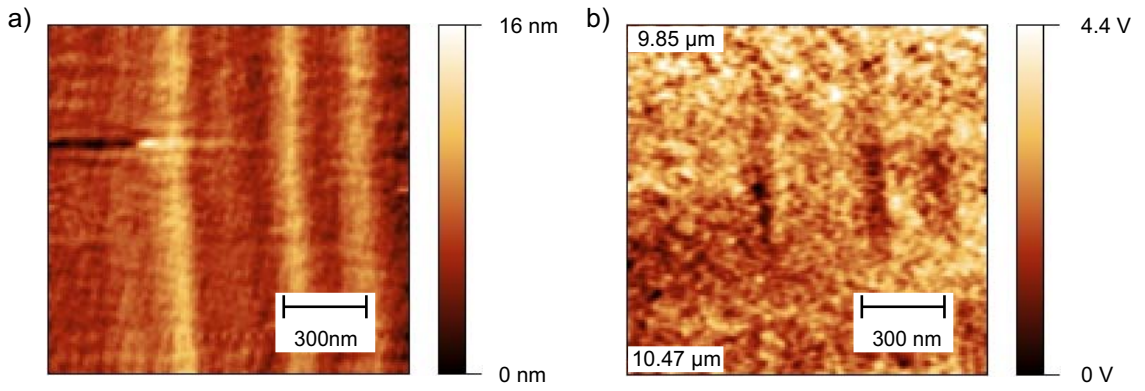

Figure 8.10: *a) Topography and b) 2nd harmonic near-field signal of a spectral measurement with s-polarized light between* 9.85 µm *(at the top of the images) and* 10.47 µm *(at the bottom of the images). The data has been filtered to enhance the contrast.*

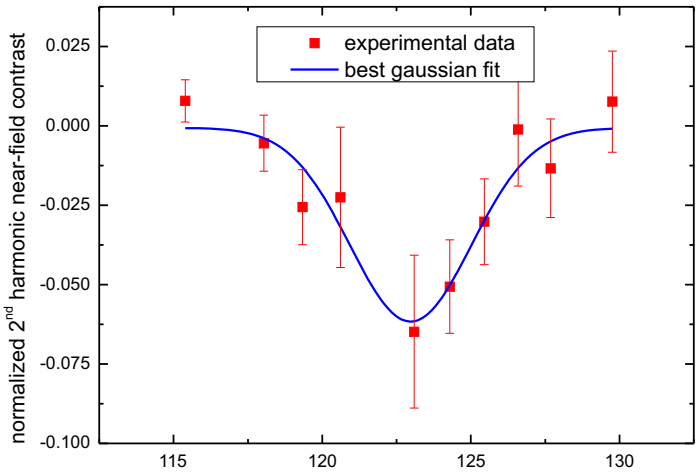

Figure 8.11: *Near-field spectrum of single InAs quantum dots for an energy range of* 115 meV *to* 125 meV.

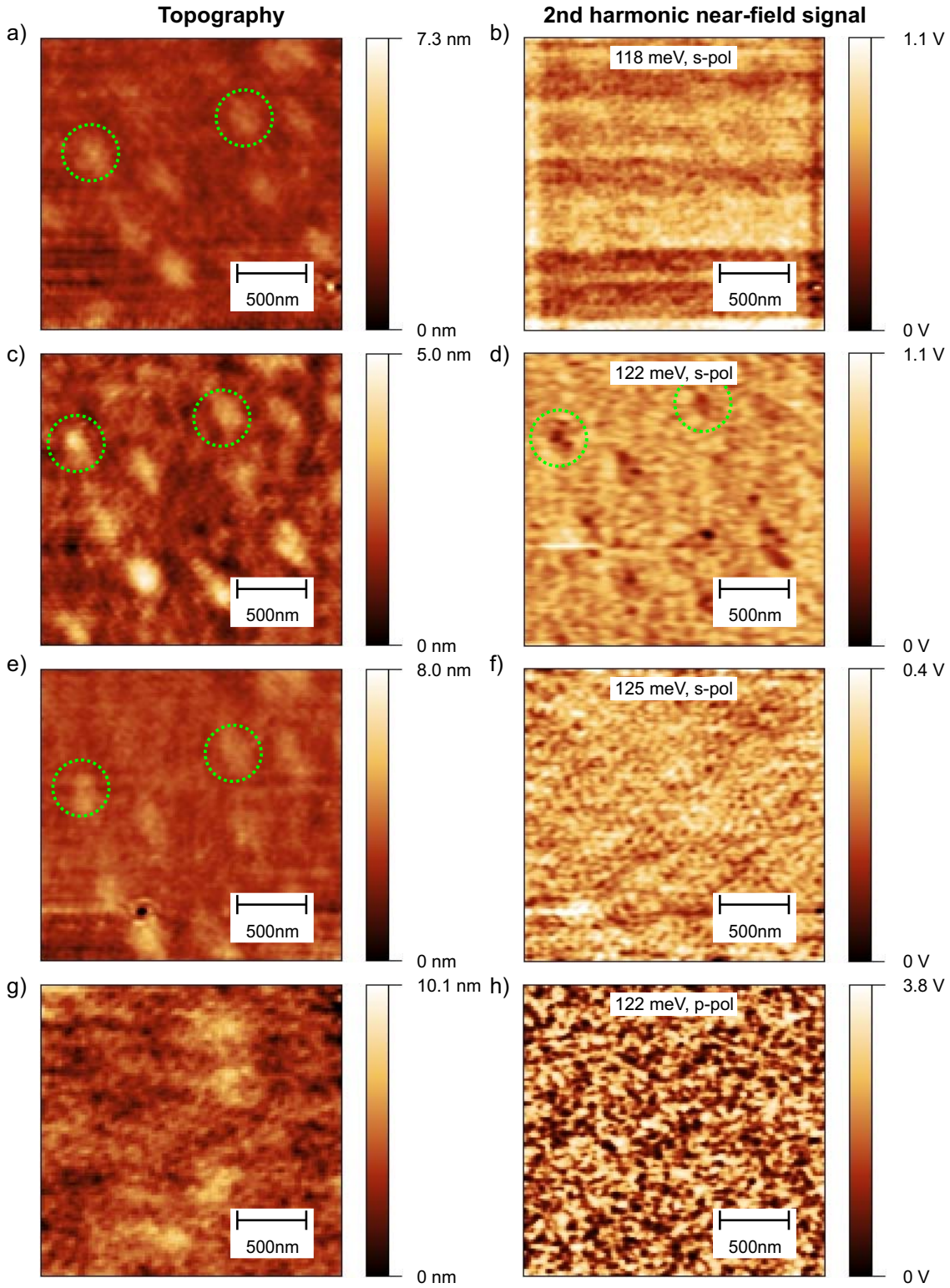

Figure 8.12: *Near-field measurements at different energies. a) Topography and b) 2^{nd} harmonic near-field signal for an energy of* 118 meV *(s-polarized). c) and d) for* 122 meV*. e) and f) for* 125 meV*. Two dots that are the same in all images are encircled green. g) and h) show the measurement at* 122 meV*, but p-polarized.*

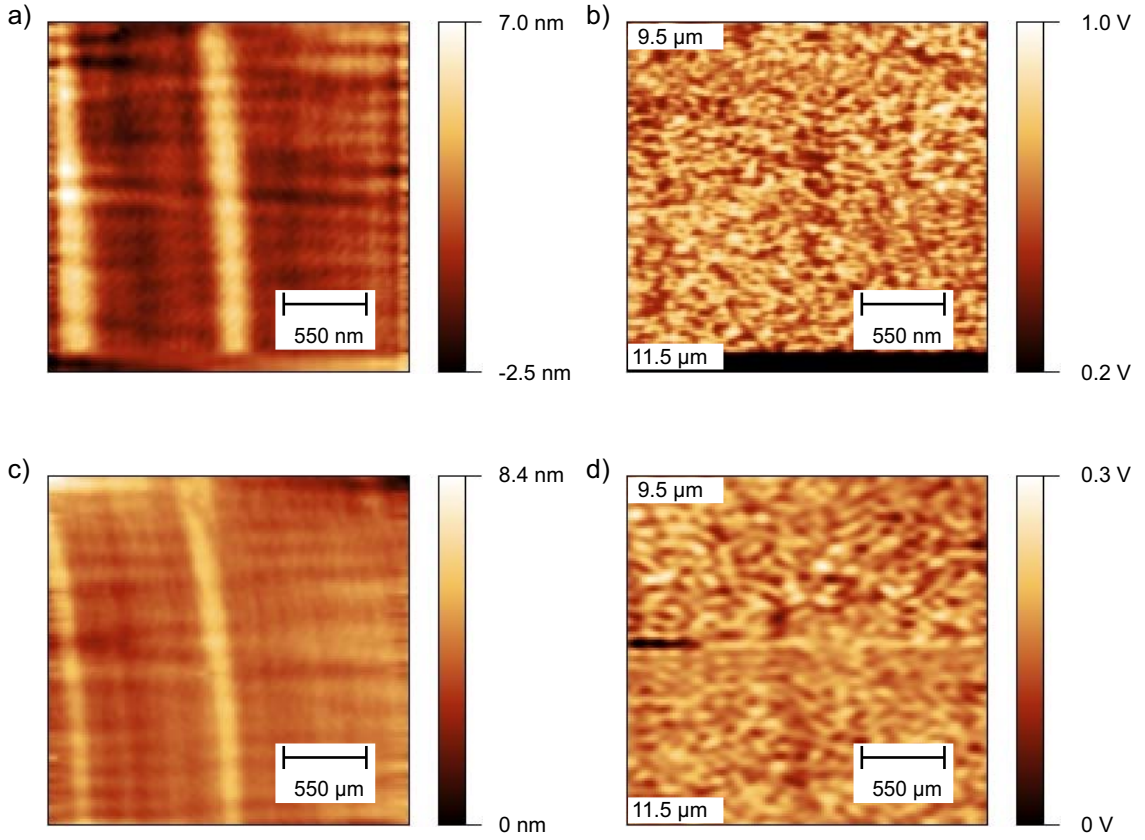

Figure 8.13: *a) Topography and b) 2nd harmonic near-field signal of a spectral measurement without the polarization filter in front of the detector. The wavelength range is* 9.5 µm *(at the top of the images) and* 11.5 µm *(at the bottom of the images). c) and d) show the same measurement, but with the polarization filter in front of the detector, transmitting just s-polarized radiation.*

positions where quantum dots can be observed. This is a clear indication that these features are related to the dots. The contrast vanished completely when the wavelength was changed to 118 meV and 125 meV. It disappeared also, when the polarization was changed to p-polarized. Hence, the spectrum shown in figure 8.11 is confirmed by these scans.

The results show a clear signature at an energy that is comparable to the separation between the ground state and the second excited state. However, this transition is essentially forbidden in the parabolic Fock model, but more realistic $\mathbf{k} \cdot \mathbf{p}$ band structure calculations show that it is slightly allowed [Bou08]. But, according to these calculations it exhibits a polarization along the growth axis which would mean p-polarized in the SNOM setup. That is in contradiction to the measured polarization dependence.

To clarify the origin, another measurement was done. It addressed the polarization of the incident light and the light which is collected by the detector. For this purpose, a polarization filter was inserted in front of the detector. It was set to a polarization perpendicular to the growth axis. The incident polarization was also set to be perpendicular to the growth axis (s-polarization). Hence, the detected near-field

amplitude would only show near-field components with the same polarization as the incident beam. With this configuration, two spectral measurements were performed that are shown in figure 8.13. 8.13a and 8.13b show the measurement without the filter (topography and 2^{nd} harmonic near-field amplitude) and 8.13c and 8.13d show the measurement with the filter while all other parameters were kept unchanged. It can be seen that the filter did not suppress the contrast which would have been the case if it originated from p-polarized components. Unfortunately, due to beam time limitations it was not possible to measure with the filter set to p-polarized. That would have clarified this issue additionally. Otherwise, the previous scans showed no p-polarized contrast at all. Hence, it can be expected that a measurement with the filter set to p-polarized would not show any contrast either.

In summary, a clear contrast was obtained at an energy consistent with the separation between the s- and d-levels. This is also supported by the small FWHM which indicates a transition between two confined electronic states. On the other hand, the very low contrast in comparison to the previously discussed transition can be an indication for the violated selection rules. If this (forbidden) transition was allowed, a much higher contrast could be expected. The disagreement between the expected and the measured polarization may be explained by additional excitations along the growth axis due to the interaction of the tip-dipole and the image dipole. It has been shown theoretically by Bryant [Bry97] that such components can be expected in near-field microscopy.

8.4 Summary

This chapter discussed the near-field measurements on InAs quantum dots. With the help of the free-electron laser it was possible to show two specific near-field signatures which were attributed to intersublevel transitions in the quantum dots. Spectral measurements were used to determine the energy of those transitions, as well as their broadening. In both cases, the broadening was $5 - 8$ meV which is an indication of bound-to-bound transitions. It is consistent with the homogeneous broadening of single quantum dots that originates from longitudinal optical phonon scattering and which is in the range of roughly 10 meV [Mat00]. The low-energy transition at 84 meV was attributed to a transition from the first excited state to the second excited electron state (p-d transition), while the transition at 123 meV was attributed to the transition from the ground state to the second excited state (s-d transition). The electronic structure of the dots according to the near-field measurements is depicted in figure 8.14.

The obtained results were discussed with respect to the predictions of photoluminescence measurements, as well as with respect to already published data for intersublevel transitions in InAs quantum dots. In both cases a general agreement could be achieved, although specific issues remain open, especially the different polarization of the s-d transition compared to the predictions by literature. A detailed discussion of this problem was not possible due to the lack of granted shifts and a long-term machine shut-down after the last performed measurements.

This is the first time ever that it was possible to perform intraband spectroscopy on single InAs quantum dots by means of their near-field signature. It was also pos-

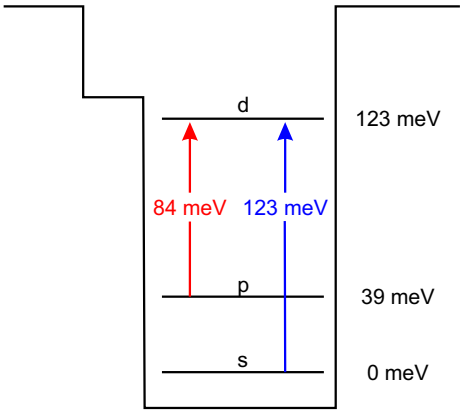

Figure 8.14: *Electronic configuration of the InAs quantum dots on the sample as measured by scattering-type near-field infrared microscopy.*

sible to corroborate the assumption from the implanted silicon sample that near-field microscopy can probe buried structures at least in the range of the tip diameter.

9 Conclusion and outlook

The major issue of this thesis was the setup of a scattering-type near-field optical microscope at the beamline of the free-electron lasers in the Forschungszentrum Dresden-Rossendorf. It was demonstrated with the help of two different sample systems that the combination of a home built s-SNOM with the widely tunable free-electron laser was successful and that it provides access to numerous scientific issues.

Using locally implanted silicon, the built setup was characterized and compared with respect to published data of near-field experiments at similar p-doped sample systems. The sample was used as a benchmark to verify the spectroscopic possibilities expected from the tunability of the light source. The results were not only compared to the literature, but also verified by different measuring techniques. Spectral measurements with variable wavelengths and interferometric measurements with a fixed wavelength yielded almost the same results, which were in excellent agreement to the expectations from the sample preparation and the literature. Furthermore, they showed that the applied dipole-model is also applicable for buried structures.

The capabilities of the setup were also demonstrated by the spectroscopy of single InAs quantum dots. As no literature is available on this topic, it appears that this is the first time ever that such measurements could be performed. The s-SNOM was used to map optical transitions within the conduction band of the quantum dot, where it was possible to obtain clear near-field signatures at energies which can be related to intersublevel transitions in the conduction band. The measured data showed very small broadening which indicates that the signatures can be assigned to bound-to-bound transitions. These measurements further corroborated that scattering-type near-field microscopy can probe structures that are buried in a depth at least equal to the diameter of the probe.

At the end of this thesis, different possibilities for further investigations should be mentioned. On the technical side this affects the combination with the free-electron laser, especially, the increase of the signal-to-noise-ratio is a major issue. This was a critical point during the investigations of the boron implanted sample. Here a decrease of the diameter of the focus on the tip should be attacked first. Another approach is the amount of the detected light which should be increased by using a different illumination scheme. It should also be investigated further, how an interferometer can be realized in combination with the FEL, even though this failed during this thesis. This would not only provide the information about the near-field phase, but would also increase the signal-to-noise-ratio.

Scientifically, the sample of the InAs dots exhibits the greatest potential, as it was not possible to investigate the problems of the polarization dependence of the s-d-transition due to lack of beamtime. It is also possible, to investigate further transitions, like the

s-p-transition which should be around 31 µm. It would also be very interesting to investigate this sample with a low temperature SNOM that is under development, because a linewidth in the µeVrange could be expected. Another interesting approach is the modulation of the occupation of the dots at room temperature. If the obtained near-field signatures originate from intersublevel transitions, they should vanish if the dots are empty. That can be achieved by applying a voltage that would deform the band structure of the dot so that the electrons can escape from the dots (depleted quantum dots). Unfortunately, this requires a top contact that does not produce an additional near-field signal which could possibly superimpose the small signals from the dots.

Bibliography

[Abb73] E. Abbe. *Beiträge zur Theorie des Mikroskops und der mikroskopischen Wahrnehmung.* Archiv für Mikroskopische Anatomie **9**, 413 (1873).

[Abb82] E. Abbe. *Die Beziehung zwischen Apertur und Vergrößerung beim Mikroskop (The Relation of Aperture and Power in the Microscope).* Journal of the Royal Society **2**, 360 and 460 (1882).

[Ahr95] A. G. Ahrens (Editor). *Mineral Physics and Crystallography* (American Geophysical Union, Washington, 1995).

[Ale89] S. Alexander, L. Hellemans, O. Marti, J. Schneir, V. Elings, P. K. Hansma, M. Longmire, and J. Gurley. *An atomic-resolution atomic-force microscope implemented using an optical lever.* Journal of Applied Physics **65**, 164 (1989).

[Ash72] E. A. Ash and G. Nicholls. *Super-resolution aperture scanning microscope.* Nature **237**, 510 (1972).

[Asl03] B. Aslan, H. C. Liu, M. Korkusinski, S.-J. Cheng, and P. Hawrylak. *Response spectra from mid- to far-infrared, polarization behaviors, and effects of electron numbers in quantum-dot photodetectors.* Applied Physics Letters **82**, 630 (2003).

[Asl08] B. Aslan, C. Y. Song, and H. C. Liu. *On the spectral response of quantum dot infrared photodetectors: Postgrowth annealing and polarization behaviors.* Applied Physics Letters **92**, 253118 (2008).

[Aub03] S. Aubert, A. Bruyant, S. Blaize, R. Bachelot, G. Lerondel, S. Hudlet, and P. Royer. *Analysis of the interferometric effect of the background light in apertureless scanning near-field optical microscopy.* Journal of the Optical Society of America B **20**, 2117 (2003).

[Bab37] J. Babinet. *Mémoires d'optique météorologique (Memoirs on meteorological optics).* Comptes Rendus de l'Académie des Sciences **4**, 638 (1837).

[Bau09] C. Baumgart, M. Helm, and H. Schmidt. *Quantitative dopant profiling in semiconductors: A Kelvin probe force microscopy model.* Physical Review B **80**, 085305 (2009).

[Beh08] N. Behr and M. B. Raschke. *Optical antenna properties of scanning probe tips: Plasmonic light scattering, tip-sample soupling, and near-field enhancement.* Journal of Physical Chemistry C **112**, 3766 (2008).

[Bey88] H. Beyer and H. Riesenberg. *Handbuch der Mikroskopie* (VEB Verlag Technik, Berlin, 1988).

[Bil06] L. Billot, M. Lamy de la Chapelle, D. Barchiesi, S.-H. Chang, S. K. Gray, J. A. Rogers, A. Bouhelier, P.-M. Adam, J.-L. Bijeon, G. P. Wiederrecht, R. Bachelot, and P. Royer. *Error signal artifact in aperture less scanning near-field optical microscopy.* Applied Physics Letters **89**, 023105 (2006).

[Bin81] G. Binnig, H. Rohrer, C. Gerber, and E. Weibel. *Tunneling through a controllable vacuum gap.* Applied Physics Letters **40**, 178 (1981).

[Bin86] G. Binnig, C. F. Quate, and C. Gerber. *Atomic force microscope.* Physical Review Letters **56**, 930 (1986).

[Boh83] C. F. Bohren and D. R. Huffmann. *Absorption and Scattering of Light by Small Particles* (John Wiley & Sons, Inc., New York, 1983).

[Bou08] P. Boucaud, S. Sauvage, and J. Houel. *Intersublevel transitions in self-assembled quantum dots.* Comptes Rendus Physique **9**, 840 (2008).

[Bra90] C. A. Brau. *Free-Electron Lasers* (Academic Press, Inc., Boston, 1990).

[Bre06] M. Brehm, T. Taubner, R. Hillenbrand, and F. Keilmann. *Infrared spectroscopic mapping of single nanoparticles and viruses at nanoscale resolution.* Nano Letters **6**, 1307 (2006).

[Bre08] M. Brehm, A. Schliesser, F. Cajko, I. Tsukerman, and F. Keilmann. *Antenna-mediated back-scattering efficiency in infrared near-field microscopy.* Optics Express **16**, 11203 (2008).

[Bry97] G. W. Bryant. *Probing quantum nanostructures with near-field optical microscopy and vice versa.* Applied Physics Letters **72**, 768 (1997).

[Ceb06] M. Cebula. *Phasengeregelte homodyne Interferometrie für s-SNOM.* Master's thesis (Diplomarbeit), Technische Universität Dresden (2006).

[Che03a] H.-T. Chen, R. Kersting, and G. C. Cho. *Terahertz imaging with nanometer resolution.* Applied Physics Letters **83**, 3009 (2003).

[Che03b] O. Cherniavskaya, L. Chen, V. Weng, L. Yuditsky, and L. E. Brus. *Quantitative noncontact electrostatic force imaging of nanocrystal polarizability.* Journal of Physical Chemistry B **107**, 1525 (2003).

[Chu99] L. Chu, M. Arzberger, G. Böhm, and G. Abstreiter. *Influence of growth conditions on the photoluminescence of self-assembled InAs/GaAs quantum dots.* Journal of Applied Physics **85**, 2335 (1999).

[Cvi07] A. Cvitkovic, N. Ocelic, and R. Hillenbrand. *Analytical model for quantitative prediction of material contrasts in scattering-type near-field optical microscopy.* Optics Express **15**, 8550 (2007).

[Dar30] C. G. Darwin. *The diamagnetism of the free electron.* Mathematical Proceedings of the Cambridge Philosophical Society **27**, 86 (1930).

[Dea77] D. A. G. Deacon, L. R. Elias, J. M. J. Madey, G. J. Ramian, H. A. Schwettman, and T. I. Smith. *First operation of a free-electron laser.* Physical Review Letters **38**, 892 (1977).

[Deu08] B. Deutsch, R. Hillenbrand, and L. Novotny. *Near-field amplitude and phase recovery using phase-shifting interferometry.* Optics Express **16**, 494 (2008).

[Dun99] R. C. Dunn. *Near-field scanning optical microscopy.* Chemical Reviews **99**, 2891 (1999).

[Eki81] A. I. Ekimov and A. A. Onushchenko. *Quantum size effect in three-dimensional microscopic semiconductor crystals.* JEPT Letters **34**, 363 (1981).

[Eli76] L. R. Elias, W. M. Fairbank, J. M. J. Madey, H. A. Schwettman, and T. I. Smith. *Observation of stimulated emission of radiation by relativistic electrons in a spatially periodic transverse magnetic field.* Physical Review Letters **36**, 717 (1976).

[Est07] R. Esteban, R. Vogelgesang, and K. Kern. *Tip-substrate interaction in optical near-field microscopy.* Physical Review B **75**, 195410 (2007).

[Est09] R. Esteban, R. Vogelgesang, and K. Kern. *Full simulations of the apertureless scanning near field optical microscopy signal: achievable resolution and contrast.* Optics Express **17**, 2518 (2009).

[Foc28] V. Fock. *Bemerkung zur Quantelung des harmonischen Oszillators im Magnetfeld.* Zeitschrift für Physik A **47**, 446 (1928).

[Fuk05] T. Fukuma, M. Kimura, K. Kobayashi, K. Matsushige, and H. Yamada. *Development of low noise cantilever deflection sensor for multienvironment frequency-modulation atomic force microscopy.* Review of Scientific Instruments **76**, 053704 (2005).

[Gar97] J. M. García, G. Medeiros-Ribeiro, K. Schmidt, T. Ngo, J. L. Feng, A. Lorke, J. Kotthaus, and P. M. Petroff. *Intermixing and shape changes during the formation of InAs self-assembled quantum dots.* Applied Physics Letters **71**, 2014 (1997).

[Gom06] L. Gomez, R. Bachelot, A. Bouhelier, G. P. Wiederrecht, S. Chang, S. K. Gray, F. Hua, S. Jeon, J. A. Rogers, M. E. Castro et al. *Apertureless scanning near-field optical microscopy: a comparison between homodyne and heterodyne approaches.* Journal of the Optical Society of America B **23**, 823 (2006).

[Har92] P. Hariharan. *Basics of Interferometry* (Academic Press, Inc., Boston, 1992).

[Har95] P. Harrison. *Quantum Wells, Wires and Dots* (John Wiley & Sons, Ltd., Chichester, 1995).

[Hec89] E. Hecht. *Optik* (Addison-Wesley Publishing Company, Bonn, 1989).

[Hec00] B. Hecht, B. Sick, U. P. Wild, V. Deckert, R. Zenobi, O. J. F. Martin, and D. W. Pohl. *Scanning near-field optical microscopy with aperture probes: Fundamentals and applications.* Journal of Chemical Physics **112**, 7761 (2000).

[Hes94] H. F. Hess, E. Betzig, T. D. Harris, L. N. Pfeiffer, and K. W. West. *Near-Field Spectroscopy of the Quantum Constituents of a Luminescent System.* Science **17**, 5166 (1994).

[Hil02] R. Hillenbrand and F. Keilmann. *Material-specific mapping of metal/semiconductor/dielectric nanosystems at 10 nm resolution by backscattering near-field optical microscopy.* Applied Physics Letters **80**, 25 (2002).

[Hol77] R. T. Holm, J. W. Gibson, and E. D. Palik. *Infrared reflectance studies of bulk and epitaxial-film n-type GaAs.* Journal of Applied Physics **48**, 212 (1977).

[Hop76] F. A. Hopf, P. Meystre, M. O. Scully, and W. H. Louisell. *Classical theory of a free-electron laser.* Physical Review Letters **37**, 1215 (1976).

[Hou07] J. Houel, S. Sauvage, P. Boucaud, A. Dazzi, R. Prazeres, F. Glotin, J. M. Ortéga, A. Miard, and A. Lemaître. *Ultraweak-absorption microscopy of a single semiconductor quantum dot in the midinfrared range.* Physical Review Letters **99**, 217404 (2007).

[Hou10] J. Houel, S. Sauvage, A. Lemaître, and P. Boucaud. *Interference effects on bound-to-continuum quantum dot absorption.* Journal of Applied Physics **107**, 083102 (2010).

[Hub07] A. J. Huber, D. Kazantsev, F. Keilmann, J. Wittborn, and R. Hillenbrand. *Simultaneous IR material recognition and conductivity mapping by nanoscale near-field microscopy.* Advanced Materials **19**, 2209 (2007).

[Hub10] A. J. Huber, J. Wittborn, and R. Hillenbrand. *Infrared spectroscopic near-field mapping of single nanotransistors.* Nanotechnology **21**, 235702 (2010).

[Hum88] J. Humlîček and K. Vojtěchovský. *Infrared optical constants of n-type silicon.* Czechoslovak Journal of Physics **38**, 1033 (1988).

[Ino94] Y. Inouye and S. Kawata. *Near-field scanning optical microscope with a metallic probe tip.* Optics Letters **19**, 159 (1994).

[Jac98] L. Jacak, P. Hawrylak, and A. Wójs. *Quantum Dots* (Springer Verlag, Berlin, 1998).

[Jac10] R. Jacob, S. Winnerl, H. Schneider, M. Helm, M. T. Wenzel, H.-G. von Ribbeck, L. M. Eng, and S. C. Kehr. *Quantitative determination of the charge carrier concentration of ion implanted silicon by IR-near-field spectroscopy.* Optics Express **18**, 26206 (2010).

[Joy00] P. B. Joyce, T. J. Krzyzewski, G. R. Bell, T. S. J. S. Malik, D. Childs, and R. Murray. *Effect of growth rate on the size, composition, and optical properties of InAs/GaAs quantum dots grown by molecular-beam epitaxy.* Physical Review B **62**, 10891 (2000).

[Joy01] P. B. Joyce, T. J. Krzyzewski, G. R. Bell, and T. S. Jones. *Surface morphology evolution during the overgrowth of large InAs-GaAs quantum dots.* Applied Physics Letters **79**, 3615 (2001).

[Keh08] S. C. Kehr, M. Cebula, O. Mieth, T. Härtling, J. Seidel, S. Grafström, L. M. Eng, S. Winnerl, D. Stehr, and M. Helm. *Anisotropy contrast in phonon-enhanced apertureless near-field microscopy using a free-electron laser.* Physical Review Letters **100**, 256403 (2008).

[Kei09] F. Keilmann, A. J. Huber, and R. Hillenbrand. *Nanoscale conductivity contrast by scattering-type near-field optical microscopy in the visible, infrared and THz domains.* Journal of Infrared, Millimeter, and Terahertz Waves **30**, 1255 (2009).

[Kel98] L. Kelvin. *Contact electricity of metals.* Philosophical Magazine **46**, 82 (1898).

[Kim98] J. Kim, L.-W. Wang, and A. Zunger. *Comparison of the electronic structure of InAs/GaAs pyramidal quantum dots with different facet orientations.* Physical Review B **57**, 9408 (1998).

[Kit06] C. Kittel. *Einführung in die Festkörperphysik* (Oldenbourg Wissenschaftsverlag GmbH, 2006).

[Kni76] D. J. E. Knight and P. T. Woods. *Application of nonlinear devices to optical frequency measurement.* Journal of Physics E **9**, 898 (1976).

[Kni96] G. Knippels. *The Short-Pulse Free-Electron Laser: Manipulation of the Gain Medium.* Ph.D. thesis, Vrije Universiteit Amsterdam (1996).

[Kno99] B. Knoll and F. Keilmann. *Near-field probing of vibrational absorption for chemical microscopy.* Nature **399**, 134 (1999).

[Kno00] B. Knoll and F. Keilmann. *Infrared conductivity mapping for nanoelectronics.* Applied Physics Letters **77**, 3980 (2000).

[Kog97] J. Koglin, U. Fischer, and H. Fuchs. *Material contrast in scanning near-field optical microscopy at 1-10 nm resolution.* Physical Review B **55**, 7977 (1997).

[Kop07] I. Kopf, J.-S. Samson, G. Wollny, C. Grunwald, E. Bründermann, and M. Havenith. *Chemical imaging of microstructured self-assembled monolayers with nanometer resolution.* Journal of Physical Chemistry C **111**, 8137 (2007).

[Lah96] A. Lahrech, R. Bachelot, P. Gleyzes, and A. C. Boccar. *Infrared reflection-mode near-field microscopy using an apertureless probe with a resolution of* $\lambda/600$. Optics Letters **21**, 1315 (1996).

[Lah97] A. Lahrech, R. Bachelot, P. Gleyzes, and A. C. Boccara. *Infrared near-field imaging of implanted semiconductors: Evidence of a pure dielectric contrast.* Applied Physics Letters **71**, 575 (1997).

[Lan88] E. Landi, A. Armigliato, S. Solmi, R. Kögler, and E. Wieser. *Electrical activation of boron-implanted silicon during rapid thermal annealing.* Applied Physics A **47**, 359 (1988).

[Lew84] A. Lewis, M. Isaacson, A. Harootunian, and A. Muray. *Development of a 500Å spatial resolution light microscope.* Ultramicroscopy **13**, 227 (1984).

[Lop04] C. Loppacher, U. Zerweck, and L. M. Eng. *KPFM of alkali chloride thin films on Au (111).* Nanotechnology **15**, S9 (2004).

[Lop05] C. Loppacher, U. Zerweck, S. Teich, E. Beyreuther, T. Otto, S. Grafstrom, and L. M. Eng. *FM demodulated Kelvin probe force microscopy for surface photovoltage tracking.* Nanotechnology **16**, 1 (2005).

[Lor65] O. G. Lorimor and W. G. Spitzer. *Infrared Refractive Index and Absorption of InAs and CdTe.* Journal of Applied Physics **36**, 1841 (1965).

[Mad71] J. M. J. Madey. *Stimulated emission of bremsstrahlung in a periodic magnetic field.* Journal of Applied Physics **42**, 1906 (1971).

[Mad79] J. M. J. Madey. *Relationship between mean radiated energy, mean squared radiated energy and spontaneous power spectrum in a power series expansion of the equations of motion in a free-electron laser.* Il Nuovo Cimento B **50**, 64 (1979).

[Mai60] T. H. Maiman. *Stimulated optical radiation in ruby.* Nature **187**, 493 (1960).

[Mar94] J. Y. Marzin, J. M. Gérard, A. Izraël, and D. Barrier. *Photoluminescence of single InAs quantum dots obtained by self-organized growth on GaAs.* Physical Review Letters **73**, 716 (1994).

[Mat00] K. Matsuda, T. Saiki, H. Saito, and K. Nishi. *Room-temperature photoluminescence spectroscopy of self-assembled $In_{0.5}Ga_{0.5}As$ single quantum dots by using highly sensitive near-field scanning optical microscope.* Applied Physics Letters **76**, 73 (2000).

[Mey92] E. Meyer. *Atomic force microscopy.* Progress in Surface Science **41**, 3 (1992).

[Mil88] P. W. Milonni and J. H. Eberly. *Lasers* (John Wiley & Sons, Inc., New York, 1988).

[Mot51] H. Motz. *Applications of the radiation from fast electron beams.* Journal of Applied Physics **22**, 527 (1951).

[Mot53] H. Motz, W. Thon, and R. N. Whitehurst. *Experiments on radiation by fast electron beams.* Journal of Applied Physics **24**, 826 (1953).

[Mur93] C. B. Murray, D. J. Norris, and M. G. Bawendi. *Synthesis and characterization of nearly monodisperse CdE (E = sulfur, selenium, tellurium) semiconductor nanocrystallites.* Journal of the American Chemical Society **115**, 8706 (1993).

[Mut99] H. Mutschke, A. Andersen, D. Clément, T. Henning, and G. Peiter. *Infrared properties of SiC particles.* Astronomy and Astrophysics **345**, 187 (1999).

[Non91] M. Nonnenmacher, M. P. O'Boyle, and H. K. Wickramasinghe. *Kelvin probe force microscopy.* Applied Physics Letters **58**, 2921 (1991).

[Nov97] L. Novotny, R. X. Bian, and X. S. Xie. *Theory of nanometric optical tweezers.* Physical Review Letters **79**, 645 (1997).

[Oce04] N. Ocelic and R. Hillenbrand. *Subwavelength-scale tailoring of surface phonon polaritons by focused ion-beam implantation.* Nature Materials **3**, 606 (2004).

[Oce06] N. Ocelic, A. J. Huber, and R. Hillenbrand. *Pseudoheterodyne detection for background-free near-field spectroscopy.* Applied Physics Letters **89**, 101124 (2006).

[Oga10] Y. Ogawa, F. Minami, Y. Abate, and S. R. Leone. *Nanometer-scale dielectric constant of Ge quantum dots using apertureless near-field scanning optical microscopy.* Applied Physics Letters **96**, 063107 (2010).

[O'S01] P. G. O'Shea and H. P. Freund. *Free-electron lasers: Status and applications.* Science **292**, 1853 (2001).

[Pae96] M. A. Paesler and P. J. Moyer. *Near-field optics: theory, instrumentation, and application* (John Wiley & Sons, Inc., New York, 1996).

[Pal98] E. D. Palik (Editor). *Handbook of Optical Constants of Solids*, vol. 3 (Academic Press, Limited, London, 1998).

[Pan98] D. Pan, Y. Zeng, M. Kong, J. Wu, Y. Zhu, C. Zhang, J. Li, and C. Wang. *Normal incident infrared absorption from InGaAs/GaAs quantum dot superlattice.* Electronics Letters **32**, 1726 (1998).

[Pap96] V. A. Papadichev. *Polarization in free electron lasers.* Nuclear Instruments and Methods in Physics Research Section A **375**, 483 (1996).

[Pas07] T. Passow, S. Li, P. Feinäugle, T. Vallaitis, J. Leuthold, D. Litvinov, D. Gerthsen, and M. Hetterich. *Systematic investigation into the influence of growth conditions on InAs/GaAs quantum dot properties.* Journal of Applied Physics **102**, 073511 (2007).

[Pet91] P. M. Petroff, Y. J. Li, Z. Xu, W. Beinstingl, S. Sasa, and K. Ensslin. *Nanostructures processing by focused ion beam implantation.* Journal of Vacuum Science & Technology B **9**, 3074 (1991).

[Phi60] R. M. Phillips. *The ubitron, a high-power traveling-wave tube based on a periodic beam interaction in unloaded waveguide.* IRE Transactions on Electron Devices **7**, 231 (1960).

[Phi88] R. M. Phillips. *History of the ubitron.* Nuclear Instruments and Methods in Physics Research A **272**, 1 (1988).

[Poh84] D. Pohl, W. Denk, and M. Lanz. *Optical stethoscopy: Image recording with resolution* $\lambda/20$. Applied Physics Letters **44**, 651 (1984).

[Pos94] M. Posselt. *Crystal-TRIM and its application to investigations on channeling effects in ion implantation.* Radiation Effects and Defects in Solids **130**, 87 (1994).

[Rai75] S. I. Raider, R. Flitsch, and M. J. Palmer. *Oxide-growth on etched silicon in air at room-temperature.* Journal of the Electrochemical Society **122**, 413 (1975).

[Ras03] M. B. Raschke and C. Lienau. *Apertureless near-field optical microscopy: Tip-sample coupling in elastic light scattering.* Applied Physics Letters **83**, 5089 (2003).

[Ray96] S. Raymond, S. Fafard, P. J. Poole, A. Wojs, P. Hawrylak, and S. Charbonneau. *State filling and time-resolved photoluminescence of excited states in* $In_xGa_{1-x}As/GaAs$ *self-assembled quantum dots.* Physical Review B **54**, 11548 (1996).

[Ree86] M. A. Reed, R. T. Bate, K. Bradshaw, W. M. Duncan, W. R. Frensley, J. W. Lee, and H. D. Shih. *Spatial quantization in GaAs-AlGaAs multiple quantum dots.* Journal of Vacuum Science & Technology B **4**, 358 (1986).

[Ree88] M. A. Reed, J. N. Randall, R. J. Aggarwal, R. J. Matyi, T. M. Moore, and A. E. Wetsel. *Observation of discrete electronic states in a zero-dimensional semiconductor nanostructure.* Physical Review Letters **60**, 535 (1988).

[Ren04] J. Renger, S. Grafström, L. M. Eng, and V. Deckert. *Evanescent wave scattering and local electric field enhancement at ellipsoidal silver particles in the vicinity of a glass surface.* Journal of the Optical Society of America A **21**, 1362 (2004).

[Ren05] J. Renger, S. Grafström, L. Eng, and R. Hillenbrand. *Resonant light scattering by near-field-induced phonon polaritons.* Physical Review B **71**, (2005).

[Rit65] J. C. Ritter, M. N. Robinson, B. J. Faraday, and J. I. Hoover. *Room temperature oxidation of silicon during and after etching.* Journal of Physics and Chemistry of Solids **26**, 721 (1965).

[Roy05] D. Roy, S. H. Leong, and M. E. Welland. *Dielectric contrast imaging using apertureless scanning near-field optical microscopy in the reflection mode.* Journal of the Korean Physical Society **47**, 140 (2005).

[Rys80] H. Ryssel, K. Müller, K. Haberger, R. Henkelmann, and F. Jahnel. *High concentration effects of ion implanted boron in silicon.* Applied Physics A **22**, 35 (1980).

[Sai99] H. Saito, K. Nishi, and S. Sugou. *Shape transition of InAs quantum dots by growth at high temperature.* Applied Physics Letters **74**, 1224 (1999).

[Sam06] J.-S. Samson, G. Wollny, E. Bründermann, A. Bergner, A. Hecker, G. Schwaab, A. Dirk Wieck, and M. Havenith. *Setup of a scanning near field infrared microscope (SNIM): Imaging of sub-surface nano-structures in gallium-doped silicon.* Physical Chemistry Chemical Physics **8**, 753 (2006).

[Sam08] J.-S. Samson. *Near-field microscopy.* Ph.D. thesis, Ruhr Universität Bochum (2008).

[Sau01] S. Sauvage, P. Boucaud, T. Brunhes, A. Lemaître, and J.-M. Gérard. *Intersublevel emission in InAs/GaAs quantum dots.* physica status solidi (b) **224**, 579 (2001).

[Sau11] S. Sauvage, A. Driss, F. Réveret, P. Boucaud, A. Dazzi, R. Prazeres, F. Glotin, J.-M. Ortéga, A. Miard, Y. Halioua, F. Raineri, I. Sagnes, and A. Lemaître. *Homogeneous broadening of the S to P transition in InGaAs/GaAs quantum dots measured by infrared absorption imaging with nanoscale resolution.* Physical Review B **83**, 035302 (2011).

[Sch06] D. K. Schroder. *Semiconductor Material and Device Characterization* (John Wiley & Sons, Inc., Hoboken, 2006).

[Sch07a] S. Schneider, J. Seidel, S. Grafström, L. M. Eng, S. Winnerl, D. Stehr, and M. Helm. *Impact of optical in-plane anisotropy on near-field phonon polariton spectroscopy.* Applied Physics Letters **90**, 143101 (2007).

[Sch07b] S. C. Schneider. *Scattering Scanning Near-Field Optical Microscopy on Anisotropic Dielectrics.* Ph.D. thesis, Technische Universität Dresden (2007).

[Sha01] I. I. Shaganov, T. S. Perova, R. A. Moore, and K. Berwick. *Spectroscopic characteristics of SiO and SiO_2 solid films: Assignment and local field effect influence.* Materials in Electronics **12**, 351 (2001).

[Sol91] S. Solmi, F. Baruffaldi, and R. Canteri. *Diffusion of boron in silicon during post implantation annealing.* Journal of Applied Physics **69**, 2135 (1991).

[Son03] R. Songmuang, S. Kiravittaya, and O. Schmidt. *Shape evolution of InAs quantum dots during overgrowth.* Journal of Crystal Growth **249**, 416 (2003).

[Spe92] M. Specht, J. D. Pedarnig, W. M. Heckl, and T. W. Hänsch. *Scanning plasmon near-field microscope.* Physical Review Letters **68**, 476 (1992).

[Spi57] W. G. Spitzer and H. Y. Fan. *Determination of optical constants and carrier effective mass of semiconductors.* Physical Review **106**, 882 (1957).

[Ste01] R. Stevenson, R. Riehn, R. G. Milner, D. Richards, E. Moons, D.-J. Kang, M. Blamire, J. Morgado, , and F. Cacialli. *Ultraviolet-visible near-field microscopy of phase-separated blends of polyfluorene-based conjugated semiconductors.* Applied Physics Letters **79**, 833 (2001).

[Ste03] L. Stebounova, B. B. Akhremitchev, and G. C. Walker. *Enhancement of the weak scattered signal in apertureless near-field scanning infrared microscopy.* Review of Scientific Instruments **74**, 3670 (2003).

[Ste06] D. Stehr. *Infrared studies of impurity states and ultrafast carrier dynamics in semiconductor quantum structures.* Ph.D. thesis, Technische Universität Dresden (2006).

[Sti10] J. M. Stiegler, A. J. Huber, S. L. Diedenhofen, J. Gomez Rivas, R. E. Algra, E. Bakkers, and R. Hillenbrand. *Nanoscale free-carrier profiling of individual semiconductor nanowires by infrared near-field nanoscopy.* Nano Letters **10**, 1387 (2010).

[Str39] I. N. Stranski and L. V. Krastanov. Abhandlungen der Mathematisch-Naturwissenschaftlichen Klasse. Akademie der Wissenschaften und der Literatur in Mainz **146**, 797 (1939).

[Syn28] E. H. Synge. *XXXVIII. A suggested method for extending microscopic resolution into the ultra-microscopic region.* Philosophical Magazine **6**, 356 (1928).

[Tak91] Y. Takeuchi and M. Inaba. *Measurement of silicon native oxide thickness by XPS.* Analytical Sciences **7 supplement**, 333 (1991).

[Tau04] T. Taubner, F. Keilmann, and R. Hillenbrand. *Nanomechanical resonance tuning and phase effects in optical near-field interaction.* Nano Letters **4**, 1669 (2004).

[Tes05] E. Tesch (1905).
URL `http://upload.wikimedia.org/wikipedia/commons/b/b7/Ernst_Abbe.jpg`

[vdH81] H. C. van de Hulst. *Light scattering by small particles* (Dover Publications, Inc., New York, 1981).

[Voh04] B. Vohnsen. *A short history of optics.* Physica Scripta **109**, 75 (2004).

[vR08] H. G. von Ribbeck, M. Brehm, D. W. Van der Weide, S. Winnerl, O. Drachenko, M. Helm, and F. Keilmann. *Spectroscopic THz near-field microscope.* Optics Express **16**, 3430 (2008).

[Vuk06] N. Vukmirović, Ž. Gačević, Z. Ikonić, D. Indjin, P. Harrison, and V. Milanović. *Intraband absorption in InAs/GaAs quantum dot infrared photodetectors - effective mass versus $k \cdot p$ modelling.* Semiconductor Science and Technology **21**, 1098 (2006).

[Web34] E. H. Weber. *Annotationes Anatomicae Et Physiologicae* (Koehler, 1834), chap. De Pulsu, Resorptione, Auditu Et Tactu.

[Wes85] J. Wessel. *Surface-enhanced optical microscopy.* Journal of the Optical Society of America B **2**, 1538 (1985).

[Wie84] E. Wieser and D. Panknin. *Electrical activation and damage annealing of boron-implanted silicon by flash-lamp irradiation.* physica status solidi (a) **82**, 171 (1984).

[Wil00] A. J. Williamson, L. W. Wang, and A. Zunger. *Theoretical interpretation of the experimental electronic structure of lens-shaped self-assembled InAs/GaAs quantum dots.* Physical Review B **62**, 12963 (2000).

[Woj97] A. Wojs and P. Hawrylak. *Theory of photoluminescence from modulation-doped self-assembled quantum dots in a magnetic field.* Physical Review B **55**, 13066 (1997).

[Wol83] A. Wolkenberg. *A mechanism for the effect of doping on the silicon native oxide thickness.* physica status solidi (a) **79**, 313 (1983).

[Wu04] C. Wu, M. Ye, and H. Ye. *Model for scanning near-field optical microscopy.* Journal of Optics A **6**, 1082 (2004).

[Zen94] F. Zenhausern, M. P. O'Boyle, and H. K. Wickramasinghe. *Apertureless near-field optical microscope.* Applied Physics Letters **65**, 1623 (1994).

[Zha04] J.-Z. Zhang and I. Galbraith. *Intraband absorption for InAs/GaAs quantum dot infrared photodetectors.* Applied Physics Letters **84**, 1934 (2004).

[ZT07] U. Zerweck-Trogisch. *Auflösungsvermögen und Genauigkeit der Kelvinsonden-Rasterkraftmikroskopie und deren Anwendung an molekularen Systemen.* Ph.D. thesis, Technische Universität Dresden (2007).

Publications

- R. Jacob, S. Winnerl, H. Schneider, M. Helm, M. T. Wenzel, H.-G. von Ribbeck, L.M. Eng, and S. C. Kehr. *Quantitative determination of the charge carrier concentration of ion implanted silicon by IR-near-field spectroscopy.* Optics Express **18**, 26206 (2010).
- R. Jacob, S. Winnerl, M. Helm, M. T. Wenzel, H.-G. von Ribbeck, M. Cebula, L.M. Eng, and S. C. Kehr. *Phase controlled homodyne interferometry for scattering near-field optical microscopy.* In preparation, (2011).
- R. Jacob, S. Winnerl, H. Schneider, M. Helm, M. T. Wenzel, H.-G. von Ribbeck, and L.M. Eng. *Intersublevel spectroscopy of single InAs-quantum dots by IR-near-field microscopy.* In preparation, (2011).

Acknowledgments

A PhD is never an easy task and I would have failed without the constant support of many people. A few of them were of such importance, that I want to thank them also in this written form:

As I am part of two groups, my first gratitudes go to my supervisors Prof. Manfred Helm and Prof. Lukas Eng. They welcomed me in their groups and offered constant help in all scientific and administrative issues. At the same time, they were patient for almost two years until I came up with my first results.

Many thanks also to Dr. Harald Schneider and Dr. Stephan Winnerl. Whenever I had problems or questions concerning semiconductors or FELs, they offered help even if they had some urgent things to do. Without their input, I would still fight the U27. Moreover, their interest in near-field microscopy did a great deal in helping me to understand the physics behind.

A great thank you to the SNOMiker at the TU Dresden: Susanne Kehr, Marc Tobias Wenzel, Hans-Georg von Ribbeck and Anja Krysztofinski. They kept me awake during endless night shifts, spent weekends with me in the lab and made boring shifts eventful. Their SNOM background was also a basis for genius ideas and fruitful discussions.

I also want to thank my other group members in Rossendorf for the fantastic working atmosphere: Martin Wagner, who did a great job in driving me nuts, Jayeeta Bhattacharyya, Sabine Zybell, Martin Mittendorff, Dominik Stehr, Matthias Baudisch, Carsten Franke and Johannes Krause. The made my time in Rossendorf enjoyable and entertaining. A special thanks also to Uta Lucchesi and Joachim Wagner who solved almost every technical problem. It was a great pleasure to work with them.

Another gratitude goes to the FELBE team, especially Wolfgang Seidel and the "super-operator" Rico Schurig. Their efforts to provide a running FEL regardless of my crazy machine parameters were another pillar to the success of the overall project. Furthermore, I want to thank the group of Dr. Bernd Schmidt in Rossendorf and Paola Atkinson for the superb samples, which they prepared for me.

Finally, there are my parents and my brothers. Without them I would not have come that far. Thanks for believing in me!

Erklärung

Diese Arbeit entstand am Helmholtz-Zentrum Dresden-Rossendorf unter wissenschaftlicher Betreuung durch Prof. Dr. Manfred Helm, Professor am Institut für Angewandte Physik der Fakultät Mathematik und Naturwissenschaften der Technischen Universität Dresden.

Ich versichere, dass ich die vorliegende Arbeit ohne unzulässige Hilfe Dritter und ohne Benutzung anderer als der angegebenen Hilfsmittel angefertigt habe. Die aus fremden Quellen direkt oder indirekt übernommenen Gedanken sind als solche kenntlich gemacht.

Die Arbeit wurde bisher weder im Inland noch im Ausland in gleicher oder ähnlicher Form einer anderen Prüfungsbehörde vorgelegt. Ich erkenne die Promotionsordnung der Fakultät Mathematik und Naturwissenschaften der Technischen Universität Dresden in der Fassung vom 19. August 2008 an.

Radebeul, den 24.01.2011 Rainer Jacob